# Probing Supersymmetry with Cosmogenic Neutrinos

by

Jessica Uscinski

---

A Dissertation Submitted to the Faculty of the

Department of Physics

In Partial Fulfillment of the Requirements
For the Degree of

Doctor of Philosophy

In the Graduate College

The University of Arizona

2 0 0 8

THE UNIVERSITY OF ARIZONA
GRADUATE COLLEGE

As members of the Dissertation Committee, we certify that we have read the dissertation prepared by Jessica Uscinski entitled "Probing Supersymmetry with Cosmogenic Neutrinos" and recommend that it be accepted as fulfilling the dissertation requirement for the Degree of Doctor of Philosophy.

_____ Date: 05/12/08
Ina Sarcevic

_____ Date: 05/12/08
Li-Zhi Fang

_____ Date: 05/12/08
Ken Johns

_____ Date: 05/12/08
Srinivas Manne

_____ Date: 05/12/08
Dimitrios Psaltis

Final approval and acceptance of this dissertation is contingent upon the candidate's submission of the final copies of the dissertation to the Graduate College.

I hereby certify that I have read this dissertation prepared under my direction and recommend that it be accepted as fulfilling the dissertation requirement.

_____ Date: 05/12/08
Dissertation Director: Ina Sarcevic

## Statement by Author

This dissertation has been submitted in partial fulfillment of requirements for an advanced degree at The University of Arizona and is deposited in the University Library to be made available to borrowers under rules of the Library.

Brief quotations from this dissertation are allowable without special permission, provided that accurate acknowledgment of source is made. Requests for permission for extended quotation from or reproduction of this manuscript in whole or in part may be granted by the head of the major department or the Dean of the Graduate College when in his or her judgment the proposed use of the material is in the interests of scholarship. In all other instances, however, permission must be obtained from the author.

Signed: Jessica Uscinski

# Table of Contents

Table of Contents—*Continued*

# List of Figures

LIST OF FIGURES—*Continued*

List of Figures—*Continued*

List of Figures—*Continued*

# List of Tables

# ABSTRACT

Neutrino telescopes have the potential to detect quasi-stable supersymmetric staus predicted by some supersymmetric models. A study of the signal for the detection of staus produced in interactions of cosmogenic neutrinos is presented. The detection depends on the stau electromagnetic energy loss and weak interactions. The results for the weak interaction contribution to the energy loss of high energy staus as they pass through rock is presented. The neutral current weak interaction contribution is much smaller than photonuclear energy loss, however, the charged current contribution may become the dominant process for energies above $\sim 10^9$ GeV. As a consequence, the stau range may be reduced above $\sim 10^9$ GeV as compared to the range neglecting weak interactions.

A detailed analysis of the incoming cosmogenic neutrino flux, neutrino attenuation, stau production, and stau energy loss shows that there is an optimal nadir angle for which the stau signal is a factor of several hundred larger than the muon signal. A discussion is presented of how one could potentially eliminate the muon background by considering the energy loss of muons in the detector. The results for the showers produced by weak interactions of staus that reach the detector is presented and compared to the showers produced by neutrinos.

# Chapter 1
# Introduction

The Standard Model (SM) of particle physics currently is the best description of experimental data on elementary particle interactions. The SM describes the three fundamental electromagnetic, weak, and strong interactions and excludes gravity. One of the most fundamental questions that exists in particle physics today is that of the hierarchy between the fundamental forces, specifically why the weak energy scale ($\sim$ 100 GeV) and the Planck energy scale ($\sim 10^{19}$ GeV) are so vastly different. This is known as the "hierarchy problem" and is one of the major impetuses for studies of physics "Beyond the Standard Model" where it is expected that new physics will emerge at $\sim$ TeV. Interactions of ultrahigh energy ($E_\nu > 10^{17}$ eV, UHE) neutrinos with nucleons as they traverse the Earth have the potential to probe very large center of mass energies ($> 14$ TeV) and may therefore delve into this region of physics beyond the Standard Model between the weak energy scale and the Planck energy scale. UHE neutrinos originate from interactions of cosmic ray protons from astrophysical sources, such as Active Galactic Nuclei or Gamma Ray Bursts, with cosmic microwave background photons or from the sources themselves. They travel to the Earth unaffected by magnetic fields and only interacting weakly, meaning they contain information from their creation point.

One of the most studied extensions to the standard model that provides a solution to the "hierarchy problem" is known as supersymmetry (SUSY). SUSY models contain a natural extension of space-time symmetries and introduce heavy fermion and boson superpartners to SM particles. In some supersymmetric models, UHE neutrinos interact with nucleons in the Earth to produce heavy supersymmetric particles that decay into quasi-stable sleptons. In weak scale SUSY models where the SUSY

breaking scale is $\sim 10^7$ GeV, these sleptons are the superpartners of taus (staus) that have a very long lifetime. Due to very long lifetimes, staus may travel thousands of kilometers through the Earth without decaying. It has been proposed that a direct way of probing the SUSY breaking scale in weak scale supersymmetry models would be to detect pairs of charged tracks in neutrino detectors, such as IceCube, from staus resulting from neutrino-nucleon interactions producing heavier supersymmetric particles [9]. This scenario has been further studied in Refs [3–5, 10–18].

Because of the small cross section, the production of staus from downward neutrinos is negligible in comparison with the background from the standard model processes. However, heavy staus produced from upward neutrinos could potentially be detectable because the effective detector volume is enlarged by the staus' long range. The detection of staus in neutrino telescopes depends very strongly on the lifetime and range. It is therefore important to study the stau energy loss as it traverses the Earth to determine the expected signal.

The second chapter of this work describes background information on neutrino physics including neutrino oscillations in vacuum. The next section describes evidence for neutrino oscillations including observations of solar neutrinos and atmospheric neutrinos. Current limits on neutrino mixing parameters are presented.

The third chapter describes the field of neutrino astronomy and begins with a discussion on neutrinos detected from Supernova 1987a. The next section provides a discussion of two astrophysical sources for cosmic ray protons and possibly UHE neutrinos, Active Galactic Nuclei and Gamma Ray Bursts. The neutrino flux models of Waxman and Bahcall [19] and of Engel, Seckel, and Stanev [20] are presented. Neutrino- nucleon interactions in the earth are described and the neutrino interaction length and density profile of the earth are presented. Finally, some UHE neutrino experiments that have a bearing on the present work are discussed.

The fourth chapter describes using neutrinos to probe physics beyond the SM. The next section describes the "Hierarchy Problem" in the SM and SUSY is presented as

a solution. A description of low-scale SUSY models and the stau production process is presented and compared to neutrino SM processes.

The fifth chapter discusses the methods used to determine the energy loss and range of leptons and sleptons. The different contributions to the stau energy loss as it traverses the earth are presented, including a region of parameter space where the possibility of weak interactions is included. The results from the inclusion of maximal weak interactions in the determination of the energy loss and range for staus and taus are given, where staus show a large suppression in the range and taus are unaffected.

The sixth chapter shows the results for the lepton and slepton fluxes in a neutrino detector such as ANITA using an incident cosmogenic neutrino flux and including maximal weak interactions. The muon and stau fluxes and ratios are presented both for different nadir angles and for different energies at specific nadir angles. The ratio is shown to be large for specific angles and energies, meaning that the staus may have the potential to be detected over the muon background. Staus are shown to have "muon-like" signals and the stau flux for a rescaled stau energy is presented, significantly decreasing the stau/muon ratio. A possible method of extracting the stau signal is presented. Finally stau charged tracks and stau showers in the ice are presented and compared to the signal produced by neutrinos. A discussion of the comparison of these results with the results obtained by using an incident Waxman-Bahcall neutrino flux is also given.

# Chapter 2
# Neutrino Physics

The neutrino was first proposed to exist by Wolfgang Pauli in 1930 to explain the continuous spectrum observed in beta decay [21]. It was proposed to be a very light particle with a small cross section for interaction. Neutrinos were not observed experimentally however, until 1956 when Cowan and Reines [22] observed antineutrinos created in a nuclear reactor in the reaction

$$\bar{\nu} + p \rightarrow n + e^{+}.$$

Beginning with the discovery in 1962 by Lederman and Schwartz of muon neutrino interactions, it was shown that different types of "flavors" of neutrinos exist [23]. The discovery of the tau lepton in 1975 at the Stanford Linear Accelerator [24] led to the postulation of a third type of neutrino associated with the tau. Tau neutrino interactions were detected in 2000 by the DONUT collaboration at Fermilab [25].

Neutrinos are assumed to be purely left-handed massless particles in the Standard Model (SM) of particle physics. Neutrinos and their corresponding leptons form a left-handed "weak-isospin" doublet designated by

$$L \equiv \begin{pmatrix} \nu \\ e \end{pmatrix}_L \tag{2.1}$$

where the left-handed neutrino state is

$$\nu_L = \frac{1}{2}(1 - \gamma_5)\nu \tag{2.2}$$

and the right-handed state

$$\nu_R = \frac{1}{2}(1 + \gamma_5)\nu = 0, \tag{2.3}$$

as a consequence of neutrinos being massless. They are electrically neutral leptons meaning that they interact only through the weak force and not the strong or electromagnetic forces. Weak interactions are described by the exchange of the weak $W$ and $Z$ gauge bosons. The interaction Lagrangian corresponding to the charged gauge bosons $W^{\pm}$ is given by [26],

$$\mathcal{L}_{W-\ell} = -\Big(\frac{G_F M_W^2}{\sqrt{2}}\Big)^{1/2}\Big[\bar{\nu}\gamma^{\mu}(1-\gamma_5)eW_{\mu}^{+} + \bar{e}\gamma^{\mu}(1-\gamma_5)\nu W_{\mu}^{-}\Big] \tag{2.4}$$

while the corresponding piece for the neutral gauge boson $Z^0$ is given by

$$\mathcal{L}_{0-\ell} = \frac{-1}{\sqrt{2}}\Big(\frac{G_F M_Z^2}{\sqrt{2}}\Big)^{1/2}\bar{\nu}\gamma^{\mu}(1-\gamma_5)\nu Z_{\mu}. \tag{2.5}$$

The term $G_F$ represents the strength of the Fermi interaction. The masses of the weak bosons are related through the weak mixing angle $\theta_W$ by

$$M_Z^2 = M_W^2/\cos^2\theta_W. \tag{2.6}$$

The SM itself is comprised of many arbitrary parameters and it is believed by many to be a low energy limit of a more complete theory. In such theories the neutrino is generally a massive particle and as such, there exists a leptonic mixing matrix corresponding to the Cabibbo-Kobayashi-Maskawa (CKM) matrix, completing the lepton-quark analogy.

Interactions of the three neutrino flavors have been observed experimentally, however no direct measurements of the neutrino mass have been made. The observation of neutrino oscillations, however, provides convincing evidence for a nonzero neutrino mass [27]. In this chapter, the framework describing neutrino oscillations is presented as well as experimental evidence supporting oscillations as seen in solar and atmospheric neutrinos.

## 2.1 Neutrino Oscillations

In 1957 Bruno Pontecorvo [28] proposed that the differing neutrino flavors could inter convert in a process known as oscillations. Oscillations occur due to the differing

neutrino flavor and mass eigenstates. The matter waves associated with the neutrino mass eigenstates interfere with each other. The flavor eigenstates exist as mixtures of the mass eigenstates, indicating that if a specific flavored neutrino is produced, it is plausible that a different flavor will be detected at a given distance for a fixed value of neutrino energy. This probability is a function of the distance between the source and the detector.

We can write the weak (flavor) eigenstate as a superposition of the mass eigenstates for a neutrino the following way

$$|\nu_\ell(t=0)>=\sum_i U_{\ell j}|\nu_j> \tag{2.7}$$

where $\ell$ represents the charged lepton that produced the neutrino and can be either $e$, $\mu$, or $\tau$ and $|\nu_j>$ represents the mass eigenstate with eigenvalue $m_j$, with energy $E_j$ and momentum $p$. The matrix $U_{\ell j}$ is the lepton mixing matrix from the electroweak SM. The evolution of the neutrino state over time can be found by evaluating the effect of the time evolution operator $U = e^{-\imath(E_j t)}$ on the initial state to obtain

$$|\nu_\ell(t)>=\sum_j U_{\ell j} e^{-\imath E_j t}|\nu_j> \tag{2.8}$$

We can observe the effect of two-flavor mixing ($\nu_e$ and $\nu_\mu$) on the evolution of the flavor state where the mixing matrix U has the form

$$\begin{pmatrix} \cos\theta & \sin\theta \\ -\sin\theta & \cos\theta \end{pmatrix} \tag{2.9}$$

The angle $\theta$ represents the weak mixing angle that is the analog to the Cabibbo mixing angle for quarks. The evolution over time for two-flavor oscillations can then be written as

$$\begin{pmatrix} \nu_e(t) \\ \nu_\mu(t) \end{pmatrix} = \begin{pmatrix} \cos\theta\, e^{-\imath E_1 t} & \sin\theta\, e^{-\imath E_2 t} \\ -\sin\theta\, e^{-\imath E_1 t} & \cos\theta\, e^{-\imath E_2 t} \end{pmatrix} \begin{pmatrix} \nu_1 \\ \nu_2 \end{pmatrix} \tag{2.10}$$

The neutrinos are nearly massless and relativistic ($E_\nu >> m_\nu$), allowing the neutrino energy to be written as

$$E_{1,2} = (p^2 + m_{1,2}^2)^{1/2} \cong p + \frac{m_{1,2}^2}{2p} \tag{2.11}$$

Making these substitutions, the probability of finding a neutrino with flavor $\ell'$ ($\ell' \neq \ell$) at a location L ($L = vt$) and time t can be calculated from the square amplitude of the projection of the state $|\nu_{\ell'}(t) >$ onto $|\nu_\ell(0) >$,

$$P(\ell \to \ell') = | < \nu_{\ell'}(t)|\nu_\ell(0) > |^2 = \sin^2 2\theta \sin^2(\frac{\Delta\phi}{2}) \tag{2.12}$$

The quantity $\Delta\phi$ represents the relative phase between the two flavor eigenstates and is determined to be $\Delta\phi = \frac{2\pi L}{\lambda_{osc}}$. The quantity $\lambda_{osc}$ is the oscillation length for the probability, or the distance between the maxima or minima and is given by $\lambda_{osc} = \frac{\pi E_{1,2}}{1.27\Delta m^2}$. This analysis shows that the probability depends on the mass squared difference of the neutrinos $\Delta m^2$, the neutrino energy $E_{1,2}$, the distance between source and detector L, and the weak mixing angle $\theta$.

The two-flavor oscillation model is frequently used in neutrino oscillation experiments. For N number of neutrino flavors, the mixing matrix becomes $N \times N$. For three-flavor oscillations with a $3 \times 3$ matrix, there are 3 mass squared differences to consider: $\Delta m^2_{12}$, $\Delta m^2_{13}$, and $\Delta m^2_{23}$. The mixing matrix for this scenario is given by the Maki-Nakagawa Sakata (MNS) matrix [29],

$$\begin{aligned} U &= \begin{pmatrix} c_{12}c_{13} & s_{12}s_{13} & s_{13}e^{-\imath\delta} \\ -s_{12}c_{23} - c_{12}s_{23}s_{13}e^{\imath\delta} & c_{12}c_{23} - s_{12}s_{23}s_{13}e^{\imath\delta} & s_{23}c_{13} \\ s_{12}s_{23} - c_{12}c_{23}s_{13}e^{\imath\delta} & -c_{12}s_{23} - s_{12}c_{23}s_{13}e^{\imath\delta} & c_{23}c_{13} \end{pmatrix} \\ &\times \begin{pmatrix} e^{\imath\alpha_1/2} & 0 & 0 \\ 0 & e^{\imath\alpha_2/2} & 0 \\ 0 & 0 & 1 \end{pmatrix} \end{aligned} \tag{2.13}$$

where $c_{ij} = \cos\theta_{ij}$ and $s_{ij} = \sin\theta_{ij}$. The terms $\alpha_1$, $\alpha_2$, and $\delta$ represent CP violating phases. In this scenario, the probability that a neutrino with flavor $\alpha$ will oscillate to a neutrino with flavor $\beta$ is given by

$$\begin{aligned} P(\nu_\alpha \to \nu\beta) = \delta_{\alpha,\beta} &- 4\sum_{i>j} Re(U^*_{\alpha i}U_{\beta i}U_{\alpha j}U^*_{\beta j}) \sin^2(\frac{\pi L}{\lambda_{ij}}) \\ &+ 2\sum_{i>j} Im(U^*_{\alpha i}U_{\beta i}U_{\alpha j}U^*_{\beta j}) \sin^2(\frac{2\pi L}{\lambda_{ij}}) \end{aligned} \tag{2.14}$$

where again L represents the distance from source to detector and the oscillation length in this case is $\lambda_{ij} = \frac{\pi E_\nu}{1.27\Delta m^2_{ij}}$.

## 2.2 Evidence for Oscillations

To date, the sun and Supernovae SN1987A are the only confirmed sources of extra-terrestrial neutrinos. Neutrinos are also produced in air showers from cosmic rays interacting in Earth's atmosphere. Experiments that have been successful in detecting neutrinos with different origins and different energies have given information about neutrino oscillation mechanisms and also bounds on the values of the mass splittings and mixing angles between the neutrino states. Evidence for neutrino oscillations and therefore for the neutrino mass can be seen from both solar and atmospheric neutrino studies. The different energy regimes that these neutrino sources represent can be seen in Fig. 2.1, along with the supernovae relic neutrino (SRN) spectrum and electron antineutrinos from reactors. The results for the mass splittings and mixing angle measurements that are discussed in this section are summarized in Table 2.1.

| Mixing parameter | Value |
|---|---|
| $\theta_{12}$ | $33.9^{\circ}{}^{+2.4^{\circ}}_{-2.2^{\circ}}$ |
| $\Delta m^2_{12}$ | $8.0^{+0.6}_{-0.4} \times 10^{-5}$ eV$^2$ |
| $\theta_{23}$ | $45 \pm 7^{\circ}$ |
| $\Delta m^2_{23}$ | $2.4^{+0.6}_{-0.5} \times 10^{-3}$ eV$^2$ |
| $\theta_{13}$ | $< 13^{\circ}$ |
| $\Delta m^2_{13}$ | $\approx \Delta m^2_{23}$ |

TABLE 2.1. Solar neutrino experiments along with the reactor experiment KamLAND have placed constraints on the smaller mass splitting from the MNS matrix $\Delta m^2_{12} = 8.0^{+0.6}_{-0.4} \times 10^{-5}$ eV$^2$ as well as the mixing angle $\sin^2\theta_{12}$, where $\theta_{12} = 33.9^{\circ}{}^{+2.4^{\circ}}_{-2.2^{\circ}}$ [6]. The atmospheric mixing parameters are found from experiments such as SuperK and are determined to be $\Delta m^2_{23} = 2.4^{+0.6}_{-0.5} \times 10^{-3}$ eV$^2$ and $\theta_{23} = 45 \pm 7^{\circ}$ [7]. The third mixing parameter $\theta_{13}$ has been determined to be $< 13^{\circ}$ from the Chooz collaboration [8] Atmospheric and solar neutrino experiments have shown that the MNS matrix consists of two large mixing angles and one small.

### 2.2.1 Solar Neutrinos

The Standard Solar Model (SSM) describes the mechanisms for producing neutrinos in the sun [30]. The main nuclear reactions directly responsible for creating neutrinos are the *pp* chain and to a lesser extent the CNO cycle, and the corresponding energies range up to $\sim$ 18 MeV. The majority of solar neutrinos arise from the first step in the *pp* reaction with a corresponding energy $<$ 0.425 MeV. The Boron-8 side reaction of the *pp* chain produces the neutrinos that are most readily detected. Their flux is smaller, but they may have energies $\sim$ 15 MeV. The largest neutrino energy corresponds to the more rare *hep* reaction which has a significantly smaller flux and energies $\sim$ 18 MeV. The theoretical prediction of the electron neutrino flux at the Earth's surface within the context of the SSM yields $\sim 6.57 \times 10^{10}/$ cm$^2/$ s [31]. Solar neutrino experiments such as Homestake [32] have consistently detected fluxes significantly lower than the theoretical prediction, leading to the what is known as the "Solar neutrino problem."

The resolution of the "Solar neutrino problem" involves including neutrino oscillations. The predicted solar neutrino flux involves electron neutrinos created during the nuclear reactions powering the Sun. The inclusion of electron neutrino oscillations to other neutrino flavors can account for the observed discrepancy. The Sudbury Neutrino Observatory (SNO) [33] collaboration was the first reported evidence of solar neutrino oscillations. The SNO detector consists of heavy water ($D_2O$) that is sensitive to inverse beta decay processes ($\nu_e d \rightarrow e^- pp$), neutral current processes ($\nu_x d \rightarrow \nu_x pn$), and neutrino electron scattering events, thus allowing for the detection of all three neutrino flavors. In 2001, the SNO collaboration reported their findings of the total flux of all three neutrino flavors being consistent with the predictions of the SSM [34]. It was shown that previous experiments such as Homestake were only sensitive to electron neutrinos. Of the solar neutrinos detected, the results from SNO showed that about 35% were of the electron type, consistent with the observations

seen at Homestake. Results from the reactor experiment Kamioka Liquid Scintillator Antineutrino Detector (KamLAND) are consistent with the oscillation parameters determined from the solar signal [6].

### 2.2.2 Atmospheric Neutrinos

Atmospheric neutrinos are created when high energy cosmic rays create muons and pions in the Earth's atmosphere. Muon and pion decays lead to the production of muon and electron neutrinos. The ratio of muon to electron neutrinos due to the muon and pion decays is roughly predicted to be about 2 : 1 from examining the reactions:

$$p + A \rightarrow \pi^{\pm} + X \tag{2.15}$$

$$\begin{array}{ll} \pi^+ \rightarrow \mu^+ + \nu_\mu & \pi^- \rightarrow \mu^- + \bar{\nu}_\mu \\ \quad \downarrow & \quad \downarrow \\ \quad e^+ + \nu_e + \bar{\nu}_\mu & \quad e^- + \nu_\mu + \bar{\nu}_e \end{array}$$

Including neutrino oscillations over the distances traveled to detectors will change this ratio.

While atmospheric neutrinos are less abundant than solar neutrinos, they have higher energies and can therefore be detected more easily due to the neutrino SM cross section's rise with incident neutrino energy (discussed in Section 3.4, see Fig. 3.5). Atmospheric neutrinos can have energies in the range of a few MeV to the energy of an incoming cosmic ray. The wide range of possible energies implies that atmospheric neutrinos consist of a very large background against which neutrinos with astrophysical origins must be identified. Atmospheric neutrinos have yielded significant measurements of muon and tau neutrino oscillations. The large neutrino detector experiments Irvine-Michigan-Brookhaven (IMB) [35], Kamokande II [36], and

Soudan [37] all observed deficits in the ratio of fluxes of $\nu_\mu/\nu_e$ atmospheric neutrinos. Results from the Super Kamiokande experiment provided the first evidence of neutrino mass with the observation of oscillations of muon and tau neutrinos [27,38]. The accelerator experiments K2K [39] and the Main Injector Neutrino Oscillation Search (MINOS) [40] later observed neutrino oscillations consistent with the atmospheric signal and found parameters consistent with the results from Super Kamiokande. All of these results place constraints on the atmospheric mixing parameters as given in Table 2.1.

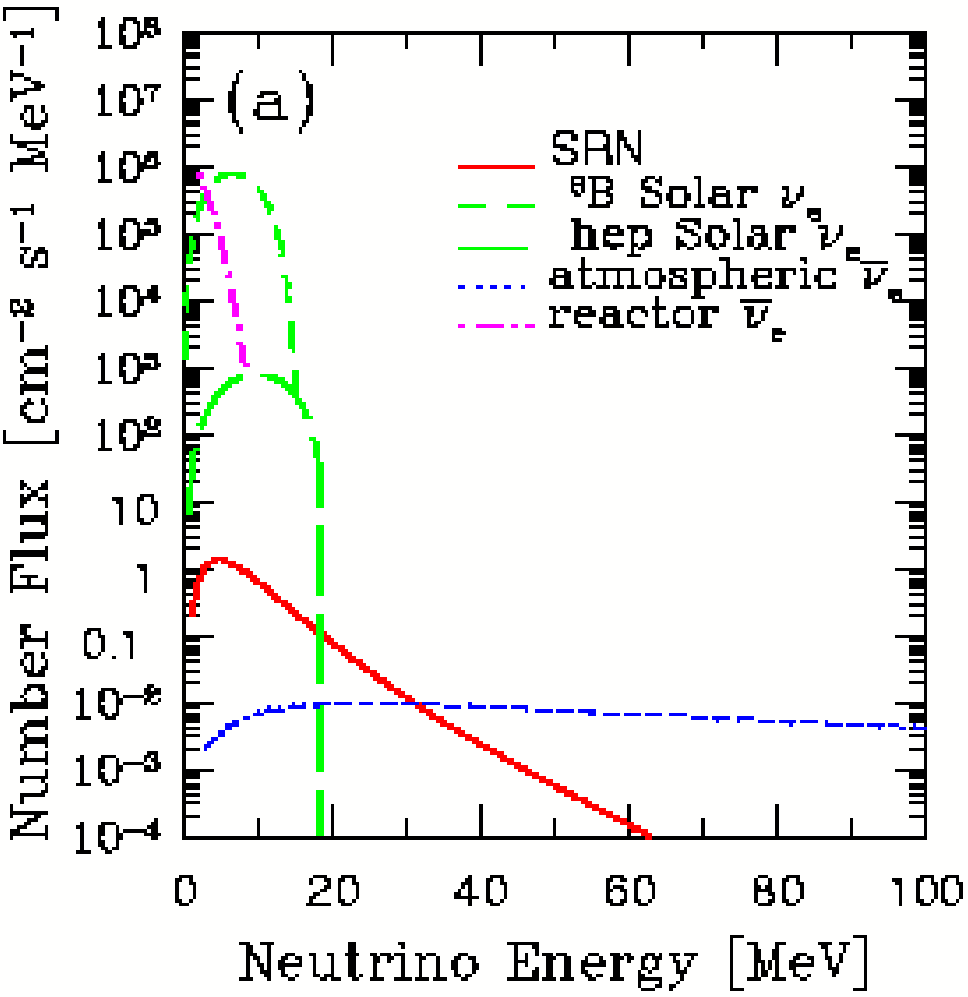


FIGURE 2.1. Number fluxes of solar, atmospheric, and SRN neutrinos as function of incident neutrino energy.

# Chapter 3
# Neutrino Astronomy

The field of neutrino astronomy holds great potential for probing different questions about the universe. Neutrinos are electrically neutral and interact very little with matter as they travel enormous distances to detectors, enabling them to provide a unique picture of the conditions existing at their place of creation. High-energy neutrinos can address different issues such as the origin of cosmic rays, the mechanisms involved in powering active galactic nuclei, the origins of gamma-ray bursts, and assist searches for new physics beyond the Standard Model.

Photon astronomy has been employed successfully as a means to study various astrophysical phenomena. The range of the high energy radiation from very distant sources, however, is reduced due to interactions with lower energy photons from the cosmic microwave background and pair production processes [41]. Neutrinos are very stable, weakly interacting particles that would provide a unique probe as they will not be deflected by magnetic fields and travel on a direct path once created. This small cross section for interaction allows neutrinos to carry information from their sources that photons cannot, however, it also means that large detectors are necessary for their detection.

In this chapter, we first examine Supernova neutrinos with energies in the MeV range; specifically we study the neutrinos that were detected from Supernova 1987a and what they have told us about the conditions where they originated as well as the properties of neutrinos themselves. Next we look at neutrinos at higher energy scales $>$ TeV from extra-galactic sources and examine the astrophysical phenomena that are capable of producing these neutrinos with such high energies. We then turn to two models of the expected ultrahigh energy (UHE) neutrino flux at the Earth. We finally

examine neutrino interactions and then turn to some UHE neutrino experiments that have a bearing on the present work.

## 3.1 Supernovae

Neutrinos from supernova (SN) explosions originating in our galactic neighborhood ($< 100\ kpc$) typically have energies on the order of  MeV and are able to be detected in currently operating neutrino telescopes. SN 1987A, a type II supernova, gave the first evidence for neutrinos being emitted from SN explosions, as events were detected by Kamiokande II [42,43], IMB [44,45], and Baskan [46]. These events occurred during a burst lasting approximately 13 seconds that took place hours before electromagnetic radiation was detected from the source. The neutrinos that were detected from SN 1987A give insight as to the conditions existing at the source since they interact very little with matter while in transit. Their detection strongly supports the model of a hot proto-neutron star forming and cooling via neutrino emissions where the neutrinos carry approximately 99% of the energy away from the explosion [47]. Neutrinos from future SN explosions will more feasibly be detected in different neutrino telescopes around the world as a part of the SuperNova Early Warning System (SNEWS) [48] with the goal of providing an early warning signal for galactic SN. The effort of future neutrino detectors to detect more events will allow for distinctions between different theoretical models of core collapse and supernova explosions.

## 3.2 Extragalactic Sources

Higher energy neutrinos ($E_\nu >$  TeV) are believed to originate from extra-galactic astrophysical sources. The input neutrino flux considered in this analysis is due to neutrinos whose origin can be traced back to protons from extragalactic sources. Protons accelerated to high energies in sources such as active galactic nuclei (AGN) and gamma-ray bursts (GRBs) produce pions through photo-meson interactions. The

charged pions then decay to produce neutrinos, leptons, and photons. What follows in this section is a brief discussion of the different astrophysical sources that may be producing UHE neutrinos that reach the Earth. The high energy cosmic rays that have been observed put constraints on the astrophysical sources from which they originate. The most plausible sources of these particles are Active Galactic Nuclei and Gamma Ray Bursts [49, 50].

### 3.2.1 Active Galactic Nuclei

Active Galactic Nuclei (AGN) are compact regions at the center of galaxies with very large luminosities, typically between $10^{42} - 10^{48}$ erg/s [51]. AGN have long been believed to be sites of high-energy particle production, including neutrinos. Many models exist to explain the neutrino production mechanism. Most of the radiation from AGN comes from their central regions and is believed to originate from matter accreting onto a central supermassive black hole. Most models describing the neutrino flux at the AGN core correlate with the mechanisms of this in-falling matter. The in-falling matter will form a shock front where protons in the AGN may be accelerated through first order Fermi acceleration. This mechanism results in highly relativistic particles with a characteristic power law spectrum. It is this proton flux that is used to determine a characteristic neutrino flux through proton-proton and proton-photon interactions near the AGN core or also in or near the jets that form along the rotation axis.

Photons with very high energies ($\sim$ TeV) have been observed from astrophysical sources. The Whipple collaboration provided the first evidence for these high energy gamma-rays from the galaxy Markarian 421 [52]. It also provided the first case for detection of TeV gamma-rays from outside our galaxy [53]. Additionally, the EGRET collaboration has detected energetic photons ($E \sim 100$ MeV) from about 40

AGN [54]. Since the initial discovery of TeV photons from Markarian 421, 68 very high energy sources ($E > 100$ GeV) have been detected using atmospheric Cherenkov telescopes, where 19 of the sources are identified as AGN [55]. The TeV photons corresponding to AGN sources have been detected by Whipple [56, 57], Durham [58], TA [59], HEGRA [60], H.E.S.S. [61–66], and MAGIC [67, 68]. These high energy photons provide observations which may be crucial towards the search for high energy neutrinos. These photons may be explained by inverse Compton scattering from energetic electrons. However, if these photons are found to be hadronic in origin, the AGN will also be sources for UHE neutrinos [69–72]

Different neutrino fluxes are predicted from different AGN models. One such representative model is that of Stecker which represents neutrinos from an AGN core [73]. The Stecker model is normalized to the extragalactic MeV photon flux measured by COMPTEL [74] and can be seen in Fig. 3.1 [1].

The results from the Antarctic Muon and Neutrino Detector Array (AMANDA) have placed limits on the diffuse neutrino flux from astrophysical sources as shown in Fig. 3.1 [1]. The flux limit for a $1:1:1$ neutrino flavor ratio is determined to be

$$E_\nu^2 \Phi_{90\%CL} \leq 2.7 \times 10^{-7} \text{ GeV cm}^{-2} \text{ s}^{-1} \text{ sr}^{-1} \tag{3.1}$$

for the energy range $2 \times 10^5$ GeV $< E < 10^9$ GeV. The AMANDA-II results have excluded a number of models for neutrino production. AMANDA is currently incorporated into the new IceCube detector (to be discussed in section 3.5.)

The Pierre Auger Observatory is a cosmic ray observatory consisting of a combination of ground and fluorescence detectors designed to detect ultra high energy cosmic rays such as those predicted to originate in AGN cores and jets. Recently the collaboration reported that the observatory has found a connection between the highest energy cosmic ray events and the location of nearby AGN [75]. The incoming direction of cosmic rays with $E > 6 \times 10^{19}$ eV were found to be correlated with positions of AGN within 75 megaparsecs. This conclusion supports the hypothesis

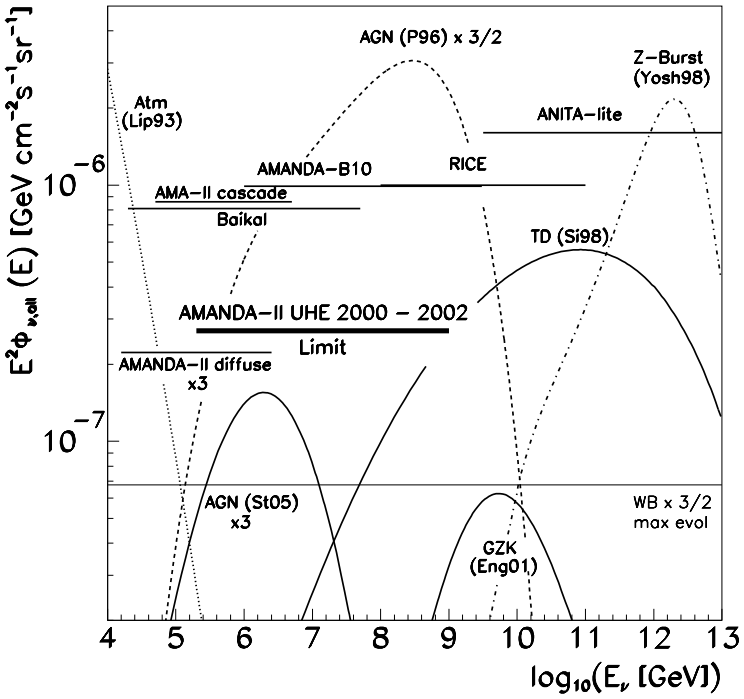


FIGURE 3.1. UHE neutrino flux limit from AMANDA-II [1].

that these cosmic rays are produced in extragalactic sources and that the corresponding flux is not substantially reduced due to interactions with the cosmic microwave background.

### 3.2.2 Gamma-ray Bursts

Gamma-ray Bursts (GRBs) are among the most luminous astrophysical events that have been observed. They have been continuously observed by astronomers since the 1970s and consist of flashes of gamma-rays that last from anywhere between a few milliseconds to minutes. The distribution of GRBs was shown to be isotropic by the BATSE detector on the Compton Gamma Ray Observatory [76] and an X-ray afterglow of GRB 970228 detected by BeppoSAX strongly supports the prediction

that GRBs are extragalactic. The intense radiation from GRBs suggest that they may also be sources for high energy neutrinos. Different models have been proposed to explain GRB origins such as failed supernovae [77] or neutron star mergers [78], or the fireball model [79].

In the fireball model, high energy electrons are accelerated in an internal shock of the expanding relativistic fireball. Synchrotron emission from these electrons result in gamma-ray emission. It is expected in the fireball model that protons will also be accelerated in the region where the electron acceleration occurs. These protons may then interact with the synchrotron photons, resulting in photomeson production. The charged pions then decay to produce high energy neutrinos. If GRBs are determined to be sources of ultrahigh energy cosmic ray protons, it is expected that there will be an associated ultrahigh energy neutrino flux as well.

## 3.3 Neutrino Fluxes

Different models exist for the incident UHE neutrino flux at the Earth that have not been excluded by the AMANDA-II results discussed in Section 3.2.1. The initial neutrino flux considered in the present work is due to cosmic-ray protons from astrophysical sources interacting with the cosmic microwave background with subsequent charged pion, muon, and neutron decays (ESS) [20]. For comparison, we also include an "upper bound" on the neutrino flux as determined by Waxman and Bahcall [19].

### 3.3.1 Waxman and Bahcall Flux

Waxman and Bahcall (WB) calculated an upper bound on neutrino fluxes from optically thin AGN jets and GRBs based on the observed cosmic-ray flux [19]. Since neutrinos can escape from a much more opaque source than protons, this is only an upper bound on the high energy neutrino flux if one assumes that all neutrino sources are identical to the high energy proton cosmic ray sources. The way this bound was

derived was starting from known information about high energy proton cosmic rays and extrapolating to how these can then source a neutrino cosmic ray flux.

Observations of cosmic-rays above $10^{17}$ eV strongly suggest that the flux is dominated at these high energies (above $\sim \ 3 \times 10^{18}$ eV) by extra-galactic sources of protons [80–82]. These protons have a flux $dN/dE \sim E^{-2}$, consistent with the assumption that the protons are accelerated via Fermi acceleration. Fermi acceleration accelerates the protons through the magnetic inhomogeneities associated with a shock wave from one of the possible extra-galactic sources such as AGN jets. Starting with the known high energy proton injection distribution this can then fix the "upper bound" on the neutrino flux. Ultrahigh energy neutrinos are proposed to also be produced at the sources of these high energy protons through photomeson interactions of the protons and subsequent charged pion decay.

The WB flux is a theoretical upper bound on such neutrinos from optically thin sources. Fixing the spectral index of the ultrahigh energy cosmic-ray flux to -2 (which is given by the protons $dN/dE$), the expected upper bound to the neutrino flux is

$$\frac{dN}{dE_\nu} \ = \ \frac{1 - 4 \times 10^{-8}}{E_\nu^2} \ \text{GeV cm}^{-2} \ \text{sr}^{-1} \ \text{s}^{-1} \tag{3.2}$$

per neutrino flavor. Fig. 3.2 shows the characteristic WB neutrino flux. An incident WB flux of neutrinos has been utilized in previous work in this area to calculate stau event rates in neutrino telescopes [3, 9]. While this upper bound does make the assumption of optically thin sources, it is quite robust since it does not require sources of neutrinos that are not able to be validated through other channels.

### 3.3.2 Cosmogenic Flux

The incident neutrino flux that we focus on in this analysis is due to cosmic-ray protons from astrophysical sources interacting with the cosmic microwave background

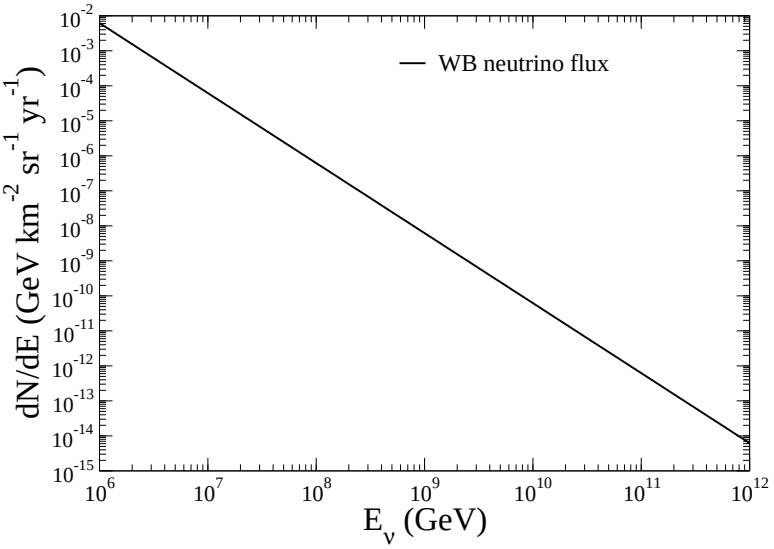


FIGURE 3.2. Waxman-Bahcall high energy neutrino flux at the earth.

(CMB),

$$p\gamma(3\mathrm{K}) \rightarrow \Delta \rightarrow N\pi$$

followed by charged pion, muon, and neutron decays. This represents a guaranteed flux of neutrinos as both the cosmic-ray flux and the 3 K CMB are measured.

Engel, Seckel, and Stanev (ESS) evaluate the neutrino flux associated with the cosmic-ray flux by tracing back cosmic-ray propagation through the background radiation [20]. The form of the protons injection spectrum is given by

$$\frac{dN}{dE} \sim E^{-\alpha} \times \exp -E/E_c \tag{3.3}$$

where $E_c$ is a cutoff energy $\sim 10^{21.5}$ eV and $\alpha$ is nominally 2. This distribution bears some similarities to the WB flux since it shares the same power law dependence coming from the injection spectrum of protons accelerated via Fermi acceleration. However, it is noticeably different due to the exponential damping factor which cuts off the injection spectrum at high energies. Starting from this injection spectrum, it is necessary to evolve the protons through over cosmological distances to generate the neutrino flux from the scattering off of the CMB. According to ESS [20], the

mean free path of the highest energy protons is only on the order of a few Mpc. This implies that the majority of the high energy neutrino flux originates early along the path of propagation. To generate a fully populated neutrino spectrum a source must be far away since after $\mathcal{O}(50)$ Mpc there are few ultra high energy protons left, and the low energy protons have a lower probability of photoproduction and thus a lower probability of generating neutrinos through decays. To simulate the interaction of the assumed injection spectrum of high energy cosmic ray protons with the CMB, ESS used the event generator SOPHIA [83]. After calculating the propagation of the protons to generate a spectrum for the neutrinos, the last step is to chose the distribution of sources. The ESS flux is based on assuming a **uniform** distribution of sources of high energy protons.

To evaluate the uncertainties on the ESS flux from cosmological evolution, the parameters of the injection spectrum (3.3), $\alpha$ and $E_c$ were varied [20]. The overall normalization of the ESS flux has an uncertainty of about 4. There is an additional uncertainty based on if the injected spectrum of cosmics is not entirely composed of protons. This will be discussed further in Section 3.3.3 where new results from Auger are reviewed. The ESS flux does not include the possibility of neutrinos being produced at the sources of the high-energy cosmic rays, thus it is a conservative estimate.

The ESS fluxes peak at high energies around $10^8$ GeV, and are for neutrinos and antineutrinos, with an electron neutrino to muon neutrino flavor ratio that depends on energy. Neutrino oscillations due to nonzero neutrino masses change the flavor ratio over the cosmological distances that they travel. At the sources for neutrino production from pion decays, the flavor ratio $\nu_e : \nu_\mu : \nu_\tau = 1 : 2 : 0$. This ratio changes to $1 : 1 : 1$ due to neutrino oscillations over the large distance from the

source to the Earth, yielding the following fluxes at the Earth

$$\begin{aligned} F_{\nu_e} &= F^0_{\nu_e} - \frac{1}{4}\sin^2 2\theta_{12}\Big(2F^0_{\nu_e} - F^0_{\nu_\mu} - F^0_{\nu_\tau}\Big) \\ F_{\nu_\mu} &= F_{\nu_\tau} = \frac{1}{2}\Big(F^0_{\nu_\mu} + F^0_{\nu_\tau}\Big) \\ &\quad + \frac{1}{8}\sin^2 2\theta_{12}\Big(2F^0_{\nu_e} - F^0_{\nu_\mu} - F^0_{\nu_\tau}\Big), \end{aligned}$$

where $F^0_i$ are fluxes at the source. The values of the neutrino mixing parameters used are presented in Table 2.1 and are representative of those used in previous studies of neutrino signals in ice due to oscillations [84]. The neutrino fluxes at the Earth assumes that the relevant mixing angle for atmospheric neutrinos $\theta_{23}$ is maximal and the angle $\theta_{13}$ is minimal. The work described here uses the ESS cosmogenic fluxes for the fluxes at the source. The cosmogenic tau neutrino flux $F^0_{\nu_\tau} = 0$ due to the threshold for tau production. The dominant process of resonant $\Delta$ production ultimately results in only $\nu_e$ and $\nu_\mu$ fluxes at the point of production. The oscillation effects assume maximal mixing between $\nu_\mu$ and $\nu_\tau$.

The effect of including neutrino oscillations enhances the ESS flux for energies $< 10^8$ GeV. Fig. 3.3 shows the cosmogenic ESS neutrino fluxes both with and without including the oscillation effects. Both standard and strong cosmological evolution for determining the neutrino fluxes are also shown. The ESS neutrino flux has a different energy dependence than that of WB. Comparing Figs. 3.2 and 3.3 shows a slight enhancement in the ESS flux over WB for $10^8 < E < 10^{11}$ GeV, corresponding to the energy regime where the neutrino detectors ANITA and ARIANNA (to be discussed in the Section 3.5) have good sensitivity, providing an impetus for the present work.

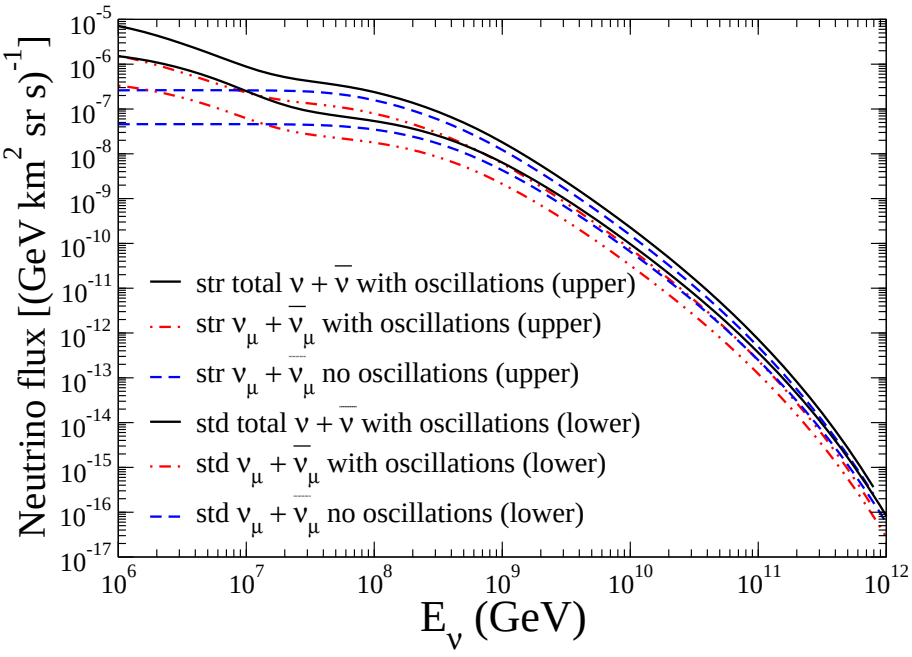


FIGURE 3.3. Cosmogenic neutrino flux with both standard and strong evolutions. The upper (lower) solid lines represent the total neutrino plus antineutrino flux for strong (standard) evolution, dashed lines are the $\nu_\mu + \bar{\nu}_\mu$ flux without including oscillation effects, and the dot-dashed lines represent $\nu_\mu + \bar{\nu}_\mu$ flux with oscillation effects included.

### 3.3.3 Updated Neutrino Flux Estimates From Auger Data

The Auger experiment has given us recently our most comprehensive understanding of the properties of ultra high energy cosmic rays. The recent data has allowed us to better understand the composition and spectrum of high energy cosmic rays. This has enabled a number of groups to update the estimates for both the WB and cosmogenic ESS neutrino flux [85, 86].

There is an uncertainty in the ESS flux mentioned in Section 3.3.2 due to the cosmological evolution of the flux. The ESS flux accounts for the cosmological evolution of cosmic ray sources assumed to be distributed uniformly. The ESS flux includes

the protons from these sources that interact with the CMB, however there is an additional component to the cosmogenic neutrino flux. If the cosmic rays consist of heavier nuclei then it is possible for these nuclei to undergo photodisintegration when interacting with the CMB. The nucleons that arise from the photodisintegration can then interact with the CMB via photopion production and thus contribute to the cosmogenic neutrino flux. However this requires knowledge of the original composition of the cosmic rays. If the CMB is completely opaque to the heavier nuclei that compose cosmic rays then they will contribute completely to the cosmogenic neutrino flux as the protons do. However if the CMB is not quite opaque to the cosmic rays then this process of photodisintegration is not completely efficient and the ESS flux estimates would be much lower.

Given the recent Auger data, Anchordoqui *et al.* [85] were able to better quantify the composition of cosmic rays and thus update the estimates of the ESS flux. They found that the most consistent fits to the data came from one of two possibilities: either the cosmic rays are completely composed of either intermediate mass nuclei or heavy nuclei, *or* they are composed almost entirely of protons with a tiny component of heavy elements. Given the difference in the cosmological evolution between these two possibilities in [85] it was shown that if cosmic rays were comprised mostly of intermediate or heavy mass nuclei, the ESS flux would be reduced by a factor of 3-100.

Another possible intriguing outcome of the Auger data, is the possible correlation between ultra high energy cosmic rays and nearby AGN [75]. With the apparent correlation to nearby AGN, the authors of [86] used the most detailed information about the local AGN to derive a bound on a diffuse neutrino flux (similar to what is done in deriving the WB flux). In [86] the diffuse neutrino flux from AGN within our horizon is found to be approximately 1/10 that of the WB flux.

The recent Auger data has obviously already had a significant impact on our understanding of the UHECR neutrino flux. In both the cosmogenic setting and the

WB type bound the Auger data has allowed for a substantial reduction in the flux of high energy cosmic neutrinos. Nevertheless given the uncertainty in the modelling of the cosmic rays still present, we will primarily use the originally derived cosmogenic neutrino flux in this work.

## 3.4 Neutrino Interactions

The neutrino signal detected in neutrino telescopes depends on neutrino interactions in the Earth. The relevant interaction in the Earth is between neutrinos and nucleons. Neutrino-nucleon interactions consist of charged-current (CC) represented by $\nu_\ell N \rightarrow \ell^- +$ anything and neutral-current (NC) represented by $\nu_\ell N \rightarrow \nu_\ell +$ anything. The details of neutrino-nucleon interactions (shown in Fig 3.4) in the Earth are essential to determine the expected signal in neutrino telescopes. Neutrinos are attenuated by SM processes as they traverse the Earth and these processes are responsible for detection either by long-range muons or showers that are produced in the telescopes. The nucleons have internal structure, thus it is necessary to describe the neutrino interactions at the parton level. The parton model was first proposed by Richard Feynman in 1969 to describe the internal structure of hadrons as comprising of point-like constituents called "partons" [87]. In the parton model, each quark carries a longitudinal fraction $x$ of the nucleon momentum $P$ where the parton momentum can be written as $p = xP$ and $0 \leq x \leq 1$. There is a probability for finding each of the quarks in the nucleon with a fractional momentum $x$. Depending on the distribution of the quarks, the neutrino can interact with each quark with some probability.

Parton distribution functions (PDFs) describe the probability density for encountering a parton $i$ in a nucleon with a specific value of the fractional momentum $x$ in the center of mass frame where the momentum transfer scale is $Q$ and are written as $f_i(x, Q^2)$. For the present work the PDFs used are determined experimentally by the CTEQ6-DIS collaboration [88]. Each nucleon consists of "valence" and "sea" quarks,

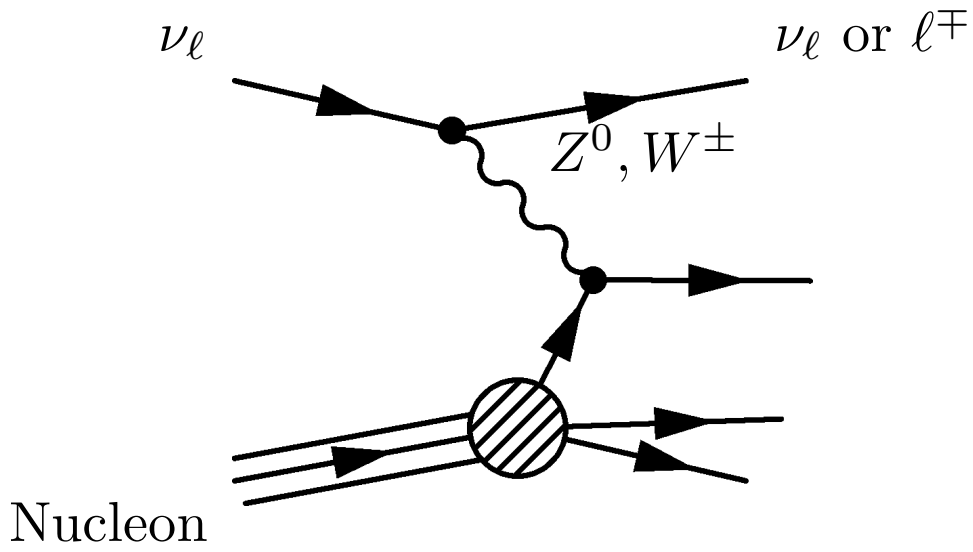


FIGURE 3.4. Neutrino-nucleon scattering.

the proton containing the three valence quarks up, up, and down (uud), and the neutron containing the three valence quarks down, down, and up (ddu). The sea quarks come from gluon splitting to $q\bar{q}$ pairs. About half of the nucleon momentum is carried by gluons. The sea quarks can have a big effect, for example, at small values of $x$. Scattering data shows that the sea quark distributions (denoted by the $s$ subscript) are all equal,

$$u_s(x) = \bar{u}_s(x) = d_s(x) = \bar{d}_s(x) = s_s(x) = \bar{s}_s(x) \equiv s(x).$$

The valence (denoted by the subscript $v$) and sea quarks are related through,

$$u(x) = u_s(x) + u_v(x)$$
$$d(x) = d_s(x) + d_v(x)$$

In the limit of a large $Q^2$, structure functions can be defined that satisfy "Bjorken scaling" where each PDF can be written as a function of the fractional momentum $x$ only, $f(x)$. This is true for a limited range of $x$ and $Q^2$ and the structure functions

are expressed as

$$\begin{aligned} F_2(x) &= \sum_i e_i^2 x f_i(x) \\ F_1(x) &= \frac{1}{2x} F_2(x), \end{aligned} \tag{3.4}$$

where $e_i$ represents the charge on the respective parton and the overall function is a sum over the charged partons. The overall quantum numbers of the nucleon in question must be preserved and are done so through the following sum rules. The proton, for example, has a charge of 1, isospin $\frac{1}{2}$, and strangeness 0,

$$\begin{aligned} \text{charge} &\rightarrow \int_0^1 \Big[\frac{2}{3}(u(x) - \bar{u}(x)) - \frac{1}{3}(d(x) - \bar{d}(x)) - \frac{1}{3}(s(x) - \bar{s}(x))\Big] dx = 1 \\ \text{isospin} &\rightarrow \int_0^1 \Big[(u(x) - \bar{u}(x)) - (d(x) - \bar{d}(x))\Big] dx = \frac{1}{2} \\ \text{strangeness} &\rightarrow \int_0^1 \Big[s(x) - \bar{s}(x)\Big] dx = 0 \end{aligned} \tag{3.5}$$

These relationships can be used to show that the ratio of the proton and neutron structure functions satisfies

$$\frac{1}{4} \leq \frac{F_2^n(x)}{F_2^p(x)} \leq 4, \tag{3.6}$$

yielding limits on the structure functions.

For the work described, the PDFs used are taken from CTEQ6-DIS [88] and are written as $xf(x, Q^2)$. For the processes analyzed, the momentum transfer $Q^2$ is a kinematic variable, meaning that the full PDFs are used (not just functions of the momentum transfer $x$). The full neutrino-nucleon cross section can be determined from folding the neutrino-parton cross section with the various distribution functions

$$\frac{d^2\sigma_{\nu N}}{dxdy} = \sum_i x f_i(x, Q^2) \frac{d\sigma_{\nu q}}{dy}, \tag{3.7}$$

where the parameter $y = \frac{E_\nu - E'_\nu}{E_\nu}$ and represents the energy loss of the incoming neutrino with the limits $0 \leq y \leq 1$. Combining everything, the overall neutrino-nucleon

cross section is

$$\frac{d^2\sigma}{dxdy} = \frac{G_F^2 M_N E_\nu}{2\pi}\Big(\frac{M_Z}{Q^2+M_Z^2}\Big)^2\Big[xq(x,Q^2) + x\bar{q}(x,Q^2)(1-y)^2\Big] \tag{3.8}$$

where $q(x,Q^2)$ and $\bar{q}(x,Q^2)$ differ for CC and NC processes.

The CC distribution functions can be written as,

$$\begin{aligned} q(x,Q^2) &= \frac{u_v(x,Q^2)+d_v(x,Q^2)}{2} + \frac{u_s(x,Q^2)+d_s(x,Q^2)}{2} \\ &+ s_s(x,Q^2) + b_s(x,Q^2) \qquad (3.9) \\ \bar{q}(x,Q^2) &= \frac{u_s(x,Q^2)+d_s(x,Q^2)}{2} + c_s(x,Q^2) \qquad (3.10) \end{aligned}$$

and NC is expressed as,

$$\begin{aligned} q(x,Q^2) &= \Big[\frac{u_v(x,Q^2)+d_v(x,Q^2)}{2} + \frac{u_s(x,Q^2)+d_s(x,Q^2)}{2}\Big](L_u^2+L_d^2) \\ &+ \Big[\frac{u_s(x,Q^2)+d_s(s,Q^2)}{2}\Big](R_u^2+R_d^2) + \Big[s_s(x,Q^2)+b_s(x,Q^2)\Big](L_d^2+R_d^2) \\ &+ \Big[c_s(x,Q^2)+t_s(x,Q^2)\Big](L_u^2+R_u^2) \qquad (3.11) \\ \bar{q}(x,Q^2) &= \Big[\frac{u_v(x,Q^2)+d_v(x,Q^2)}{2} + \frac{u_s(x,Q^2)+d_s(x,Q^2)}{2}\Big](R_u^2+R_d^2) \\ &+ \Big[\frac{u_s(x,Q^2)+d_s(s,Q^2)}{2}\Big](L_u^2+L_d^2) + \Big[s_s(x,Q^2)+b_s(x,Q^2)\Big](L_d^2+R_d^2) \\ &+ \Big[c_s(x,Q^2)+t_s(x,Q^2)\Big](L_u^2+R_u^2) \qquad (3.12) \end{aligned}$$

where,

$$\begin{aligned} L_u &= 1-\frac{4}{3}\sin^2\theta_W \quad L_d = -1+\frac{2}{3}\sin^2\theta_W \\ R_u &= \frac{-4}{3}\sin^2\theta_W \qquad R_d = \frac{2}{3}\sin^2\theta_W. \end{aligned}$$

Both the charged-current and neutral-current cross sections are obtained using CTEQ6-DIS PDFs and are shown as a function of neutrino energy in Fig 3.5. The charged-current interactions are represented by: $\nu_\ell N \rightarrow \ell^- +$ anything and the neutral-current interactions by: $\nu_\ell N \rightarrow \nu_\ell +$ anything. The resulting cross sections for different parton distribution functions are consistent up to energies of about

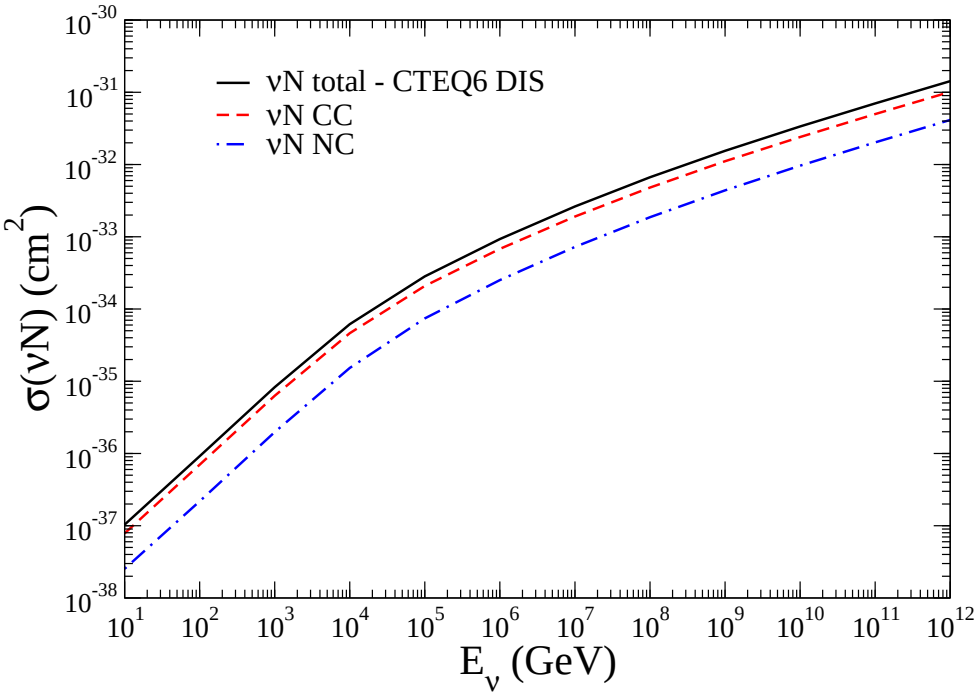


FIGURE 3.5. Neutrino-nucleon total (upper-solid), charged-current (middle-dashed), and neutral-current (lower-dot dashed) cross sections as a function of incident neutrino energy. The cross sections were calculated using the CTEQ6-DIS parton distributions.

$E_\nu = 10^{16}$ eV [72]. For $E_\nu > 10^{16}$ eV, the cross sections differ for different parton distribution functions due to the assumptions about parton behavior for small values of the momentum fraction $x$. Compared to previous work which employed CTEQ4-DIS PDFs, these results are about a few percent smaller [72].

### 3.4.1 Interaction Length and Density Profile of Earth

The neutrino-nucleon interaction length is inversely proportional to the cross section and is given by

$$\mathcal{L}_{int} = \frac{1}{\sigma_{\nu N}(E_\nu) N_A} \tag{3.13}$$

where $N_A = 6.022 \times 10^{23}$ mol$^{-1}$ $= 6.022 \times 10^{23}$ cm$^{-3}$ is Avogadro's number [72] normalized to the density of water (water equivalent, w.e.). The energy dependence on the interaction length is shown in Fig 3.6 along with the depth through the Earth for different nadir angles.

The density profile of the Earth has been determined in the Preliminary Earth Model [89] and can be represented by the following,

$$\rho(r) = \begin{cases} 13.0885 - 8.8381x^2, & r < 1221.5 \\ 12.5815 - 1.2638x - 3.6426x^2 - 5.5281x^3, & 1221.5 < r < 3480 \\ 7.9565 - 6.4761x + 5.5283x^2 - 3.0807x^3, & 3480 < r < 5701 \\ 5.3197 - 1.4836x, & 5701 < r < 5771 \\ 11.2494 - 8.0298x, & 5771 < r < 5971 \\ 7.1089 - 3.8045x, & 5971 < r < 6151 \\ 2.691 + 0.6924x, & 6151 < r < 6346.6 \\ 2.9, & 6346.6 < r < 6356 \\ 2.6, & 6356 < r < 6368 \\ 1.02, & r \leq R_\oplus. \end{cases} \tag{3.14}$$

The density $\rho$ is measured in g/ cm$^3$, the distance $r$ is measured in km from the center of the Earth, and $x$ represents the scaled radial variable $x = r/R_\oplus$ and the radius of the Earth is $R_\oplus = 6371$ km. The Earth density profile can be used to determine the column depth as a function of incident nadir angle, as shown in Fig. 3.7 where the column depth is in terms of the distance through the Earth $z$, and the density $\rho$ by $X_{col} = \rho z$. This represents the amount of Earth that an upward-going neutrino would encounter along its trajectory. The diameter of the Earth exceeds the neutrino CC interaction length for neutrinos with energy $\sim 4 \times 10^4$ GeV.

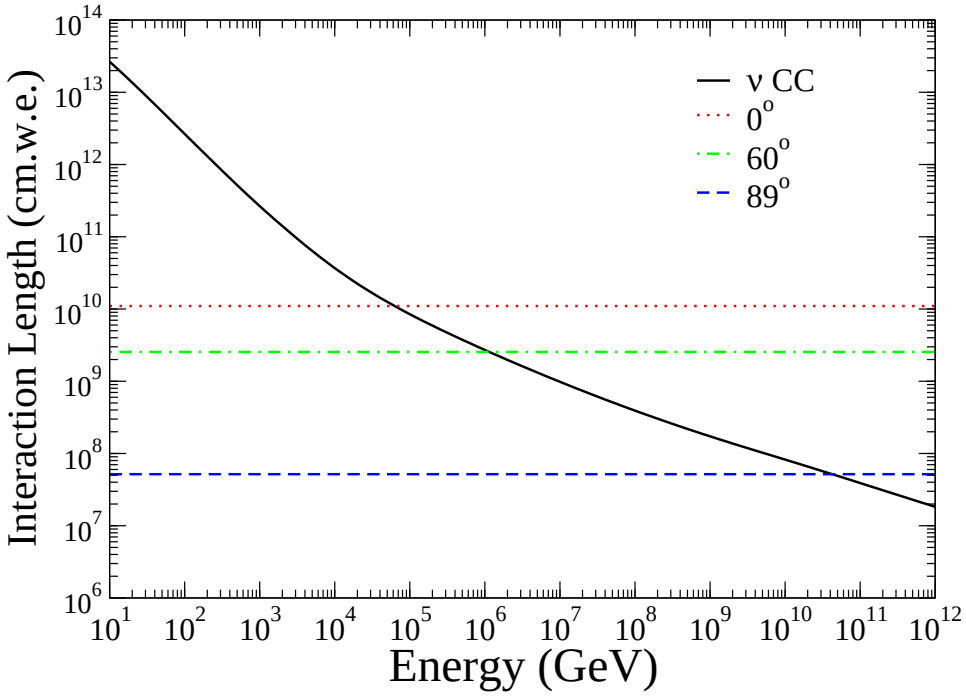


FIGURE 3.6. Neutrino-nucleon charged current interaction length as a function of incident neutrino energy compared to different depths through the Earth.All angles are measured from the full diameter. 0° is represented by the upper dotted, 60° by the middle dashed-dotted and 89° by the lower dashed line.

## 3.5 UHE Neutrino Experiments

There are many experiments that have been proposed to detect UHE neutrinos, both ground and satellite based. UHE neutrinos have a very small flux but the cross sections for interaction increase with energy as shown in Fig. 3.5. With very large detectors, it is feasible to observe some UHE neutrino events.

Neutrino telescopes that employ optical Cherenkov detectors such as AMANDA [90] and IceCube [91] with representative scales of 1 $km^3$ show promise for detecting neutrino interactions at energies $>$ TeV. In these detectors, the signal of the neutrino

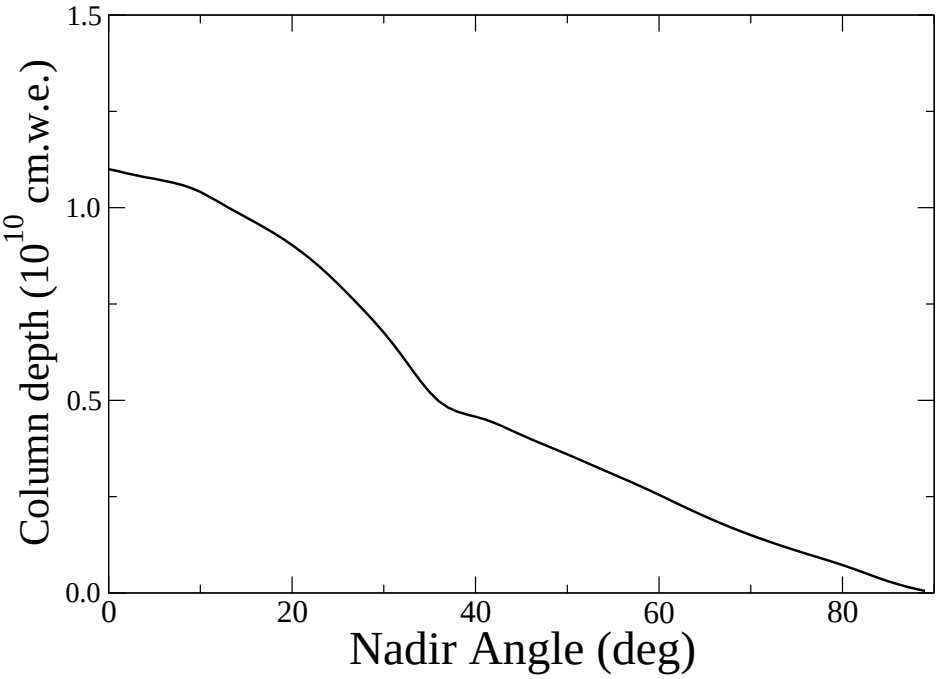


FIGURE 3.7. Column depth through the Earth as a function of incident nadir angle.

interactions occurring in rock or ice will depend on the incident neutrino energy and corresponding flavor. For example, IceCube can detect the Cherenkov signal of upward going muons that are produced during muon neutrino CC interactions. Future upgrades of IceCube such as IceCube-plus which surrounds IceCube with a ring of more conventional IceCube strings and also Hypercube which approximately doubles the number of the strings in the current IceCube design will result in even better sensitivity [92].

The future water Cherenkov neutrino telescope Astronomy with a Neutrino Telescope and Abyss environmental RESearch project (ANTARES) will reside in the northern hemisphere and will complement the IceCube detector [93]. There are other neutrino telescopes that will also employ water Cherenkov techniques such

as the Neutrino Experimental Submarine Telescope with Oceanological Research (NESTOR) [94], and the Neutrino Mediterranean Observatory (NEMO) [95]. The future km$^3$ NEutrino Telescope (KM3NeT) [96] will build on properties of these water Cherenkov telescopes. For higher neutrino energies representative of the expected cosmogenic neutrino flux (discussed in previous section), larger scale detectors are necessary to detect a significant number of events [97].

The Antarctic Impulse Transient Array (ANITA) is an experiment designed to detect cosmic neutrinos in the Antarctic ice cap [2, 98]. The ANITA experiment consists of a balloon-borne detector at an altitude of 35-40 km above the Antarctic ice sheet circling a surface area within the horizon of the instrument of about $1.5 \times 10^6$ km$^2$. The ice thickness varies between $1-3$ km, yielding a potentially observable volume of $1.5-4.5\times10^6$ km$^3$. High energy neutrinos interacting in the ice sheet will produce radio pulses via the Askaryan effect. Limits determined from a test flight of the ANITA experiment (ANITA-lite) in early 2004 and projected limits for the full ANITA experiment are shown in Fig. 3.8 along with different models for neutrino fluxes. The projected limit for ANITA delves into the model for cosmogenic neutrino production that we focus on in this analysis (discussed in Section 3.3.2), specifically into the energy range where weak interactions may begin to affect both the range of staus as well as the signals produced by staus, making it an ideal experiment to test our results (to be discussed in Chapter 5).

The Antarctic Ross Iceshelf Antenna Neutrino Array (ARIANNA) has been proposed as a neutrino detector that has an increased sensitivity of about an order of magnitude above that of existing detectors [99]. ARIANNA makes use of properties of the Ross Ice Shelf to achieve this increase in sensitivity. The shelf ice is mostly transparent to radio frequencies and the detection of downward neutrinos reflecting off the water-ice boundary is possible. The projected sensitivity of ARIANNA delves even more into the energy region for ESS neutrino flux so it could potentially provide signals for cosmogenic neutrinos.

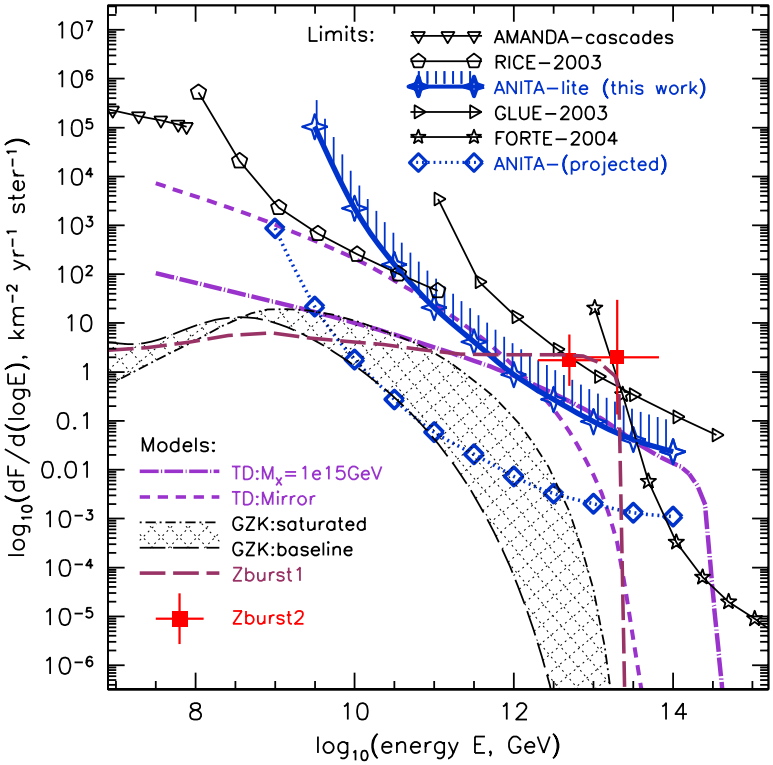


FIGURE 3.8. Limits on neutrino telescope experiments including ANITA-lite test flight and projected limit for ANITA. Neutrino fluxes from different models are also shown [2].

In addition to the ground-based neutrino scopes mentioned, there are proposals for space-based telescopes such as the Extreme Universe Space Observatory (EUSO). EUSO will use the Earth's atmosphere as a large fluorescence detector to search for cosmic rays and neutrinos with energies $> 10^{19}$ eV [100]. EUSO is currently commissioned to come online for its three year mission in 2009.

# Chapter 4
# Probing Physics Beyond the Standard Model with Neutrinos

Ultrahigh energy cosmic neutrinos could potentially probe physics beyond the Standard Model [12, 101]. Interactions of UHE neutrinos ($E_\nu \geq 10^{17}$eV) with nucleons probe center of mass energies above 14 TeV. Some fraction of these neutrinos may produce supersymmetric particles or some other exotic particles. These processes are suppressed relative to standard model processes, however, in some models interesting signals may arise from supersymmetric particles with long lifetimes. In most SUSY scenarios, particles produced in high energy collisions decay immediately into the lightest one and are thus hard to detect. However, in some low scale supersymmetric models in which the gravitino is the lightest supersymmetric particle (LSP) and R-parity is conserved, the next-to-lightest particle (NLSP) is the charged superpartner of the right-handed tau, the stau [102–108]. Due to its weak coupling to the gravitino, the stau is a long-lived particle in these models. For the supersymmetric breaking scale, $\sqrt{F} > 5 \times 10^6$ GeV, the long-lived stau could travel distances of the order of $10^4$ km before decaying into the gravitino.

In this chapter, we briefly summarize the Higgs mechanism in the SM that is responsible for electroweak symmetry breaking and how this leads to what is known as the "hierarchy problem." We then turn to an extension of the SM known as supersymmetry, specifically low scale supersymmetric models, and how UHE neutrinos can produce SUSY particles with long lifetimes that have the potential to be detected in neutrino telescopes.

## 4.1 The Standard Model and the Hierarchy Problem

The Standard Model (SM) of particle physics in its current form is incomplete. While the triumph of the SM is clearly seen insofar as it accurately describes all elementary particle interactions that have been observed and detected, it is inadequate from a theoretical standpoint at describing some of its own features. The SM contains many parameters that are only able to be determined through experiments. Many questions arise from the predicted particle spectrum, where some examples include: What is the origin and value of these parameters? Why are there three generations of matter? The fact that the SM fails to answer these questions in no way undermines its predictive power for what it can tell us. One of the main problems with the SM lies in what is known as the Higgs sector.

In the SM, electroweak symmetry breaking (EWSB) from $SU(2) \times U(1)_Y$ down to the $U(1)$ of electromagnetism is accomplished by introducing the scalar Higgs field. The Higgs field is given the potential

$$V = m_H^2 |H|^2 + \lambda |H|^4, \tag{4.1}$$

where $m_H$ is the Higgs mass parameter. This potential leads to the vacuum expectation value (VEV) for the field of $\langle H \rangle = \sqrt{-m_H^2/2\lambda}$, which is responsible for the EWSB. The Higgs particle has never been observed directly and its detection is a major effort for the Large Hadron Collider (LHC) that is scheduled to come online at CERN in 2008. Existing results of electroweak precision tests (EWPT) from experiments such as LEP point towards a light Higgs with mass of order $m_H^2 \sim -(100 \text{ GeV})^2$ [109]. The Higgs mass is subject to loop corrections from all particles that couple to the Higgs field. These quantum corrections to the SM Higgs mass show that the mass is quadratically sensitive to the cutoff of the theory $m_H^2 \sim \Lambda^2$, which could be the scale at which new physics appears and can potentially lie between the weak and Planck scales. If there were no physics beyond the SM this would imply that the Planck scale would be responsible for EWSB which is of order

$\sim 10^{18}$ GeV. If the Planck scale is taken as the cutoff for the SM, this would imply that $m_H^2 \sim m_{PL}^2$, contradicting EWPT constraints on the Higgs mass. These results require significant fine-tuning cancellation between the bare mass of the Higgs and the radiative corrections. The failure of the SM to describe such a phenomenon is what is known as the "Hierarchy problem."

The Hierarchy problem between the Planck and the electroweak scales is a major impetus for studies of physics "beyond the SM" that could provide a resolution. It is expected that this new physics will appear at energy scales that are comparable to the energy required to produce a Higgs boson. This new physics at energies above a TeV must be capable of canceling the quadratic divergences in the bare mass of the Higgs boson to provide a solution to the Hierarchy problem. One such class of theories that provide physics beyond the SM to solve the hierarchy problem is supersymmetry.

## 4.2 Supersymmetry

Supersymmetry (SUSY) (for a review see Ref. [110]) is an extension to the SM that provides new physics at the TeV scale that solves the "hierarchy problem." SUSY provides a natural extension of the space-time symmetries of the SM to include a global supersymmetry. SUSY introduces a symmetry between bosons and fermions. The relative minus sign between the boson and fermion loop corrections to the Higgs mass effectively work to cancel each other and thus offer a natural explanation for the cancellation. The attractiveness of SUSY as an extension to the SM lies in the required exact cancellation of these corrections. The SUSY transformation changes the spin state by a half unit of spin according to the relations

$$\begin{aligned} Q|\text{ boson}\rangle &= |\text{ fermion}\rangle, \\ Q|\text{ fermion}\rangle &= |\text{ boson}\rangle \end{aligned} \tag{4.2}$$

The operators $Q$ and the hermitian conjugate $Q^\dagger$ are required to be anti-commuting spinors and their algebra is defined by the following anti-commutation and commu-

tation relations

$$\begin{aligned} \{Q, Q^\dagger\} &= P^\mu, \\ \{Q, Q\} &= 0, \\ [P^\mu, Q] &= [P^\mu, Q^\dagger] = 0, \end{aligned} \tag{4.3}$$

where $P^\mu$ represents the four-momentum generator of space-time translations. The operators $Q$ and $Q^\dagger$ transform the SUSY eigenstates into one another, and the corresponding eigenstates are known as "superpartners". The collection of single-particle states in a SUSY theory that form the irreducible representations of the SUSY algebra are known as "supermultiplets", where each supermultiplet consists of two superpartners. The members of a single supermultiplet can be shown to have the same masses, gauge quantum numbers, and couplings through the commutation relations between both the squared-mass operator ($-P^2$) and the gauge group generators with $Q$ and $Q^\dagger$. It can also be shown that the members of a supermultiplet have the same number of degrees of bosonic and fermionic freedom, ensuring that the loop corrections from a single supermultiplet will exactly cancel one another. The opposite spin statistics of the superpartners allows for loop contributions to cancel the quadratic divergences of the SM proportional to the cutoff of the theory. This implies that the quadratic divergences in the Higgs mass will be proportional to the mass of the superpartners.

It is possible for terms to exist within SUSY models that violate conservation of lepton or baryon number, which may give rise to false predictions such as fast proton decay. In the Minimal Supersymmetric Standard Model (MSSM), a new property known as R-parity is introduced that is defined for a (s)particle as

$$P_R = (-1)^{3(B-L)+2S} \tag{4.4}$$

where B represents baryon number, L is lepton number, and S is spin. All particles have $P_R = +1$ while sparticles have $P_R = -1$ and R-parity exists as a multiplicatively conserved quantum number, implying that terms in the Lagrangian will only be

allowed if the product of the R-parities of the fields is +1, ruling out lepton and baryon number violating terms. R-parity is a discrete symmetry which ensures that sparticles can only be produced in pairs and that subsequent decays will end with the production of the lightest supersymmetric particle (LSP). The resulting LSP for a particular model will then be stable.

SUSY models predict that the masses of the sparticles are degenerate with their corresponding particles. If this were the case, the sparticles should have already been seen experimentally. To date, there is no direct evidence of the existence of the superpartners, indicating that SUSY must be a broken symmetry, allowing the superpartners to be heavy. The mass-splitting must not be so large that large loop corrections reappear for determining the Higgs mass parameter. For SUSY to remain a viable solution to the hierarchy problem, the mass splitting must be of the order $m_{sparticle} - m_{particle} \lesssim \mathcal{O}(1 \text{ TeV})$, ensuring that the particle spectrum is still able to be probed experimentally. This corresponds to "soft" SUSY breaking and ensures that the Lagrangian for the MSSM can be written as

$$\mathcal{L}_{MSSM} = \mathcal{L}_{SUSY} + \mathcal{L}_{soft} \tag{4.5}$$

where $\mathcal{L}_{SUSY}$ represents the Lagrangian of the unbroken SUSY and $\mathcal{L}_{soft}$ represents the SUSY violating ("soft") terms.

The SUSY breaking mechanism will determine the mass spectrum of the superpartners, and thus, the identity of the LSP through the strength of the breaking scale, $\sqrt{F}$. For models where $\sqrt{F} \gtrsim 10^{10}$ GeV, the LSP is generally the neutralino. If $\sqrt{F} \lesssim 10^{10}$ GeV, the LSP is typically the gravitino and the next-to-lightest supersymmetric particle (NLSP) is the charged superpartner of the right-handed tau, the stau. NLSP decays to the LSP are suppressed by powers of $\sqrt{F}$, implying that the lifetime can be large with a sufficiently high breaking scale.

Different SUSY models fit the constraints on $\sqrt{F}$ such that the LSP is the gravitino and the NLSP is the stau. In the present work, we focus on gauge-mediated

supersymmetry breaking (GMSB) [108, 111]. In GMSB models, the SUSY breaking mechanism is communicated via ordinary gauge interactions to the visible sector. The lifetime of the NLSP is given by

$$c\tau = \Big(\frac{F}{10^{14}\ \mathrm{GeV}^2}\Big)^2 \Big(\frac{100\ \mathrm{GeV}}{m_{\tilde{\tau}}}\Big)^5 10\ \mathrm{km}, \tag{4.6}$$

where $m_{\tilde{\tau}}$ is the stau mass. Limits on the stau mass of about 100 GeV come from its non-observation in accelerator experiments [112–115]. For $\sqrt{F} \gtrsim 10^7$ GeV, this implies that the staus may travel on the order of $10^4$ km before decaying to the gravitino.

It is important to understand the cosmological implications of the range of parameters that we are interested in. For a $\sqrt{F} \sim 10^7$ GeV this implies a gravitino mass of $m_{3/2} \sim 10$ KeV. In models of very low energy gauge mediation there typically are no cosmological problems associated with the stable gravitino. However for a gravitino mass $m_{3/2} \gtrsim$ KeV this naively overcloses the universe [108]. To safely avoid this issue one must dilute the abundance of gravitinos which typically involves lowering the reheat temperature after inflation [108].

A possibly more stringent cosmological constraint on gauge mediated models is the requirement of preserving the successes of big bang nucleosynthesis (BBN). Since the NLSP in gauge mediation can be long lived it is important that it decays before the time when standard nucleosynthesis sets in so as not to disturb its predictions. If the lifetime of the the NLSP is less than $\sim 10^7$ seconds there is typically no problem with nucleosynthesis [108]. As discussed in [116] there is an additional worry if there are hadronic NLSP decays, such as when there is a stau NLSP. The energetic nucleons created from the hadronic decays of the NLSP can significantly alter the light element abundances created through standard BBN. To safely avoid the dangers of upsetting nucleosynthesis it was found that one can change various parameters in the SUSY breaking sector [116], however typically in any model with a gravitino mass $m_{3/2} \gtrsim$

KeV it will require a reheating temperature no greater than $10^7$ TeV to satisfy all the cosmological bounds.

### 4.2.1 Stau Production through UHE Neutrino Interactions

Interactions of ultrahigh energy (UHE) neutrinos ($E_\nu \geq 10^{17}$ eV) with nucleons probe center of mass energies above 14 TeV. Some fraction of these neutrinos colliding with the earth could produce pairs of stau NLSPs which could then travel very large distances and potentially be detected in neutrino telescopes. These SUSY processes are suppressed relative to neutrino CC and NC SM processes. However, once they are produced they have the potential to travel through the earth without decaying, opening up the possibility to be detected in neutrino telescopes. The long range of the staus have the potential to compensate for the suppressed production cross section by increasing the effective detector volume and enhancing the signal.

In the models considered, the relevant process to produce a pair of staus involves the t-channel chargino or neutralino exchanges:

$$\nu N \to \widetilde{\ell}\widetilde{q}.$$

The relevant interaction is between a left-handed neutrino and either a left-handed down-type quark or a right-handed up-type quark, yielding the respective parton cross sections [3]:

$$\frac{d\sigma}{dt} = \frac{\pi\alpha}{2\sin^4\theta_W}\frac{M_{\widetilde{w}}^2}{s(t-M_{\widetilde{w}}^2)^2} \tag{4.7}$$

$$\frac{d\sigma}{dt} = \frac{\pi\alpha}{2\sin^4\theta_W}\frac{(tu-m_{\widetilde{\ell}_L}^2)m_{\widetilde{q}}^2}{s^2(t-M_{\widetilde{w}}^2)^2}, \tag{4.8}$$

where s,t, and u represent Mandelstam variables and $M_{\widetilde{w}}$, $m_{\widetilde{\ell}_L}$, and $m_{\widetilde{q}}$ represent the chargino, left-handed slepton, and squark masses. The heavier slepton and squarks promptly decay to the right-handed stau NLSP, which then has a long lifetime. Fig.

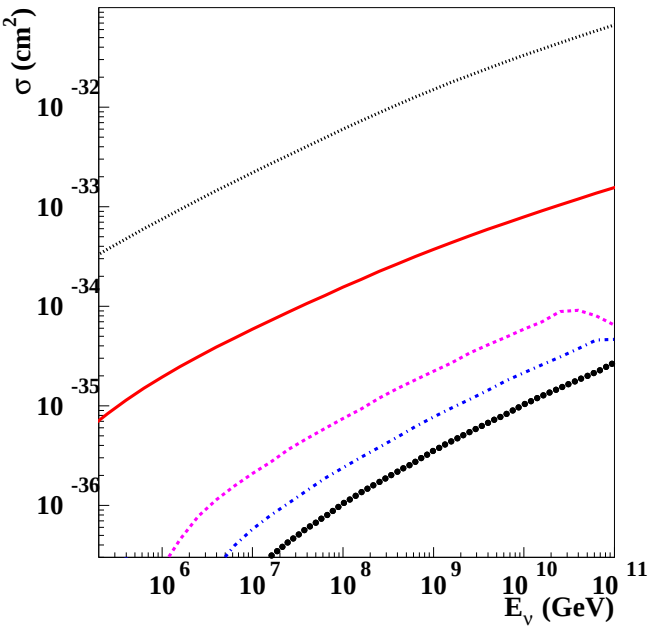


FIGURE 4.1. Stau production cross sections for $m_{\tilde{w}} = 250$ GeV and $m_{\tilde{\ell}_L} = 250$ GeV. The top dotted curve represents the total neutrino nucleon SM cross section and the middle dotted curve represents di-muon background. The bottom three curves are for stau production correspond to squark masses, from the top down, 300, 600, and 900 GeV [3].

4.1 shows the stau production cross sections for corresponding $m_{\tilde{w}} = 250$ GeV, $m_{\tilde{\ell}_L} = 250$ GeV and three squark masses $m_{\tilde{q}} = 300$ GeV, 600 GeV, and 900 GeV as determined in Ref. [3]. The cross sections are shown to be suppressed for heavier squarks. These values for the masses are representative of those in the models under consideration. The figure also shows the SM charged-current cross section for neutrino-nucleon interactions, on the order of $10^3$ times larger than the highest SUSY cross section for the 300 GeV squark. In the present work we use the cross section corresponding to a stau mass of 150 GeV and a squark mass of 300 GeV.

The stau production cross sections through neutrino-nucleon interactions in the

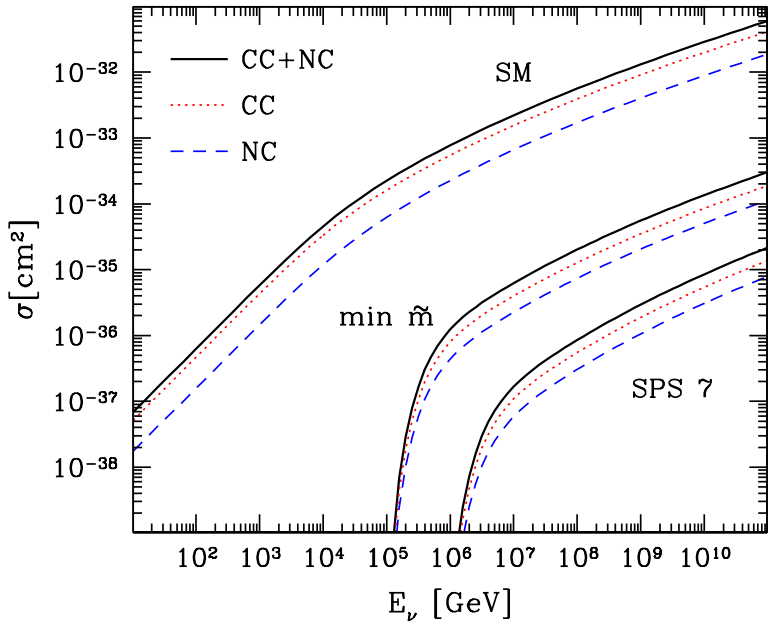


FIGURE 4.2. The total (solid), charged (dotted) and neutral (dashed) current cross sections for SM neutrino-nucleon scattering compared to the chargino and neutralino exchange for the SPS 7 benchmark point and a scenario with light squark masses of 300 GeV [4].

earth for other models are shown in Fig. 4.2 [4]. Again, neutrino-nucleon standard model processes are shown for comparison. The "min $\tilde{m}$" model assumes the light squark mass of 300 GeV, while the "SPS 7" curves are specific to other parameters not considered in this analysis.

The lifetime of the stau within this class of SUSY models is given by Eq. 4.6 where $m_{\tilde{\tau}}$ is the mass of the stau and $\sqrt{F}$ is the SUSY breaking scale. The present work probes a region of parameter space given by the stau lifetime equation where stau decays in the Earth are suppressed. In Fig. 4.3, we show the parameter space $(m_{\tilde{\tau}}, \sqrt{F})$ and the region for which staus with certain energy ($10^8$, $10^{10}$, $10^{12}$ GeV) have long enough lifetimes, $\gamma c\tau = 10^7$ cm w.e., to travel through the Earth without decaying for a nadir angle of 88°. Different nadir angles, or column depths, correspond to different range of these parameters. Clearly there is a large parameter space that

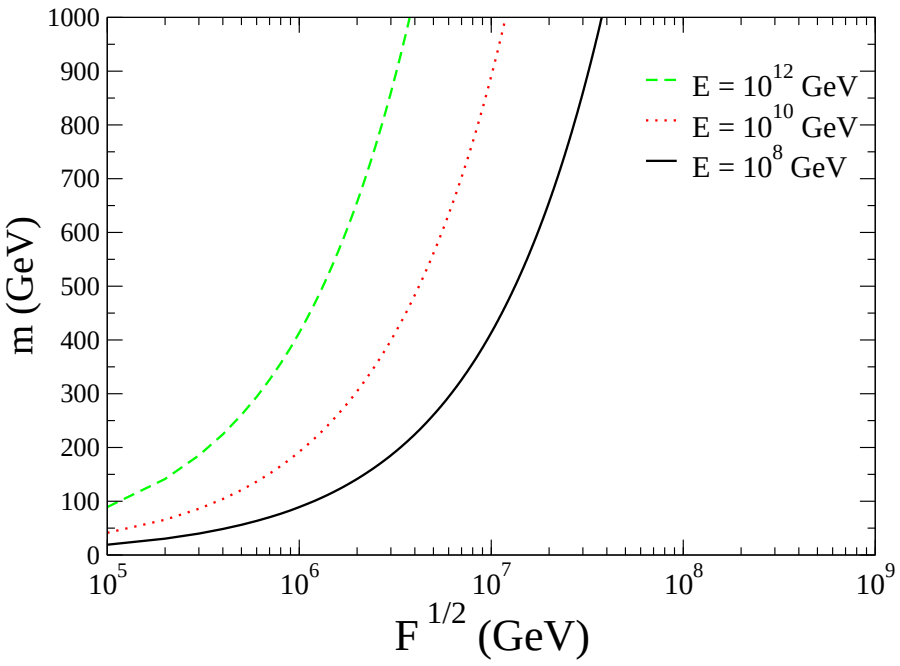


FIGURE 4.3. The parameter space of stau mass $m$ and decay parameter $F^{1/2}$ probed with stau decay lengths corresponding to a column depth of $10^7$ cm w.e. The area to the the right of each curve is the parameter space probed by demanding that stau does not decay as it traverses this column depth.

we are probing for which staus do not decay, but they may interact via charged-current interactions, if there is a maximal mixing between the right-handed and left-handed stau (to be discussed in the next chapter). Here we consider the case when stau mass is 150 GeV and the supersymmetric breaking scale $F^{1/2}$ =$10^7$ GeV.

# Chapter 5
# Lepton and Stau Energy Loss and Range

## 5.1 Introduction

The detection of staus in large ice-based neutrino detectors through neutrino nucleon interactions very strongly depends on the particle's lifetime and range. Thus, to determine the signal it is crucial to determine the particle's energy loss and effective range as it traverses the Earth. These large detectors that are applicable to this analysis such as ANITA [2, 98] and ARIANNA [99] are designed to detect neutrinos with very large energies ($> 10^8$ GeV) that originate in high energy extra galactic sources. In low-scale SUSY models the high energy neutrinos interact with nucleons in the Earth to produce the high energy stau NLSPs. Once the stau is produced, it has the potential to travel distances on the order of tens to $10^4$ km before decaying to the gravitino LSP. In this chapter, we investigate the charged slepton energy loss as it traverses the Earth.

The average electromagnetic energy loss of a particle that traverses a distance $X$ (in g/ cm$^2$) is given to first order in E by

$$-\frac{dE}{dX} \simeq \alpha + \beta E \tag{5.1}$$

where $E$ represents the particle energy, $\alpha$ is nearly constant and represents energy loss due to ionization, and $\beta = \sum_i \beta_i$ represents radiative energy losses due to photonuclear, pair production, bremsstrahlung and weak (NC) processes. The radiative energy loss parameter $\beta$ can be represented by

$$\beta^i(E) = \frac{N}{A} \int_{y_{min}}^{y_{max}} dy\, y \frac{d\sigma^i(y, E)}{dy} \tag{5.2}$$

where the superscript $i$ indicates the contributions from the various radiative processes. The parameter $y$ represents the fractional slepton energy loss in the radiative

interaction given by

$$y = \frac{E - E'}{E} \tag{5.3}$$

where $E$ is the incoming particle energy and $E'$ is the outgoing particle energy. The $\alpha$ parameter that represents energy loss due to ionization is nearly constant as a function of the mass of the particle [117]

$$\alpha \simeq 2 \times 10^{-3} \text{ GeVcm}^2/\text{g} \ . \tag{5.4}$$

At low energies, where $\beta E \ll \alpha$, either the lifetime or the energy loss due to ionization will determine the stau range. Fig 5.1 shows the crossover in the parameter space where the ionization energy loss or the stau lifetime becomes important [5]. The two regions in the figure are separated by a curve described by $c\tau\rho = m_{\tilde{\tau}}/\alpha$ where $\rho$ is taken to be the density for standard rock (2.65 g/ cm$^3$), $m_{\tilde{\tau}}$ is the mass of the stau, $c\tau$ represents the stau lifetime as given in the equation

$$c\tau = \Big(\frac{\sqrt{F}}{10^7 \text{ GeV}}\Big)^4 \Big(\frac{100 \text{ GeV}}{m_{\tilde{\tau}}}\Big)^5 10 \text{ km}, \tag{5.5}$$

and finally $\sqrt{F}$ represents the SUSY breaking scale, which as shown in the previous chapter can be as low as $10^7$ GeV for the models considered. For higher stau energies ($> 10^6$ GeV), the radiative processes dominate the stau energy loss and therefore the stau range.

In this chapter, we outline the contributions from the relevant processes and show that for stau energies $10^6 - 10^{12}$ GeV the photonuclear interaction gives the largest contribution to the stau energy loss within a certain region of parameter space as determined in Ref. [5]. Photonuclear and pair production processes are shown to have a $1/m_{\tilde{\tau}}$ dependence. A useful paramaterization towards determining the resulting range of the stau is presented. We then turn to the weak interaction contribution to both staus and leptons and show how the energy loss and therefore range are affected. Specifically we show that the neutral current weak interaction contribution

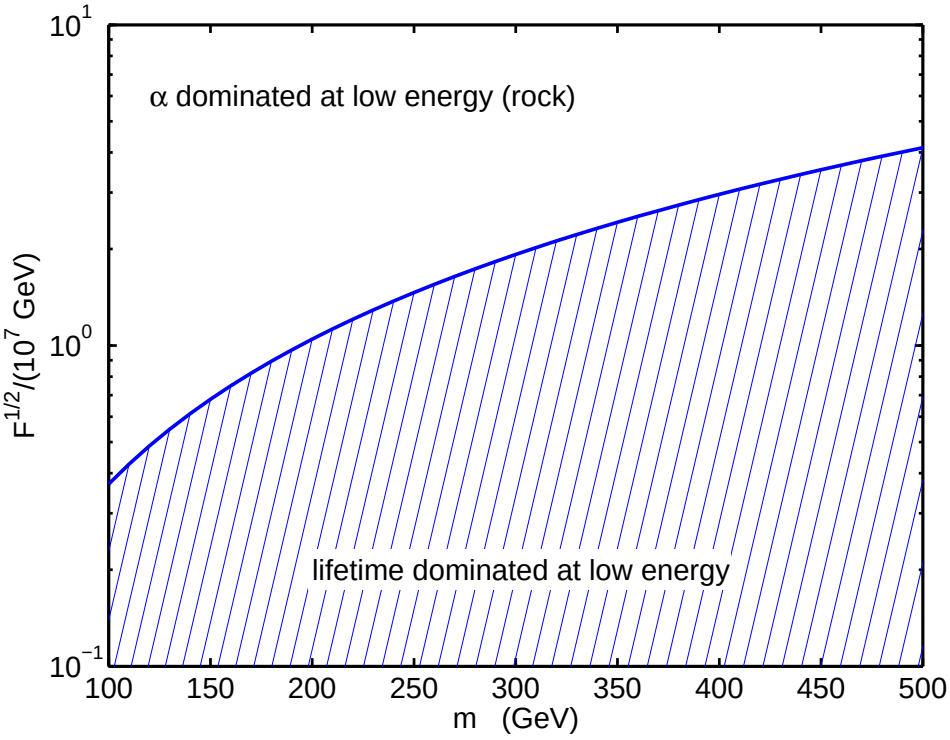


FIGURE 5.1. Parameter space in $(m_{\tilde{\tau}}, \sqrt{F})$ in which the stau range is dominated by either ionization energy loss or the lifetime, when $\beta E \ll \alpha$ [5].

to the stau energy loss is much smaller than the photonuclear contribution. However, the charged current contribution may become the dominant process for staus with energies above $\sim 10^9$ GeV, effectively reducing the stau range for these energies if weak interactions were not included. We show how these results depend on the details of the supersymmetric couplings considered. The lepton energy loss and range is not significantly affected by including weak interactions.

## 5.2 Photonuclear, Pair Production, and Bremsstrahlung Processes

Photonuclear, pair production, and bremsstrahlung processes have all been studied in detail in Ref. [5]. Photonuclear processes describe high energy stau interactions

with nuclei in the Earth via virtual photon exchange,

$$\widetilde{\ell}N \rightarrow \widetilde{\ell}X \tag{5.6}$$

resulting in a stau with a reduced energy. Pair production processes describe $e^+e^-$ production in collisions of staus with nuclei. Bremsstrahlung describes radiation from a charged stau due to acceleration of the stau in the presence of nuclei. The contributions from all three processes to the stau energy loss parameter $\beta$ is detailed in Fig. 5.2.

The energy loss due to the photonuclear process is calculated using the deep inelastic scattering formalism [118] and the differential cross section is given by

$$\begin{aligned} \frac{d^2\sigma(x,Q^2)}{dQ^2\,dx} &= \frac{4\pi\alpha^2}{Q^4}\frac{F_2(x,Q^2)}{x}\Bigg[1-y+\frac{y^2}{4} \\ &\quad -\left(1+\frac{4m_{\tilde{\tau}}^2}{Q^2}\right)\frac{y^2(1+4M^2x^2/Q^2)}{4(1+R(x,Q^2))}\Bigg], \end{aligned} \tag{5.7}$$

where $F_1$ and $F_2$ represent the nucleon electromagnetic structure functions as parameterized by Abramowitz, Levin, Levy and Maor (ALLM) [119]. This expression uses $-Q^2 = q^2 = (k-k')^2$, $x = Q^2/(2p\cdot q)$, $y$ as defined in Eq. (5.3), $m_{\tilde{l}}$ as the stau mass, and $M$ as the nucleon mass. The term $R(x,Q^2)$ represents the deviation from the Callan-Gross relation $F_1(x,Q^2) = \frac{1}{2x}F_2(x,Q^2)$ (as previously shown in Eq. (3.4)) by

$$R(x,Q^2) = \frac{\left(1+\frac{4M^2x^2}{Q^2}\right)F_2(x,Q^2) - 2xF_1(x,Q^2)}{2xF_1(x,Q^2)}, \tag{5.8}$$

which has been shown to be small and is taken to be $R(x,Q^2) = 0$ [120]. The kinematic limits of integration for the evaluation of the photonuclear energy loss are determined to be

$$\begin{aligned} \frac{m_{\tilde{\tau}}^2y^2}{1-y} &\leq Q^2 \leq 2MEy - [(M+m_\pi)^2 - M^2] \\ \frac{\left[(M+m_\pi)^2-M^2\right]}{2ME} &\leq y \leq 1-\frac{m_{\tilde{\tau}}}{E} \end{aligned} \tag{5.9}$$

The result for $\beta^{nuc}$ for a stau mass of 150 GeV is shown in the upper curve in Fig. 5.2 along with the results for $\beta$ due to pair production and bremsstrahlung processes [5]. We see that the largest contribution to the stau energy loss for energies considered comes from photonuclear processes. Fig. 5.3 shows the mass dependence on the photonuclear energy loss, which scales as $1/m_{\tilde{\tau}}$.

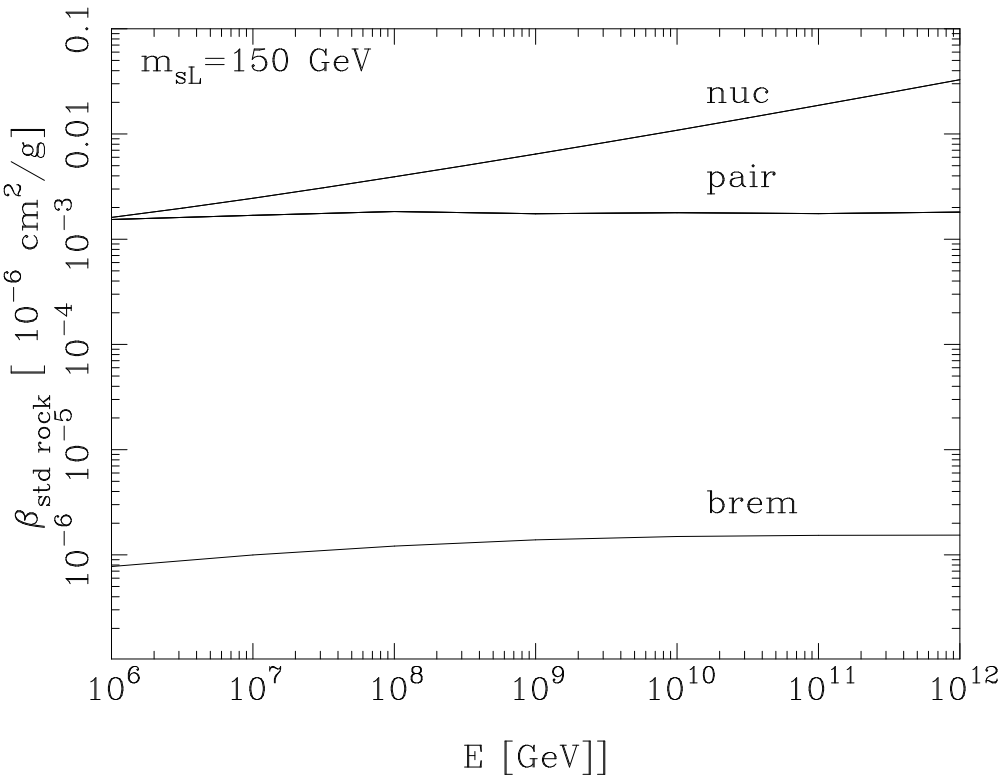


FIGURE 5.2. Energy loss of stau due to photonuclear (nuc) interactions, pair production (pair) and bremsstrahlung (brem) for a stau mass of 150 GeV [5].

The contribution due to pair production is determined to be the same as that in the fermion case. The result for staus is found by using the fermion result as presented in Ref. [121], with the substitution that $m_{\mu} \rightarrow m_{\tilde{\tau}}$. Fig. 5.2 details the result for a 150 GeV massive stau and it is noted that the pair production contribution to the energy loss is not as significant as the photonuclear. Fig. 5.3 shows the mass dependence of $\beta^{pair}$ and a $1/m_{\tilde{\tau}}$ behavior is again found.

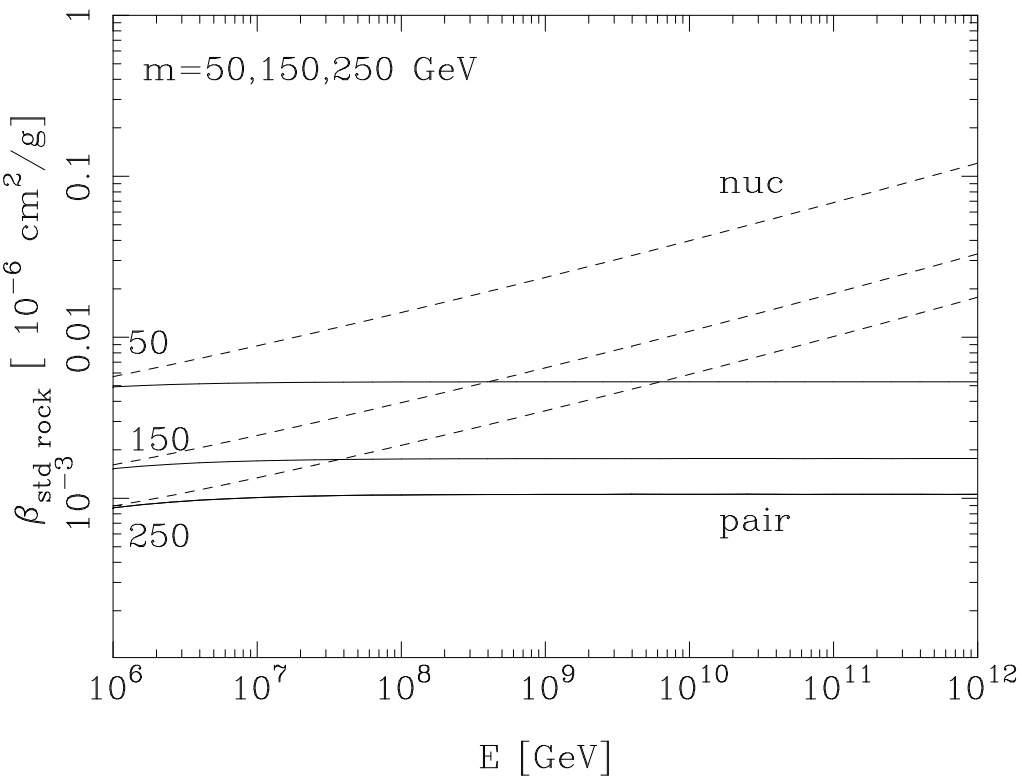


FIGURE 5.3. Energy loss of stau due to photonuclear and pair production for $m_{\tilde{\tau}} = 50$ GeV, $m_{\tilde{\tau}} = 150$ GeV and $m_{\tilde{\tau}} = 250$ GeV [5].

The Bremsstrahlung contribution to the energy loss is determined to be significantly smaller than photonuclear and pair production. $\beta^{brem}$ is determined to have an additional factor of $1/m_{\tilde{\tau}}$ dependence [122] as is noted in Fig. 5.2. The evaluation of $\beta^{brem}$ follows from Ref. [123].

## 5.3 Weak Interactions

Neutral current and charged current cross sections are relevant in two different ways. Neutral current interactions only shift the stau energy and can therefore be incorporated into $\beta$. By contrast, the charged current interactions remove the stau, in the process producing a sneutrino. The sneutrino then decays, presumably to another stau. We do not include stau regeneration because of the several steps decreasing

energy. Neutral current and charged current cross sections of staus are discussed in this section, as well as the results for the cross sections for taus. In the following subsections we evaluate the weak interaction cross sections and the contributions to the energy loss $\beta$.

### 5.3.1 Neutral Current Cross Sections

The neutral current cross section that describes the interactions of charged sleptons ($\tilde{\tau}$) with nucleons via exchange of $Z^0$ boson is given by

$$\begin{aligned}\frac{d^2\sigma^{NC}(\tilde{\tau}N)}{dxdy} &= \frac{G_F^2}{\pi} ME\Big(\frac{M_Z^2}{Q^2+M_Z^2}\Big)^2 \sin^2 2\theta_W \\ &\cdot \Big(\alpha_f + \beta_f \cos 2\theta_f\Big)^2 \Big[2x\Big(1-\frac{y}{2}\Big)^2 \\ &- \Big(\frac{xy^2}{2} + \frac{m_{\tilde{\tau}}^2 y}{ME}\Big)\Big] F_1^{NC} \ . \end{aligned} \tag{5.10}$$

The parton fractional momentum is $x$ and $y$ is the fraction of slepton energy loss. The quantities $\alpha_f$ and $\beta_f$ are the couplings of staus to gauge bosons [124]

$$\alpha_f = \frac{1}{4}\Big(3\tan\theta_W - \cot\theta_W\Big) \tag{5.11}$$

and

$$\beta_f = \frac{1}{4}\Big(\tan\theta_W + \cot\theta_W\Big) \ . \tag{5.12}$$

The scalar partner of the right-handed tau may not be a mass eigenstate. The angle $\theta_f$ parameterizes the mixing between scalar partners of the right-handed and left-handed tau, where $\sin\theta_f = 0$ means that the mass eigenstate quasi-stable stau is purely made of the partner of the right-handed tau. In principle, $\sin\theta_f$ need not equal zero. We take $\sin\theta_f = 1$ for the neutral-current process in the figures below to evaluate the maximal effect in the charged current case, since $W$'s couple only to left-handed fermions and their scalar partners. The range of $(\alpha_f + \beta_f \cos 2\theta_f)^2$ is such that

$$0 \leq \Big[(\alpha_f + \beta_f \cos 2\theta_f)^2/(\alpha_f+\beta_f)^2 \equiv r_{NC}\Big] \leq 1.38 \ . \tag{5.13}$$

For the neutral current structure functions, we have taken $2xF_1 = F_2$. We use the same definition for the charged current structure functions as well. For neutral currents,

$$F_1^{NC} = \frac{1}{2}(v_i^2 + a_i^2)[q_i(x,Q^2) + \bar{q}_i(x,Q^2)] \tag{5.14}$$

with

$$v_i = T_3 - 2e_i \sin^2\theta_W \tag{5.15}$$

$$a_i = T_3 \tag{5.16}$$

for weak isospin assignments $T_3 = \pm 1/2$ and electric charge $e_i$. We use CTEQ6 parton distribution functions [88] with a power law extrapolation of these distributions for $x < 10^{-6}$ of the form $x^{-\lambda_i}$, where $i$ denotes quark or antiquark flavor [71, 72, 125]. The values we use for $\lambda_i$ are given by:

| | $u\bar{u}, d\bar{d}$ | $s\bar{s}, b\bar{b}$ | $c\bar{c}$ |
|---|---|---|---|
| $\lambda_i$ | $-0.0276 \cdot \ln Q + 0.1784$ | $\lambda_u + 0.0054$ | $\lambda_u + 0.0094.$ |

The kinematic limits on the variables of integration, $y$ and $Q^2$ (for small $y$) are given by

$$\begin{aligned} \frac{m_{\tilde{\tau}}^2 y^2}{1-y} \leq\ & Q^2 \leq 4E^2(1-y) - \frac{m_{\tilde{\tau}}^2(2-y)^2}{1-y} \\ \frac{\left[(M+m_\pi)^2 - M^2\right]}{2ME} \leq\ & y \leq 1 - \frac{m_{\tilde{\tau}}}{E} \end{aligned} \tag{5.17}$$

In Fig. 5.4 we show the neutral-current cross sections for stau masses of 50 GeV and 250 GeV, for $\sin\theta_f = 1$. We also show the muon, tau and neutrino neutral current cross sections for comparison. We note that the cross section for taus is almost indistinguishable from the muons because the masses of taus and muons are small compared to the energy considered. The stau cross sections have weak $m_{\tilde{\tau}}$ dependence.

We see that the stau NC cross section is almost an order of magnitude smaller than the neutrino case for $\sin\theta_f = 1$ and $m_{\tilde{\tau}} = 250$ GeV at $E = 10^6$ GeV. The difference comes from the couplings as well as from the $y$ dependence of the differential cross section. The ratio of neutrino to stau neutral-current couplings, including spin averaging, yields about a factor of 2. At small $y$, the differential cross section, $d\sigma/dy$, for neutrinos is larger by about a factor of 5 than for the stau. The average $y$ for staus decreases with increasing stau mass from $< y > \approx 0.13$ for $m_{\tilde{\tau}} = 50$ GeV to $< y > \approx 0.06$ for $m_{\tilde{\tau}} = 250$ GeV.

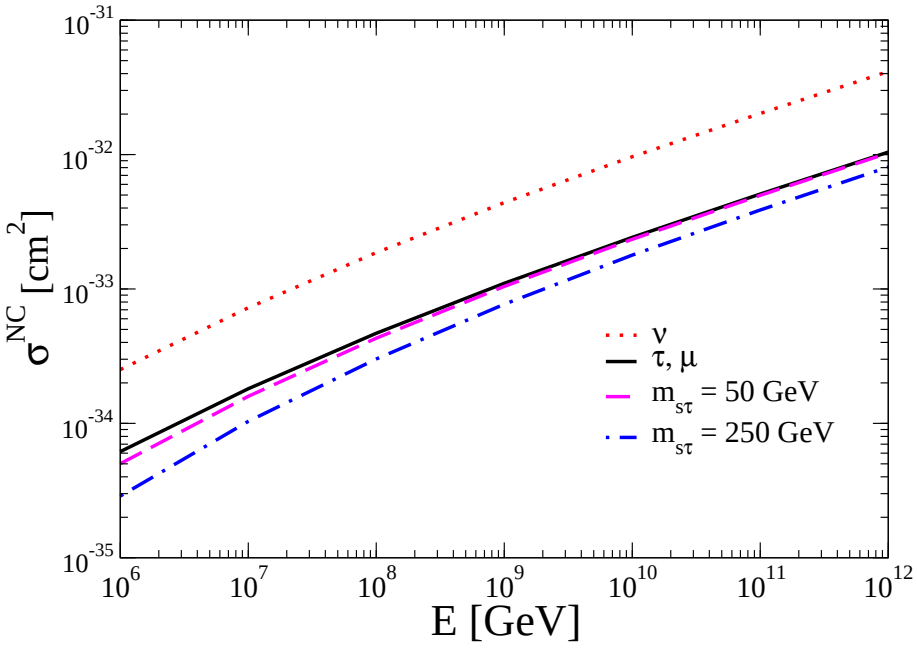


FIGURE 5.4. Neutral-current cross sections for neutrino, tau, muon, and stau for $m_{\tilde{\tau}} = 50$ GeV and $m_{\tilde{\tau}} = 250$ GeV, with $\sin\theta_f = 1$.

### 5.3.2 Charged Current Cross Sections

The charged-current cross section of staus with nucleons via exchange of charged boson is given by

$$\begin{aligned}\frac{d^2\sigma^{CC}(\tilde{\tau}N)}{dxdy} &= \frac{G_F^2}{\pi}\Big(\frac{M_W^2}{Q^2+M_W^2}\Big)^2 \sin^2\theta_f ME \\ &\cdot \quad F_1^{CC}\Big[2x\Big(1-\frac{y}{2}\Big)^2 \\ &- \quad \frac{y}{2ME}\Big(m_{\tilde{\tau}}^2 + m_{\tilde{\nu}}^2 + MExy\Big)\Big]. \end{aligned} \tag{5.18}$$

Since we are interested in considering the upper limit on the stau cross section, we take $\sin^2\theta_f = 1$, however, the value of $\sin\theta_f$ is unknown. For the charged current, the conventional normalization of the structure functions is

$$\begin{aligned} F_1^{CC} &= [q_i(x,Q^2) + \bar{q}_j(x,Q^2)] \\ F_3^{CC} &= 2[q_i(x,Q^2) - \bar{q}_j(x,Q^2)] \end{aligned} \tag{5.19}$$

and we use the kinematic limits

$$\begin{aligned} \frac{m_{\tilde{\nu}}^2 y}{1-y} - m_{\tilde{\tau}} y \;\le\; Q^2 &\le 4E^2(1-y) - m_{\tilde{\tau}}^2(2-y) \\ &- \frac{m_{\tilde{\nu}}^2(2-y)}{1-y} \\ \frac{\Big[(M+m_\pi)^2 - M^2\Big]}{2ME} \;\le\; y &\le 1 - \frac{m_{\tilde{\nu}}}{E}, \end{aligned} \tag{5.20}$$

where $m_{\tilde{\tau}}$ represents the mass of the incoming stau and $m_{\tilde{\nu}}$ represents the outgoing sneutrino. For the stau process we take $m_{\tilde{\nu}} - m_{\tilde{\tau}} = 50$ GeV, with $m_{\tilde{\tau}}$ as 50 GeV and 250 GeV.

In Fig. 5.5 we show the charged-current (CC) cross sections for the stau with mass 50 GeV and 250 GeV, and for the tau, muon and neutrino for comparison. We note again that the cross section for stau has a weak mass dependence. The cross sections for taus and muons are indistinguishable due to the small masses relative to

the energies we consider. The charged lepton CC cross section is about a factor of 2 smaller than the neutrino case, due to the spin averaging. The energy dependence of the stau cross section is stronger than for the tau and muon.

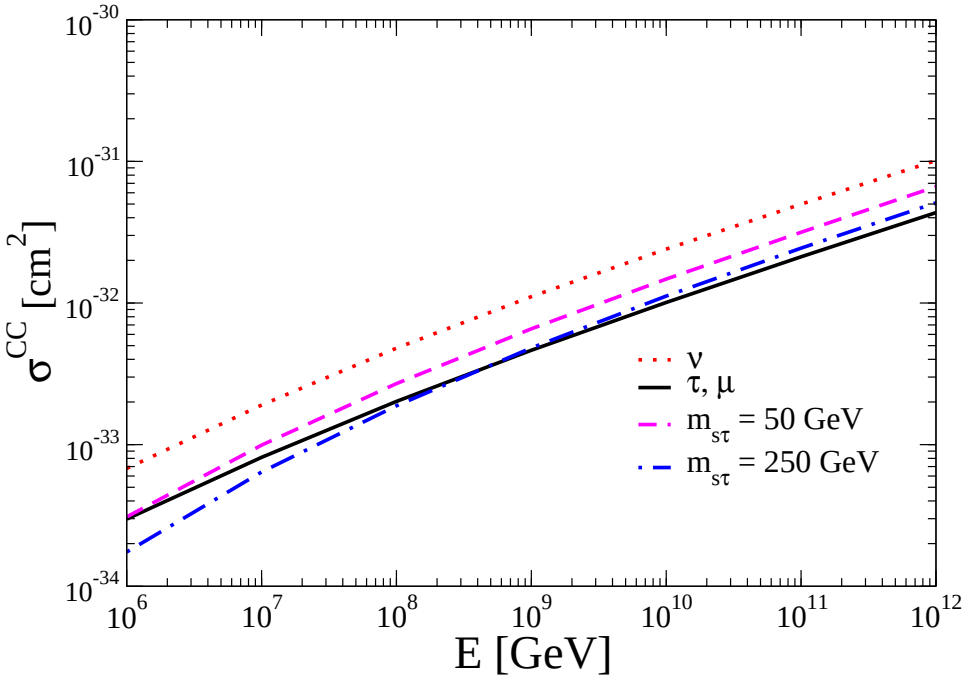


FIGURE 5.5. Charged-current cross sections for neutrino, tau, muon, and stau for $m_{\tilde{\tau}} = 50$ GeV and $m_{\tilde{\tau}} = 250$ GeV, with $\sin\theta_f = 1$.

### 5.3.3 Application to Energy Loss

The energy loss $\beta$ for neutral current interactions can be found at a fixed initial charged lepton or stau energy from Eq. (5.2). In Fig. 5.6 we show our results for $\beta^{NC}$ for muon, tau and stau with masses 50 GeV and 250 GeV, with $\sin\theta_f = 1$. The values of $\beta^{NC}$ for the muon and tau are very close in value, as they were for the cross

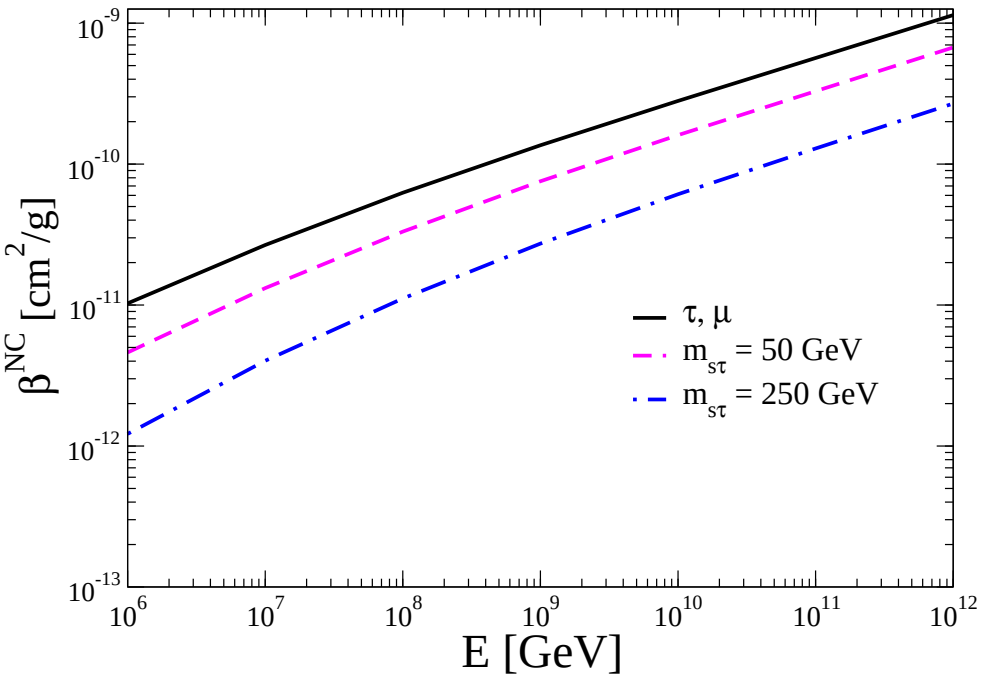


FIGURE 5.6. Neutral-current $\beta$ for tau, muon, and stau for $m_{\tilde{\tau}} = 50$ GeV and $m_{\tilde{\tau}} = 250$ GeV, with $\sin\theta_f = 1$.

sections. Using the relation

$$\beta \simeq N\langle y\rangle\sigma(E) \ ,$$

we estimate the average value for $y$ to be about 0.2 for tau and muon neutral-current interaction. We see that the stau case is smaller than tau by about a factor of 3 at $10^6$ GeV when we use a stau mass of 50 GeV. We show below that the photonuclear contribution to $\beta$ is at least an order of magnitude larger than $\beta^{NC}$ for staus. For muons and taus, the photonuclear $\beta^{nuc}$ is larger than $\beta^{NC}$ by a factor $\sim 10^3 - 10^4$.

In Fig. 5.7 we show the mass dependence of $\beta^{NC}$ for different initial energies. We note that the mass dependence is weaker than $1/m_{\tilde{\tau}}$ for $m_{\tilde{\tau}} \leq 200$ GeV. For masses larger than 200 GeV, the $1/m_{\tilde{\tau}}$ scaling works reasonably well.

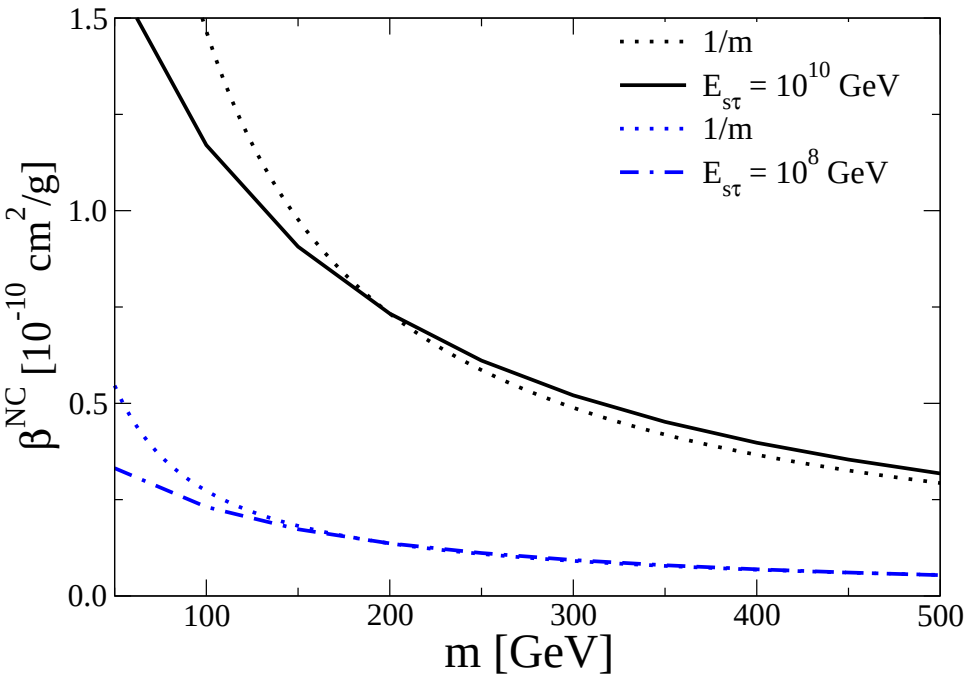


FIGURE 5.7. Mass dependence of neutral-current $\beta$ for stau with a stau mass range of $m_{\tilde{\tau}} = 50$ GeV to $m_{\tilde{\tau}} = 500$ GeV, with $\sin\theta_f = 1$.

In charged-current processes the initial and final states are different so we use $N\sigma^{CC}$, the inverse of the effective interaction length, instead of $\beta$. We show in Fig. 5.8 the results for $N\sigma^{CC}$ together with $\beta^{nuc}$. These figures are plotted using $\sin\theta_f = 1$ and for a sneutrino mass 50 GeV more massive than the stau. For the sneutrino mass between 5 GeV and 150 GeV more than the stau mass, the cross section changes by a factor of $\sim 1/2 - 2$. In the following, we show only a 50 GeV mass difference.

Comparing the scales associated with weak interaction and electromagnetic processes shows that the charged-current interactions become significant at higher energies, in contrast to the neutral current interactions. For a stau mass of 250 GeV and $\sin\theta_f = 1$, this corresponds to energies higher than about $4 \times 10^9$ GeV. For the lighter

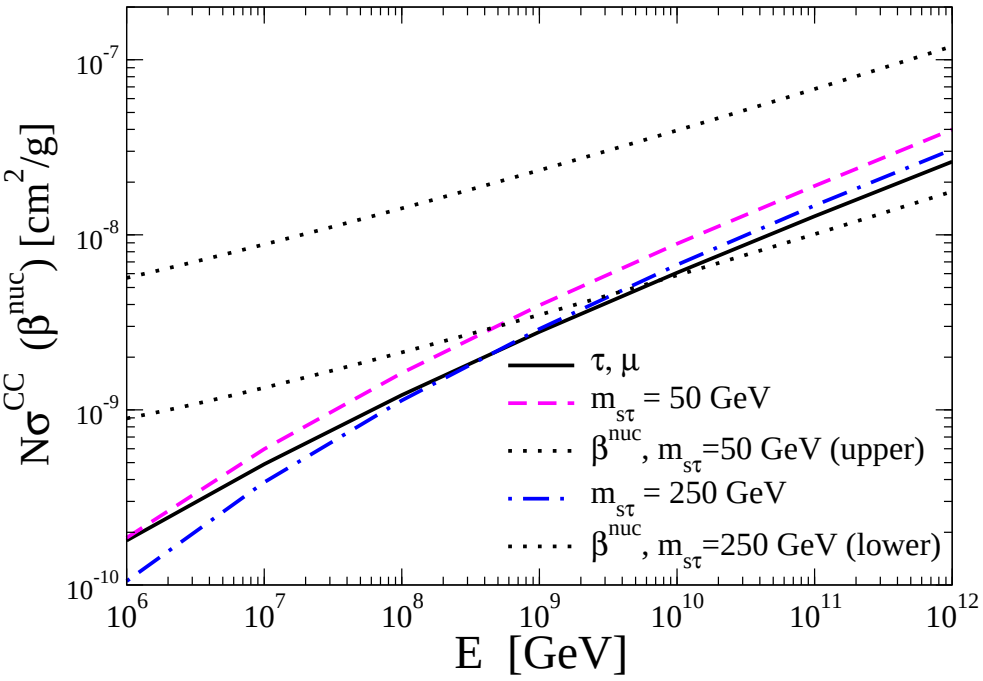


FIGURE 5.8. Charged-current interaction length for tau, muon, and stau for $m_{\tilde{\tau}} = 50$ GeV and $m_{\tilde{\tau}} = 250$ GeV, with $\sin\theta_f = 1$. The sneutrino mass is $m_{\tilde{\tau}} + 50$ GeV. Also shown are photonuclear energy loss parameters for the two stau masses.

50 GeV stau mass, the charged current process does not contribute significantly for energies up to $10^{12}$ GeV. The opportunity for charged current interactions to become relevant comes from the fact that the charged current cross section is less sensitive to the stau mass than the photonuclear energy loss parameter $\beta$.

A comparison of Figs. 5.8 and 5.6 verifies our assertion that the weak neutral current contribution to $\beta$ for staus is not important. This is also true for tau energy loss.

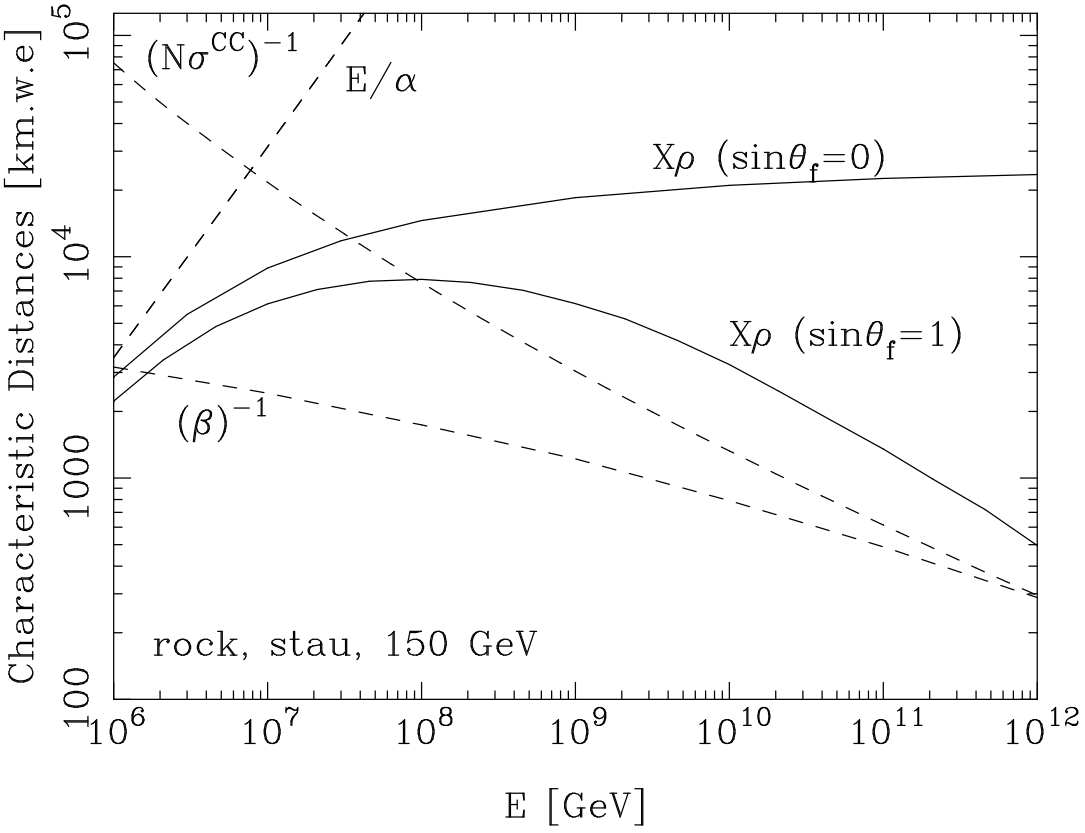


FIGURE 5.9. Characteristic distances in km water equivalent units (dashed) and ranges (solid) for staus in rock, for $m_{\tilde{\tau}} = 150$ GeV, $\sin\theta_f = 0$ and 1, and $\sqrt{F} = 10^7$ GeV. The minimum stau energy is $E_0 = 10^3$ GeV. The sneutrino mass is $m_{\tilde{\tau}} + 50$ GeV.

## 5.4 Characteristic Distances and Range

Because $\beta^{NC} \ll \beta^{nuc}$ for staus, taus and muons, we neglect neutral current interactions in our evaluation of the range. For staus, the charged current interaction length is roughly comparable to $1/\beta$ for some stau masses, so we include the charged current interactions in our Monte Carlo evaluation of the particle range. A one dimensional Monte Carlo is used as in Refs. [126] and [5], compared to the MUSIC code [127], which employs a three dimensional simulation. This approximation is justified given that the two approaches give very similar results as shown in Ref. [126]. To find the

stau range we wish to use the Monte Carlo to find the energy loss given the differential equation

$$-\frac{dE}{dX} = \alpha + \frac{N_A}{A}E\int_0^{y_{cut}} dy\; y\frac{d\sigma}{dy} + \frac{N_A}{A}E\int_{y_{cut}}^{1} dy\; y\frac{d\sigma}{dy} \tag{5.21}$$

where the first two terms are treated continuously and the third term stochastically. The terms in the differential equation are separated into both a continuous and a stochastic piece to better model the effect of a single interaction taking away a large fraction of the initial energy. The ionization loss is well modelled by the continuous piece. Processes in which a particle loses a large amount of energy in a single interaction are treated using both the continuous and stochastic pieces. The variable $y$ represents the fractional energy loss of the stau. To simulate as accurately as possible $y_{cut}$ should be as small as possible, however this increases the Monte Carlo time necessary to simulate. To optimize the simulation a value of $y_{cut} = 10^{-3}$ was chosen as done in Ref. [127].

The Monte Carlo computer program computes survival probabilities $P(E, E_0, X')$ for a particle incident with energy $E$ which survives a distance $X'$ with $E > E_0$. The range is defined by

$$X(E, E_0) \equiv \int dX' P(E, E_0, X') \; . \tag{5.22}$$

We have taken $E_0 = 10^3$ GeV for the figures shown here for staus.

A parameterization for stau range due to the dominant photonuclear and pair production processes is given as a solution to 5.2 with a constant $\beta$, but uses an energy dependent $\beta$ in the solution. This parameterization is presented in [5] and it is found from a fit to the average range as determined by the Monte Carlo program. The range is parameterized by,

$$X(E, E_0) \;\; = \;\; \frac{1}{\beta}\ln\Big[\frac{\alpha + \beta E}{\alpha + \beta E_0}\Big] \tag{5.23}$$

with the following new definitions,

$$\begin{aligned} \beta &= b_0 + b_1 \ln(E/E_0) \ , \\ b_0 &= 5 \times 10^{-9} \ \mathrm{cm}^2/\mathrm{g}(150 \ \mathrm{GeV}/m_{\tilde{\tau}}) \ , \\ b_1 &= 2.8 \times 10^{-10} \ \mathrm{cm}^2/\mathrm{g}(150 \ \mathrm{GeV}/m_{\tilde{\tau}}) \ . \end{aligned} \tag{5.24}$$

In Fig. 5.9, we show characteristic distances associated with stau interactions in rock. The curves are evaluated for $m_{\tilde{\tau}} = 150$ GeV and the decay parameter $F^{1/2} = 10^7$ GeV, where the lifetime is determined by

$$c\tau = \left( \frac{F}{10^{14} \ \mathrm{GeV}^2} \right)^2 \left( \frac{100 \ \mathrm{GeV}}{m_{\tilde{\tau}}} \right)^5 10 \ \mathrm{km} \ . \tag{5.25}$$

The lifetime is not relevant for this energy range for $m_{\tilde{\tau}} = 150$ GeV and $F^{1/2} = 10^7$ GeV: $Ec\tau\rho/m_{\tilde{\tau}} \simeq 3 \cdot 10^4$ kmwe for $E = 10^6$ GeV. A distance which is relevant, which also grows with energy, depends on the ionization energy loss parameter $\alpha$ through $d \sim E/\alpha$, shown in the figure. We also show the charged current interaction length $(N\sigma^{CC})^{-1}$ and the distance characterized by $\beta^{-1}$, the electromagnetic energy loss parameter. We show the range for 150 GeV staus with no charged current contributions ($\sin\theta_f = 0$) and with maximal charged current contributions ($\sin\theta_f = 1$). At low energies, the ionization energy loss dominates, but for $E \sim 10^8$ GeV, the charged current interaction dominates the evaluation of the range if $\sin\theta_f = 1$. The range does not precisely equal the charged current interaction length because the electromagnetic energy loss is still a factor, shifting the initial stau energy to lower energies.

Fig. 5.10 shows the stau ranges in rock for $m_{\tilde{\tau}} = 150$ and 250 GeV, again for minimum stau energy of $10^3$ GeV and $F^{1/2} = 10^7$ GeV. The upper curves show the range when charged current interactions are vanishing, while the lower curves have maximal charged current interactions. Fig. 5.11 again shows the stau ranges in rock, but for $m_{\tilde{\tau}} = 250$ GeV, a minimum stau energy of $10^8$ GeV and $F^{1/2} = 10^7$ GeV.

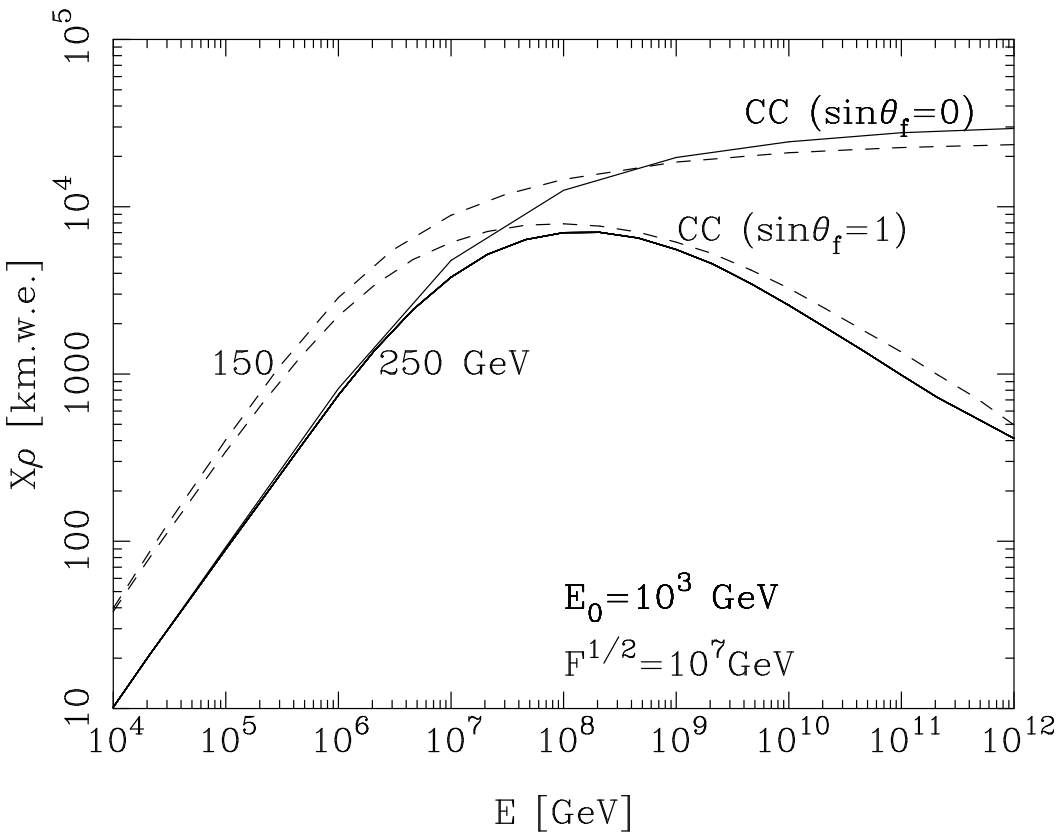


FIGURE 5.10. Range of stau in rock, for $m_{\tilde{\tau}} = 150$ and 250 GeV, $\sin\theta_f = 0$ and 1. The lifetime is here governed by $\sqrt{F} = 10^7$ GeV, and the minimum stau energy is $E_0 = 10^3$ GeV. The sneutrino mass is $m_{\tilde{\tau}} + 50$ GeV.

Again, the upper curve shows vanishing charged current interactions and the lower curve shows maximal charged current interactions.

Finally, in Fig. 5.12 we show the characteristic distances for taus in rock and the tau range. The lifetime governs the range at low energies, while electromagnetic energy loss dominates at high energies. Because the charged current interaction length is small compared to $(\beta\rho)^{-1}$, the tau range changes very little with charged current interactions included. We do not find a decrease in the range in rock or water near $E = 10^{12}$ GeV as suggested in Ref. [128, 129]. This is due to the fact that using just the scales, e.g., $(\beta\rho)^{-1}$ or the CC interaction length, is insufficient to accurately

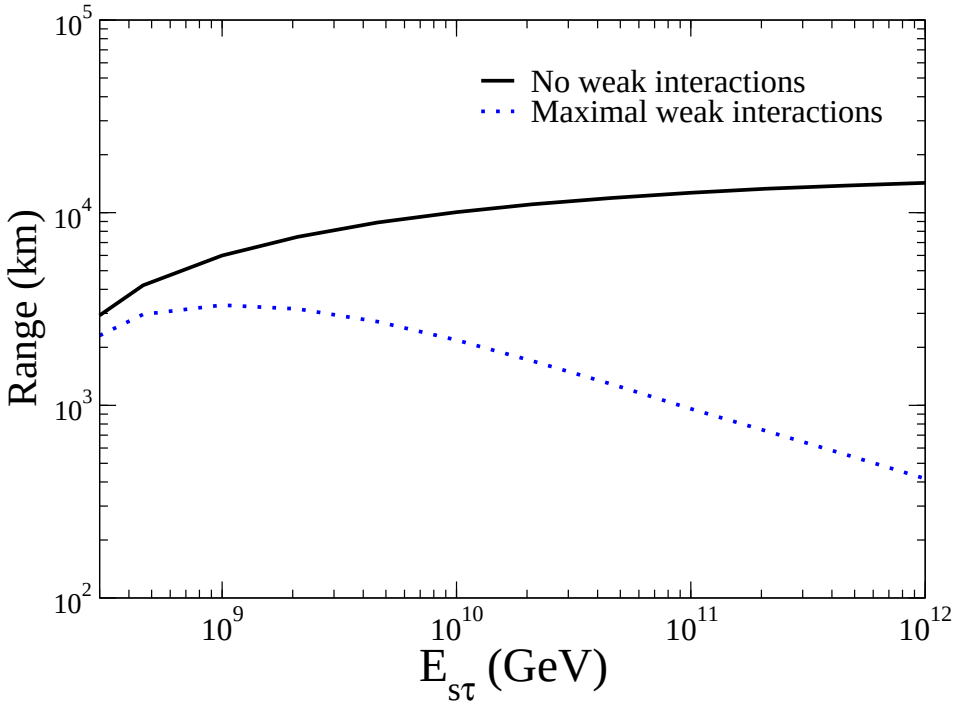


FIGURE 5.11. Range of stau in rock, for $m_{\tilde{\tau}} = 250$ GeV, $\sin\theta_f = 0$ (solid) and 1 (dotted). The lifetime is here governed by $\sqrt{F} = 10^7$ GeV, and the minimum stau energy is $E_0 = 10^8$ GeV. The sneutrino mass is $m_{\tilde{\tau}} + 50$ GeV.

compute the range. We have directly evaluated the tau range via Eq. 5.22, where the probability includes stochastic effects in the tau propagation.

## 5.5 Discussion

We have shown that weak interactions have the potential to play an important role in stau detection by neutrino telescopes, however, the effect is strongly energy dependent. Our results are based on a sneutrino mass 50 GeV more massive than the stau, and we considered $\sin\theta_f = 1$.

Recent work on stau signals [3, 4] has focused on the IceCube detector. The stau

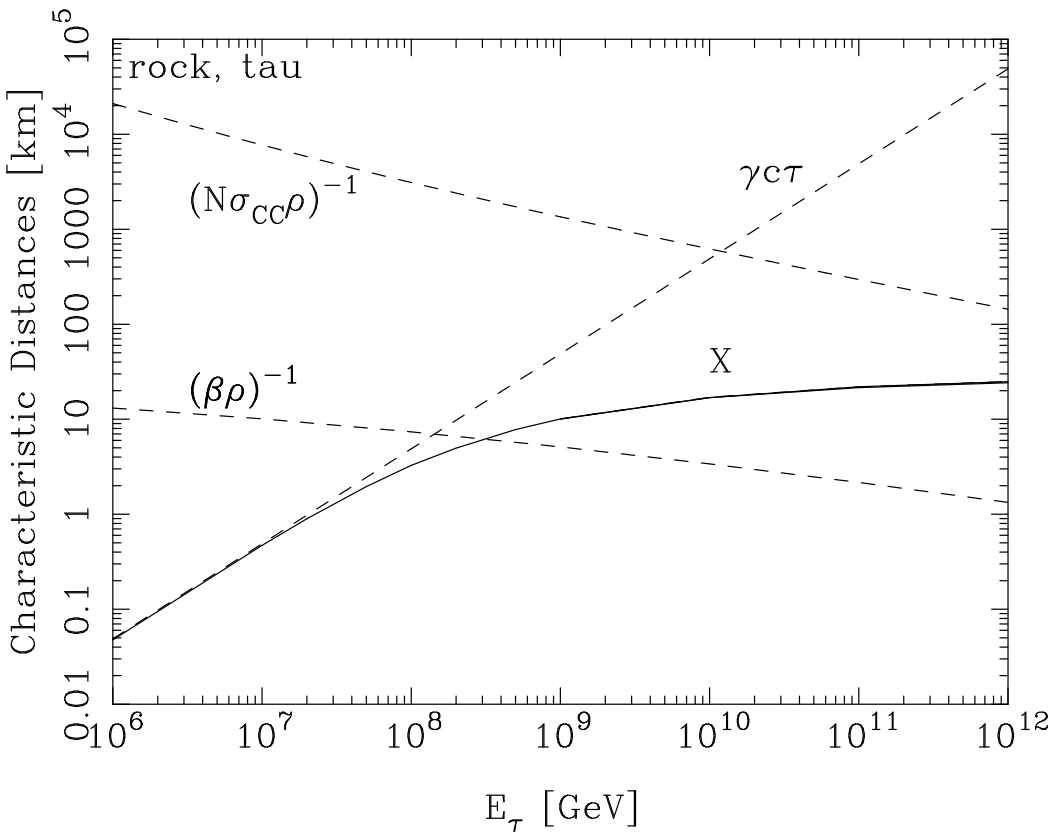


FIGURE 5.12. Characteristic distances (dashed) and tau range in rock (solid) in km. By including the charged current interaction length, the tau range is unchanged on the scale of the figure.

pair event rate depends on the effective volume for creation of a pair of staus. The effective volume scales approximately with the stau range which depends on energy.

Refs. [3,4] show that the signal events come from energies fairly near the threshold for squark production because of the falling neutrino fluxes. In these studies, an incident $E^{-2}$ neutrino flux is assumed. The threshold depends on squark masses: for $m_{\tilde{q}} = 300 - 900$ GeV, the energy threshold is between a few$\times 10^5 - 10^6$ GeV. For $E = 10^6$ GeV, even a maximal charged current cross sections with $m_{\tilde{\nu}} = m_{\tilde{\tau}} + 50$ GeV doesn't affect the stau energy range dramatically. For $m_{\tilde{\tau}} = 150$ GeV, maximal CC interactions reduce the range by 22% at $10^6$ GeV, and by 31% at $10^7$ GeV. The

effect is less pronounced for $m_{\tilde{\tau}} = 250$ GeV. When $\sin\theta_f = 1$ for $m_{\tilde{\tau}} = 250$ GeV and $F^{1/2} = 10^7$ GeV, the range is reduced by 9% and 21% for $E = 10^6$ and $10^7$ GeV, respectively. Based on these reductions in the range, the thresholds in the $10^5 - 10^6$ GeV energy range and steeply falling fluxes, event rate estimates without including weak interactions are reasonably reliable.

Efforts to try to detect staus with higher energy thresholds are potentially strongly influenced by charged current interactions, where the range can be as much as two orders of magnitude shorter than the range evaluated without charged current interactions. A detector such as the Antarctic Impulse Transient Array (ANITA) [2] is sensitive to stau energies larger than $\sim 10^8$ GeV. Designed to use a radio antenna suspended by a balloon $\sim 37$ km over the south pole ice, the primary goal of the experiment is to detect cosmogenic neutrinos incident just below the horizon which interact with the ice. The goal is to detect the radio Cherenkov signal produced by neutrino weak interactions which refracts on its way out of the ice. Staus would also make a signal by weakly interacting in the ice.

Weak interactions play a role for ANITA signals in two ways. As noted above, the most important feature of weak interactions is to produce the signal itself. For electromagnetic interactions, only a small amount of energy will be deposited in the shower over the area of $\sim 10^6$ km$^2$. Neutral current interactions have a larger energy deposition necessary for detection. Charged current interactions have the largest energy deposition. Only neutral current processes will contribute to the signal if $\sin\theta_f = 0$, while charged current processes contribute with increasing values of $\sin\theta_f$. The maximum contribution from charged current interactions occur when $\sin\theta_f = 1$. For this maximum value of the mixing angle, $\sigma^{CC}/\sigma^{NC} \sim 10$, meaning that the probability for interactions of staus in the ice is increased by a factor of 10 over the case of $\sin\theta_f = 0$.

A second effect for ANITA signals is that charged current weak interactions may attenuate the stau flux in transit to the ice in view of the detector. By incorporating

the attenuation of the GZK neutrino flux [20] as it traverses the Earth, the stau production cross section [9] and the stau interactions on the way to the detector, we find that the stau flux attenuation at $10^9$ GeV ranges from 1 at $0^\circ$ to $\sim 1/3$ at a $10^\circ$ angle measured relative to the horizon [15]. For energies of $10^{10}$ GeV, attenuation causes the stau flux to be lowered by a factor of $\sim 1/10$ with maximal charged current interactions for an angle of $10^\circ$ below the horizon. The factor of 10 increase in the signal due to the stau CC interactions in ice is sufficient to compensate for the attenuation as well as enhance the signal when the full range of energy is considered.

To summarize, weak interaction effects are small in the range of energies relevant to the IceCube detector. Recent event rate estimates [3, 4, 9] for IceCube will be reduced by less than $\sim 30\%$ for $E = 10^6 - 10^7$ GeV by including maximal weak interactions. The potential for observing staus at higher energies, for example, by the ANITA detector, is enhanced by maximal weak interactions. The enhancement is due to the high energy charged current cross section which becomes increasingly important as the stau energy increases above $10^8$ GeV. A detailed investigation of the ANITA signal from stau pairs, and for the proposed ARIANNA [99] telescope is described in the next chapter on lepton and stau fluxes. Signals of staus from several energy regimes may impose constraints on this class of supersymmetry models with quasi-stable staus in the future.

# Chapter 6
# Lepton and Stau Fluxes

## 6.1 Cosmogenic Neutrino Flux and Attenuation

Ultrahigh energy cosmogenic neutrinos have the potential to produce supersymmetric particles (or some other exotic particles) through neutrino-nucleon interactions as they traverse the Earth and/or in the detector. These neutrinos originate from cosmic ray protons interacting with the cosmic microwave background,

$$p\gamma(3\mathrm{K}) \rightarrow \Delta \rightarrow N\pi$$

followed by charged pion, muon and neutron decays. This flux is guaranteed as cosmic ray fluxes are measured as well as the 3K microwave background. Details of the cosmogenic neutrino fluxes, including neutrino oscillations that are used in this work, are discussed in Chapter 2.

Cosmic neutrino fluxes that reach the Earth get attenuated as neutrinos traverse the Earth toward the detector due to weak interactions, primarily the charged-current (CC) interactions. Similarly, once created in neutrino-nucleon interactions, the stau flux also gets attenuated when staus interact weakly. The size of these effects can be seen in Fig. 6.1, where we show neutrino interaction length [71, 72, 125] and the stau interaction length [13] due to their charged-current interactions with isoscalar nucleons, as a function of incident energy. This figure shows the stau charged current cross section with maximal weak interactions. We also show for reference the column depth for nadir angles of 60° and 80°.

The evaluation of the stau or lepton flux that reaches the detector depends on the initial neutrino flux and attenuation, the particle's production cross section, lifetime, and energy loss as discussed in the previous chapters. In this chapter the procedure

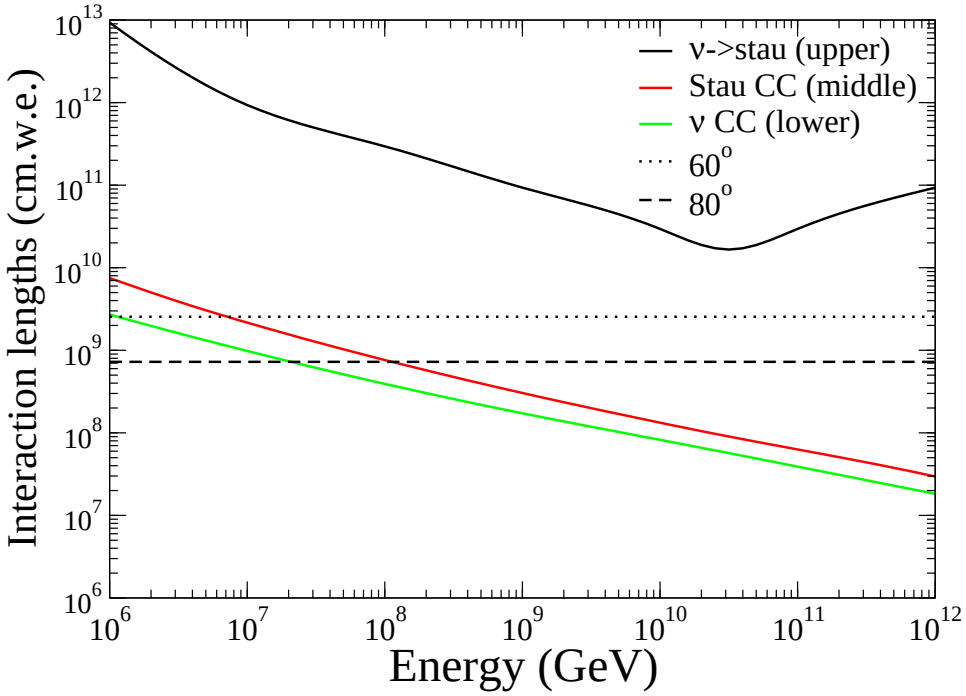


FIGURE 6.1. Interaction lengths for neutrinos and staus. The solid curves, from top to bottom, are the interaction lengths for neutrinos to produce staus, for stau charged current (CC) interactions with maximal weak interactions and for neutrino CC interactions. The dotted and dashed lines show the column depths for nadir angles of 60° and 80°.

for calculating the lepton or stau flux in the detector is outlined. We consider cosmogenic neutrinos, their propagation, stau production, and subsequent energy loss as it traverses the earth, for a region of parameter space where the staus do not decay over the distances required. We compare the resulting stau flux both for when there is no mixing between right-handed and left-handed stau and when there is maximal mixing. We consider muon-like signals (charged tracks) produced by staus and its associated background. We discuss the potential for eliminating the background by measuring the energy loss, which requires large volume detectors. Finally we discuss

the showers produced in the ice due to stau interactions and its background from neutrino-induced showers.

## 6.2 Muon Flux

Muons are produced by $\nu_\mu N$ charged-current interactions. Electromagnetic energy loss of muons passing through matter together with a survival probability that depends on lifetime and energy determines the muon flux. Electromagnetic energy loss is described by the average change in energy per unit column depth $X = \rho z$ (in terms of density $\rho$ and distance $z$) via

$$\frac{dE}{dX} = -(\alpha + \beta_\mu E) \ . \tag{6.1}$$

as discussed in Chapter 5. The radiative energy loss due to bremsstrahlung, pair production and photonuclear scattering, characterized by $\beta_\mu$, increases with energy from about $\simeq 4 \times 10^{-6}$ cm$^2$/g for $E_\mu \sim 10^3$ GeV to about $\simeq 5 - 6 \times 10^{-6}$ cm$^2$/g for $E_\mu \sim 10^9$ GeV [126]. Here we take $\beta_\mu \simeq 4 \times 10^{-6}$ cm$^2$/g, which will correspond to the maximum background for the stau charged-track signal due to muons. With $\alpha \simeq 2 \times 10^{-3}$ GeV cm$^2$/g [117], for the energies considered here, $dE/dX \simeq -\beta_\mu E$. Eq. (6.1) combined with effects of the finite muon lifetime on the survival probability $P_{\rm surv}$,

$$\frac{dP_{\rm surv}}{dX} = -\frac{P_{\rm surv}}{c\tau\rho E/m} \tag{6.2}$$

leads to

$$P_{\rm surv} = \exp\left[-\frac{m_\mu}{c\tau_\mu\beta_\mu\rho}\left(\frac{1}{E_\mu} - \frac{e^{-\beta_\mu(L-X)}}{E_\mu}\right)\right] \ . \tag{6.3}$$

The muon flux produced by incident muon neutrinos, for column depth $L$ is given

by

$$\begin{aligned} F_\mu(E_\mu, L) &\simeq \int_0^L dX \int dE_\nu e^{-X\sigma_{CC}(E_\nu)N_A} F_{\nu_\mu}(E_\nu, 0) \\ &\times N_A \sigma_{\nu\to\mu}(E_\nu)\delta(E_\mu - 0.8E_\nu e^{-\beta_\mu(L-X)}) \\ &\times \exp\left[-\frac{m_\mu}{c\tau_\mu\beta_\mu\rho}\left(\frac{1}{E_\mu} - \frac{e^{-\beta_\mu(L-X)}}{E_\mu}\right)\right], \end{aligned} \tag{6.4}$$

where the flux $F_\nu$ represents the $\nu_\mu + \bar{\nu}_\mu$ flux, $F_\mu$ is the sum of muon and antimuon fluxes, and we have made some simplifying approximations. We have approximated the neutrino-nucleon charged current differential cross section by

$$\frac{d\sigma_{\nu\to\mu}(E_\nu,\ E'_\mu)}{dE'_\mu} \simeq \sigma_{\nu\to\mu}(E_\nu)\delta(E'_\mu - 0.8E_\nu)$$

where $E'_\mu$ is the energy of the produced muon. This is the energy of the muon before it loses energy via electromagnetic interactions. We have also approximated the attenuation of the neutrino flux in transit through a column depth $X$ by the shadow factor

$$S \equiv \exp\Big(-\sigma^{\nu N}_{CC}(E_\nu)N_A X\Big)\ . \tag{6.5}$$

The muon fluxes, as a function of muon energy, are shown in Figs. 6.2 and 6.3 with dotted lines for two nadir angles, 80° and 88°. Also shown on these figures are the stau fluxes, to which we now turn.

## 6.3 Stau Flux

The stau flux depends on a number of inputs. We use the squark and slepton masses indicated in Section 4.2.1 yielding the $\nu \to \widetilde{\tau}$ interaction length shown in Fig. 6.1. A further choice of parameter is the mixing angle between weak isospin zero and weak isospin 1/2 scalars, the right-handed and left-handed staus, that yields the mass eigenstate of the NLSP stau. We consider two limiting cases: staus with no weak interactions, and staus with maximal weak interactions [13].

We start with the case of no weak interactions. In this case, the evaluation of the stau flux is similar to that of the muon flux. Ref. [5] shows that a reasonable parametrization of the energy loss parameter $\beta_{\tilde{\tau}}$ for staus is

$$\begin{aligned} \beta_{\tilde{\tau}} &= b_0 + b_1 \ln(E/E_0) \ , \\ b_0 &= 5 \times 10^{-9} \ \mathrm{cm}^2/\mathrm{g} \ , \\ b_1 &= 2.8 \times 10^{-10} \ \mathrm{cm}^2/\mathrm{g} \ , \\ E_0 &= 10^{10} \ \mathrm{GeV} \ . \end{aligned} \tag{6.6}$$

With the expression in Eq. (6.6), the stau survival probability and the relation between the initial stau energy and the final stau energy as a function of distance is modified from the constant $\beta$ case, namely [130]

$$\begin{aligned} E^i_{\tilde{\tau}}(E_{\tilde{\tau}}) &= E_0 \exp\Bigg[\Big[\frac{b_0}{b_1}(1 - e^{-b_1(L-X)}) \\ &+ \ln\frac{E_{\tilde{\tau}}}{E_0}\Big] e^{b_1(L-X)}\Bigg] \end{aligned} \tag{6.7}$$

$$\begin{aligned} P_{\mathrm{surv}}(E_{\tilde{\tau}}, E^i_{\tilde{\tau}}) &= \exp\Bigg(\frac{m_{\tilde{\tau}} b_1}{c\tau\rho b_0^2}\Bigg[\frac{1}{E_{\tilde{\tau}}}(1 + \ln(E_{\tilde{\tau}}/E_0) \\ &- \frac{1}{E^i_{\tilde{\tau}}}(1 + \ln(E^i_{\tilde{\tau}}/E_0)\Bigg]\Bigg) \\ &\times \exp\left[-\frac{m_{\tilde{\tau}}}{c\tau b_0 \rho}\left(\frac{1}{E_{\tilde{\tau}}} - \frac{1}{E^i_{\tilde{\tau}}}\right)\right] \end{aligned} \tag{6.8}$$

This leads to a stau flux of

$$\begin{aligned} F_{\tilde{\tau}}(E_{\tilde{\tau}}, L) &\simeq 2\int_0^L dX \int dE_\nu e^{-X\sigma_{CC}(E_\nu)N_A} F_\nu(E_\nu, 0) \\ &\times N_A \sigma_{\nu\to\tilde{\tau}}(E_\nu)\delta(E_{\tilde{\tau}} - \frac{1}{6}E_\nu \frac{E_{\tilde{\tau}}}{E^i_{\tilde{\tau}}(E_{\tilde{\tau}})}) \\ &\times P_{\mathrm{surv}}(E_{\tilde{\tau}}, E^i_{\tilde{\tau}}) \ . \end{aligned} \tag{6.9}$$

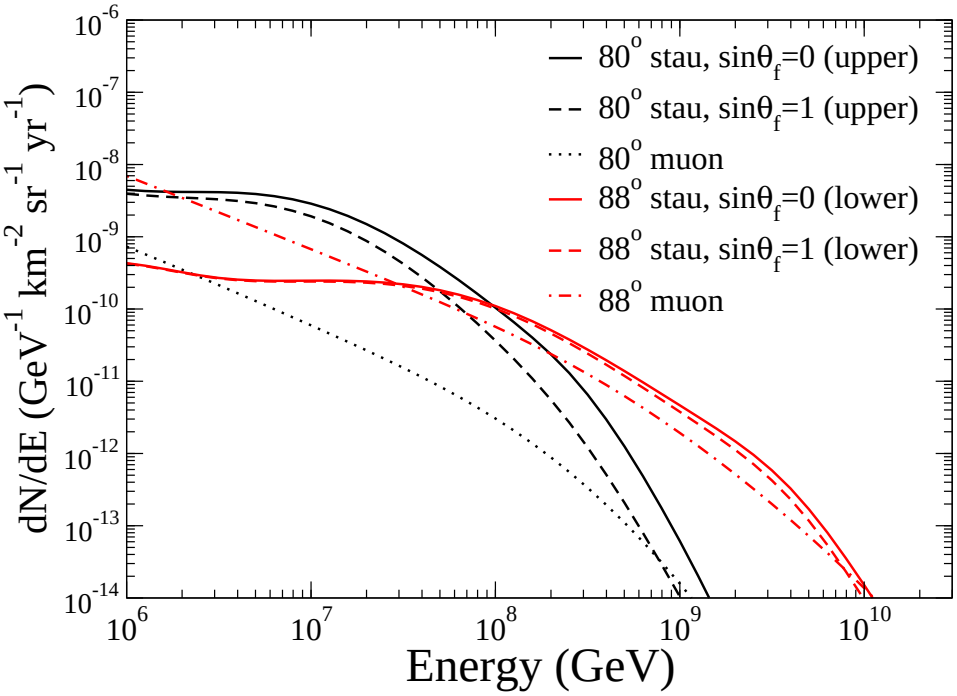


FIGURE 6.2. For fixed nadir angles of 80° and 88°, the stau flux assuming no weak interactions of the staus (solid lines) and assuming maximal weak interactions (dashed lines) produced by the ESS neutrino flux with standard evolution, evaluated using Eq. (6.9) and an input flux with including oscillations. The dotted line shows the neutrino induced muon flux at 80°.

The prefactor of 2 accounts for the fact that the staus appear in pairs, one from each of the chain of decays of the initial squark and slepton. All of the neutrino plus antineutrino flavors are included in $F_\nu(E_\nu, 0)$.

When weak interactions are included, there is an effect due to the attenuation of the staus themselves. The survival probability is modified and is given by

$$\begin{aligned} \frac{dP_{\rm surv}}{dX} &= -\frac{P_{\rm surv}}{\lambda_{\rm eff}} \\ \lambda_{\rm eff}^{-1} &= (c\tau\rho E/m_{\tilde\tau})^{-1} + N_A\sigma^{CC}(\tilde\tau N) \end{aligned} \tag{6.10}$$

The solution of the combined equations Eqs. (6.10) and (6.1) is done numerically.

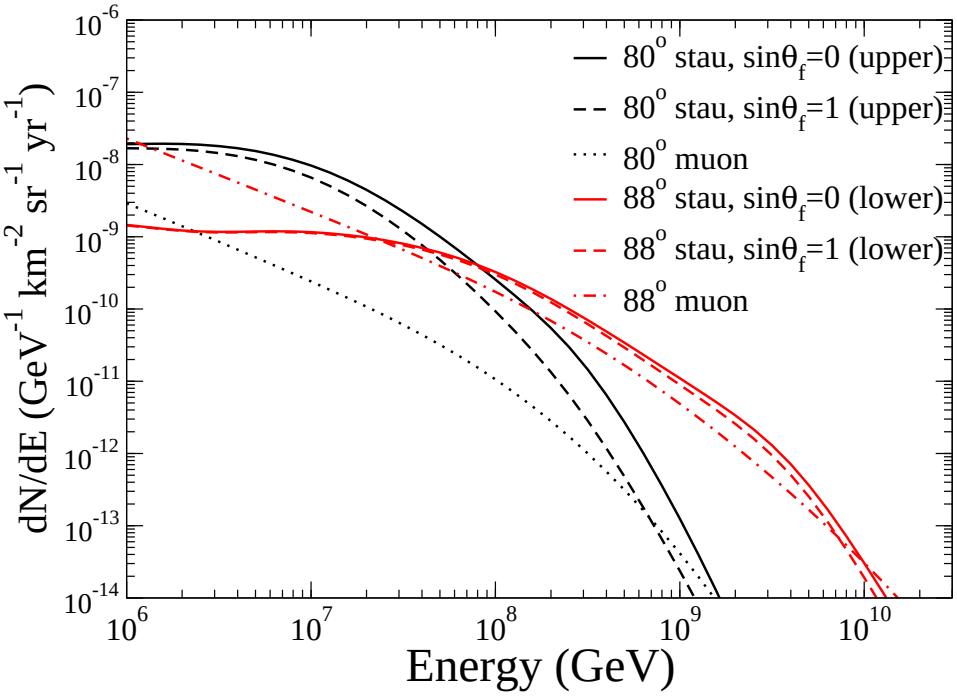


FIGURE 6.3. For fixed nadir angles of 80° and 88°, the stau flux assuming no weak interactions of the staus (solid lines) and maximal weak interactions (dashed lines) produced by the ESS neutrino flux with strong evolution, evaluated using Eq. (6.9) and an input neutrino flux with oscillations. The dotted line shows the neutrino induced muon flux at 80°.

The resulting stau fluxes, for fixed nadir angles of 80°, 85° and 88° are shown as a function of stau energy in Fig. 6.2 for the ESS standard evolution flux, and in Fig. 6.3 for the strong evolution. In these figures, the solid lines are with minimal weak interactions, while the dashed lines are for maximal weak interactions.

## 6.4 Stau signals

### 6.4.1 Stau Charged Tracks

The fluxes of staus and muons depend on the initial neutrino fluxes, the production cross sections, and the energy loss parameter $\beta$. For the stau signal, the initial neutrino flux includes all neutrino flavors while for muons, only the oscillated $\nu_\mu + \bar{\nu}_\mu$ flux contributes. The neutrino energy required to produce a stau or a muon of comparable initial energy along the trajectory through the earth is about 5 times higher for the stau because the mean energy of the resulting stau is approximately 1/6 of the incident neutrino energy, in contrast to the muon case where $E'_\mu \sim 0.8E_\nu$. This means we are probing higher energy neutrinos for staus than for muons to produce a quasi-stable particle of a given energy. On the other hand, the muons lose more energy in transit from the production point to the detection point.

The production cross section for staus is approximately three orders of magnitude smaller than the muon production cross section. Once the staus are produced, they lose very little energy as they traverse the earth while the muon energy loss is of the order $10^2 - 10^3$ times greater. The stau range can be as high as $10^4$ km.w.e. for vanishing charged-current interactions or suppressed to about $10^3$ km.w.e. for maximal charged-current interactions, both higher than the muon range. The neutrino attenuation will also have a large effect on the signals. This attenuation acts to deplete more muons than staus since the muons must be created very near the detector to be seen, whereas the staus can be produced farther away.

These competing effects account for the large stau/muon ratio for specific angles and particle energies. In Fig. 6.4, we show the ratio of the stau flux to the muon flux for the angles 80°, 85°, and 88°, as a function of energy, for standard ESS evolution. The solid lines show the ratio in the scenario where stau weak interactions do not occur. The effect of including maximal charged-current interactions of the staus can be seen by the suppression in the ratio, shown with the dashed lines. We note that

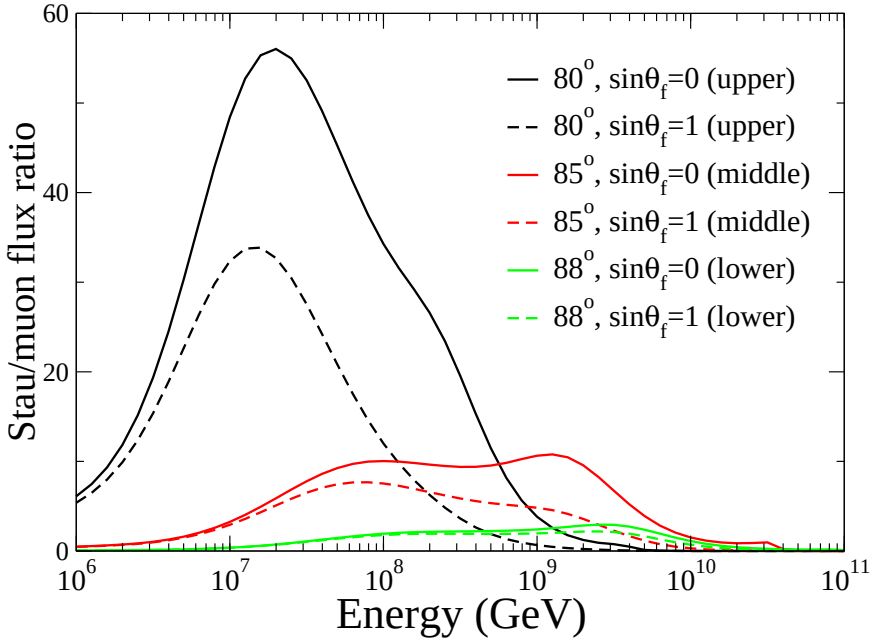


FIGURE 6.4. For fixed nadir angles of 80°, 85° and 88°, the ratio of the stau flux assuming no weak interactions of the staus (solid lines) and maximal weak interactions (dashed lines) to the muon flux produced by the ESS neutrino flux with standard evolution, including oscillations.

the suppression in the ratio begins to take effect between $10^6$ and $10^7$ GeV, where the stau range begins to be affected by stau charged-current interactions [13]. In Fig. 6.4, the largest ratio occurs for the nadir angle of 80° which represents the largest path length through the earth of the trajectories shown. As the nadir angle is decreased, there is an enhancement in the ratio until it reaches a maximum value and then it drops off when the neutrino attenuation begins to be the dominant effect for the signal. At lower energies, $E_{\tilde{\tau}} \sim 2 \times 10^6$ GeV, the maximum ratio is 125 (at 70°) when stau maximum weak interactions are included and it is 280 when there are no stau weak interactions. Furthermore, our signal to background ratios increase by about 50% (for energy around $10^7$ GeV) if we incorporate energy dependent muon energy

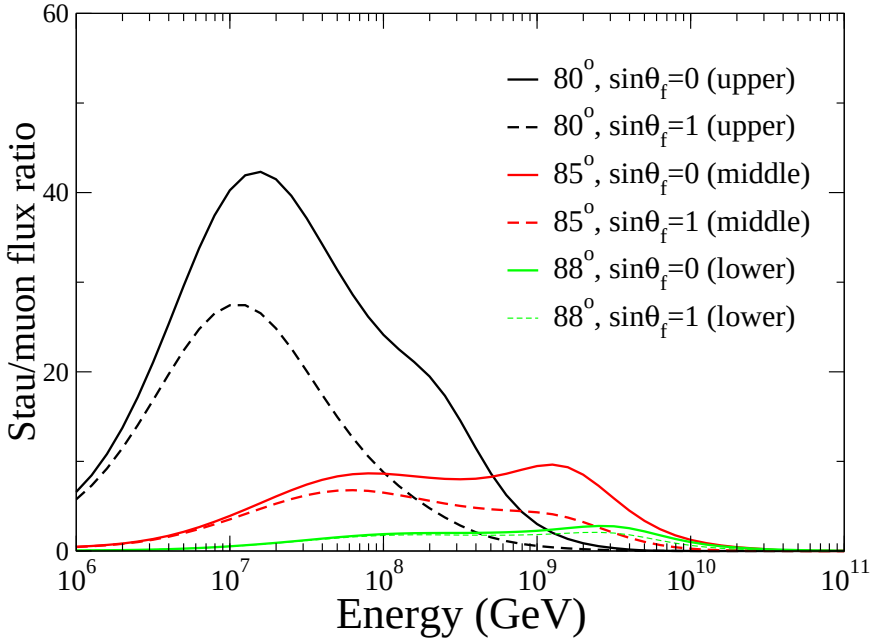


FIGURE 6.5. For fixed fixed nadir angles of 80°, 85° and 88°, the ratio of the stau flux assuming no weak interactions of the staus (solid lines) and maximal weak interactions (dashed lines) to the muon flux produced by the ESS neutrino flux with strong evolution, including neutrino oscillations.

loss, by increasing $\beta_\mu$ value to $\beta_\mu \simeq 6 \times 10^{-6}$ cm$^2$/g.

Fig. 6.5 shows the same effects for strong ESS evolution where the ratio is somewhat reduced. We show in Figs. 6.6 and 6.7 the ratio for stau/muon fluxes as a function of angle for the two fixed final particle energies $10^7$ and $10^8$ GeV, for ESS standard and strong evolutions. Again, we see the same enhancement of stau/muon ratio shifted to the lower angles shown. The strong ESS evolution shows the same behavior as standard evolution, again with a suppressed ratio.

Figures 6.4-6.7 show a significant enhancement of the stau flux relative to the muon flux for various energies and angles. Extracting the stau signal, however, is quite difficult. At issue is the fact that apart from stau decays and charged current

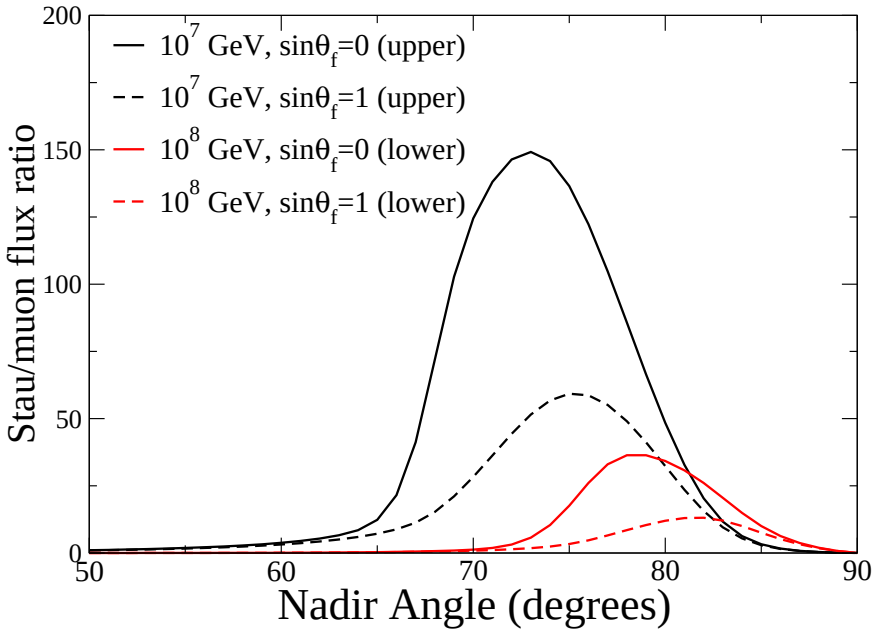


FIGURE 6.6. For fixed energies of $10^7$ and $10^8$ GeV, the ratio of the stau flux assuming no weak interactions of the staus (solid lines) and maximal weak interactions (dashed lines) to the muon flux produced by the ESS neutrino flux with standard evolution, including oscillations.

interactions, the stau moves through matter in a way similar to a lower energy muon: the stau signal is muon-like.

In terms of electromagnetic energy loss, one of the issues is that the average of the energy loss per unit distance at high energy scales with $\beta E$. The electromagnetic energy loss parameter $\beta$ for pair production and photonuclear contributions to the energy loss scales as the inverse mass of the charged particle. The bremsstrahlung process, important for muon energy loss, is negligible for stau energy loss since it scales with the inverse mass squared.

An important element of the energy loss is the electron positron pair production cross section. This cross section is important at low values of the inelasticity

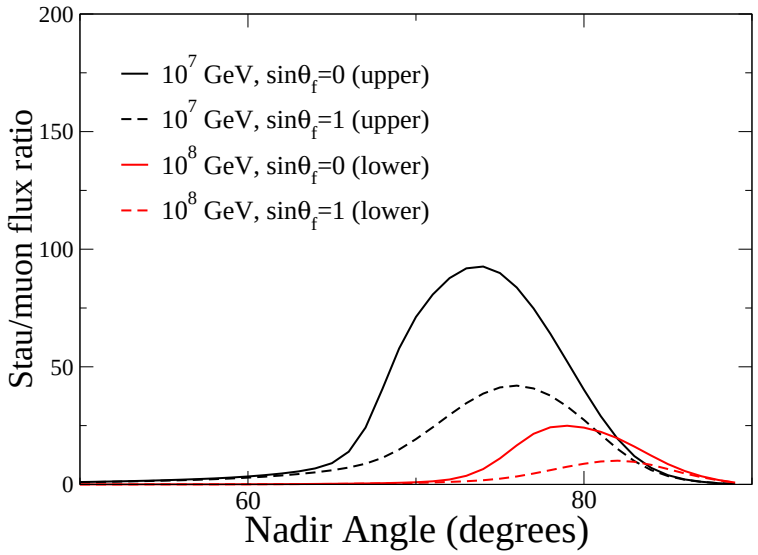


FIGURE 6.7. For fixed energies of $10^7$ and $10^8$ GeV, the ratio of the stau flux assuming no weak interactions of the staus (solid lines) and maximal weak interactions (dashed lines) to the muon flux produced by the ESS neutrino flux with strong evolution, including neutrino oscillations.

parameter $v$ where

$$v = \frac{E - E'}{E} \ , \tag{6.11}$$

the ratio of the change in muon or stau energy to the initial energy. In Fig. 6.8 we show the differential cross section $v d\sigma/dv$ scaled by $N_A/A$ for muons scattering in iron [121, 131]. For ease of viewing the small $v$ region, we plot the differential cross section versus $1/v$. Because the photonuclear process includes inelastic scattering corrections [126, 132], the differential cross section depends on the incident muon energy. Pair production dominates for $1/v$ greater than $\sim 10$, that is to say for muon energy losses of less than $\sim 10\%$ of the initial muon energy.

The corresponding differential cross section for staus is shown in Fig. 6.9. This figure shows that the dominant process for energy loss of staus is pair production

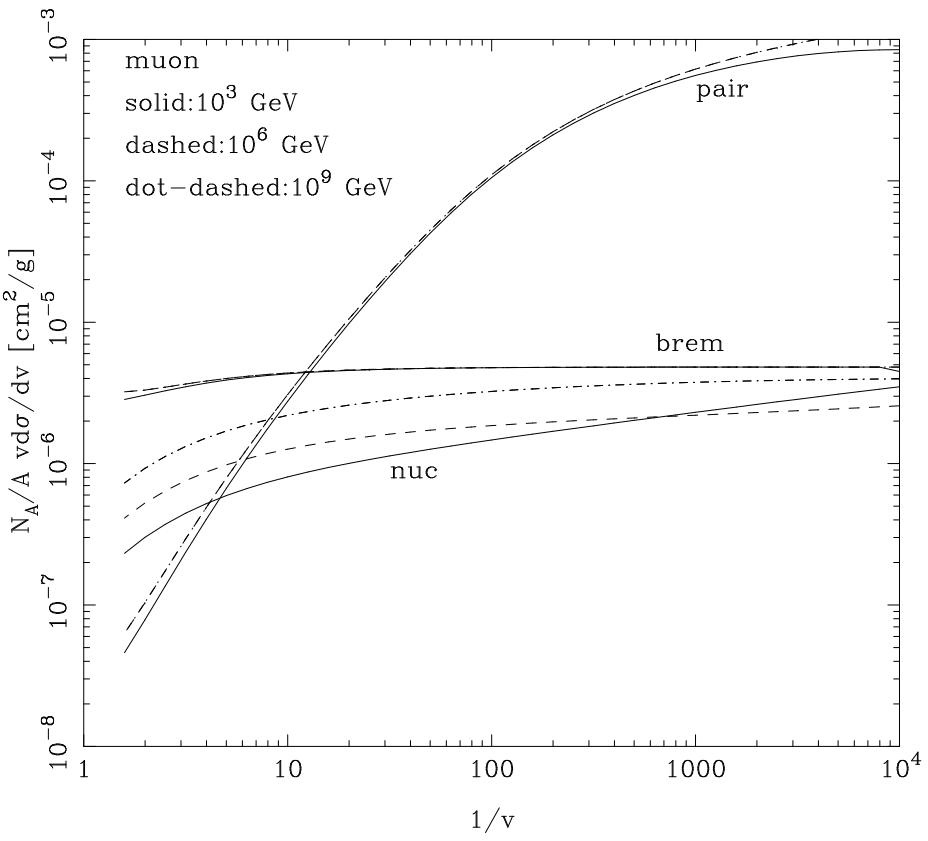


FIGURE 6.8. The inelasticity weighted differential cross section for muons for three muon energies: $10^3$ GeV (solid lines), $10^6$ GeV (dashed lines) and $10^9$ GeV (dot-dashed lines) for pair production, bremsstrahlung and photonuclear energy loss processes.

only for energy losses of less than $v \sim 10^{-4}$. Similar results are obtained for ice.

Figs. 6.8 and 6.9 can be interpreted in terms of the average energy loss $\langle dE/dX \rangle$. For a stau of energy $E_{\tilde{\tau}}$, the average energy loss per unit distance is of order of that of a muon with energy $E_\mu \sim 10^{-3} E_{\tilde{\tau}} \sim m_\mu/m_{\tilde{\tau}} \cdot E_{\tilde{\tau}}$. If the average energy loss per unit distance is the only observable quantity, the large stau to muon ratios are unobservable because one must compare the high energy stau flux with the lower energy, but significantly larger, muon flux. Quantitatively, this is shown in Fig. 6.10. Here we take the ratio of the stau flux at energy $E_{\tilde{\tau}} = m_{\tilde{\tau}}/m_\mu \cdot E_\mu$ to the muon flux evaluated at $E_\mu$. We note that the ratio is peaked at the same angle as in Fig. 6.6,

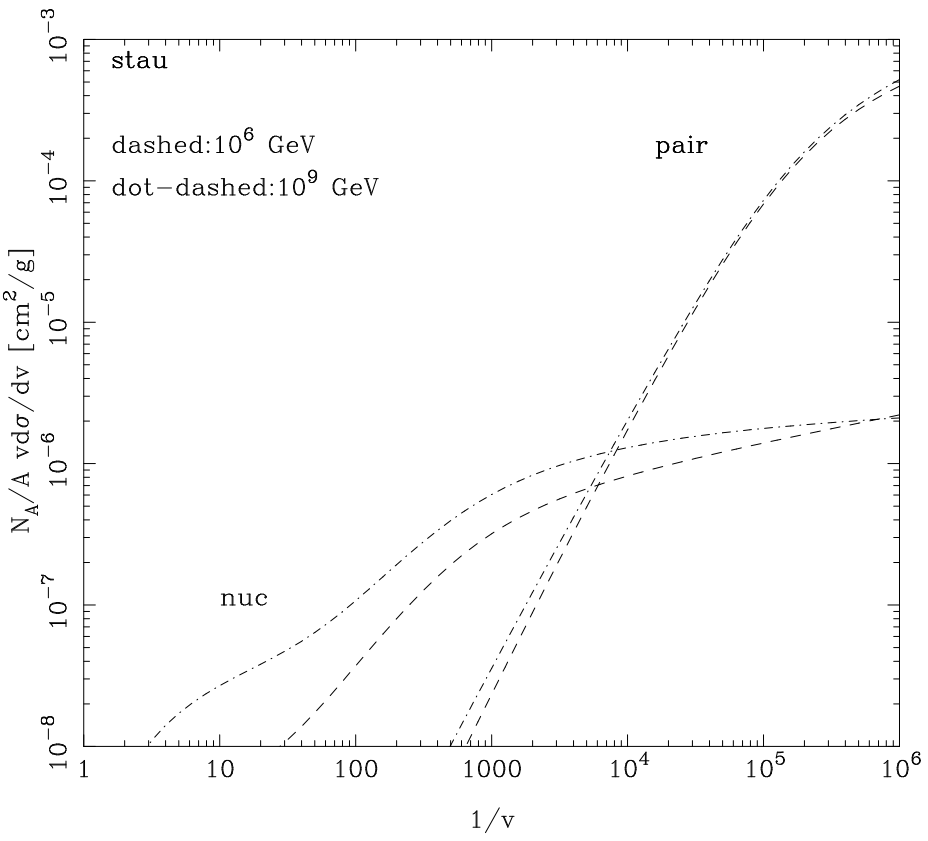


FIGURE 6.9. The inelasticity weighted differential cross section for staus for two energies: $10^6$ GeV (dashed lines) and $10^9$ GeV (dot-dashed lines) for pair production and photonuclear energy loss processes. Bremsstrahlung energy losses are negligible for staus.

but the ratio is much smaller. This is because $\langle dE/dX \rangle$ matches, for example, muons with energies of $10^7$ GeV to staus with energies more than two orders of magnitude higher, where the stau flux is low.

The $v$-dependence of the cross sections in Figs. 6.8 and 6.9 may open a window for differentiating muons and staus in the future. Fig. 6.9 shows a marked difference between muons and staus for large $v$ (small $1/v$). An energy deposit of 10% of the initial stau energy of $E_{\tilde{\tau}} = 10^8$ GeV is observed in a stau signal interaction, with very little in the way of comparable energy losses nearby since the large $v$ cross section is so low. With such a large energy loss (say, $\Delta E = 0.1 E_{\tilde{\tau}}$), there would be no confusing

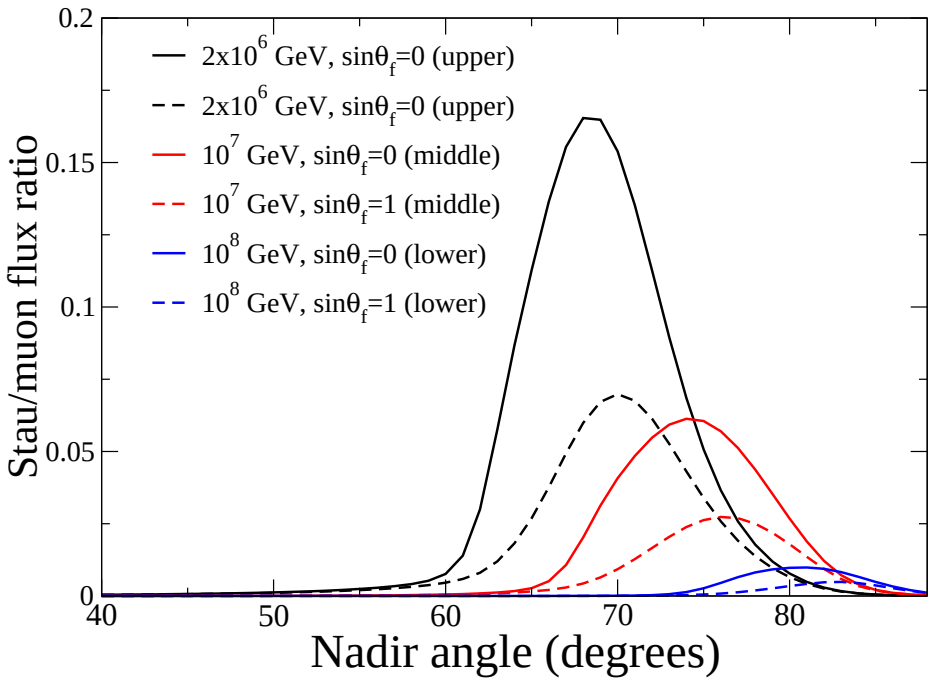


FIGURE 6.10. The ratio of stau flux at energy rescaled by $m_{\tilde{\tau}}/m_{\mu}$ as a function of the nadir angle for muon energy of $10^7$ GeV and $10^8$ GeV including stau maximal weak interactions (dashed lines) and no weak interactions (solid lines).

the stau with muon with an energy of $E_{\mu} = m_{\mu}/m_{\tilde{\tau}} \cdot E_{\tilde{\tau}}$ since $E_{\mu} \ll \Delta E$. On the other hand, a similar energy deposit could come for a muon with the same high energy, but the profile of the track would be significantly different, with more large energy losses along the muon track where the multiple pair production energy losses contribute. Essential here is the large ratio of stau to muon masses. The effect is more difficult to observe when the masses are closer, e.g., for taus compared to muons [133].

In Figs. 6.11 and 6.12 we show the average number of interactions per unit distance of ice rather than the energy loss per unit distance. This is evaluated using

$$M = \frac{X\rho N_A}{A} \int_{v_{\min}}^{1} dv \, \frac{d\sigma}{dv} \, , \tag{6.12}$$

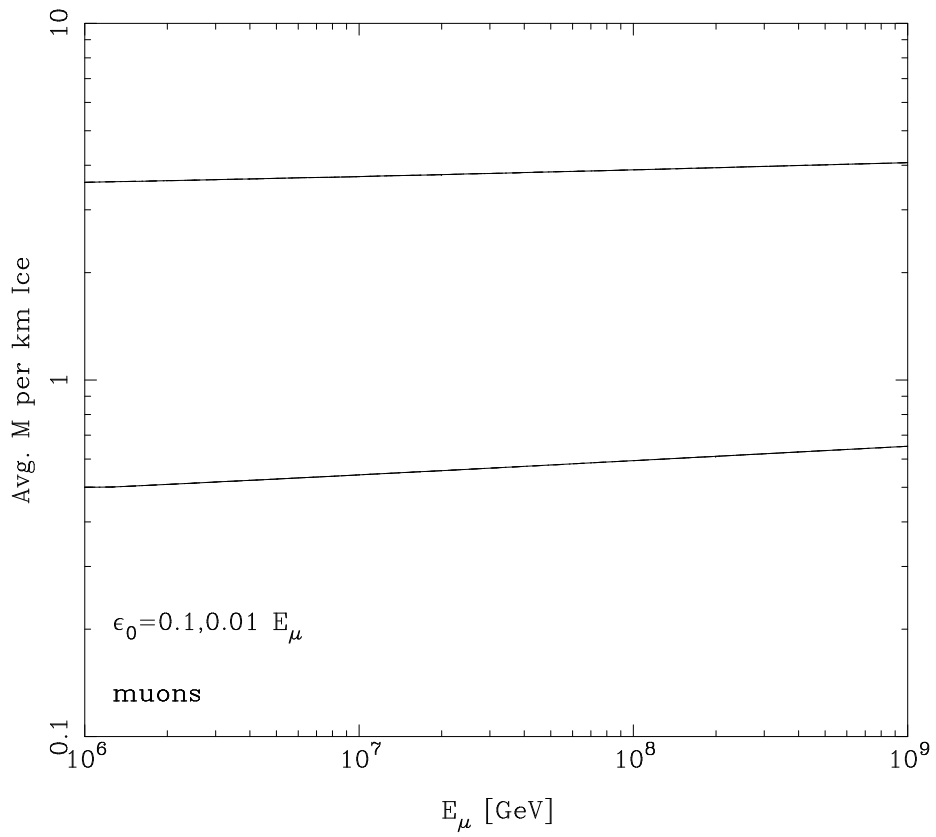


FIGURE 6.11. The average number of interactions per km of ice for muons. The upper line is for $v > 0.01$, and the lower line is for $v > 0.1$.

for density $\rho$ and column depth $X$. Here we have taken $v_{\min} = \epsilon_0/E = 0.1, 0.01$ for muons and staus. The lower line on Figs. 6.11 and 6.12 are for $v_{\min} = 0.1$ and the upper lines are for $v_{\min} = 0.01$. A muon which can deposit 10% of its initial energy of $10^8$ GeV proceeds to have a significantly larger number of subsequent interactions in which 10% of its energy is deposited, as compared to the stau of the same energy. The scale of the average number of interactions is such that one would need an observational coverage of a few tens of kilometer distance scales to see the distinction between muons and staus.

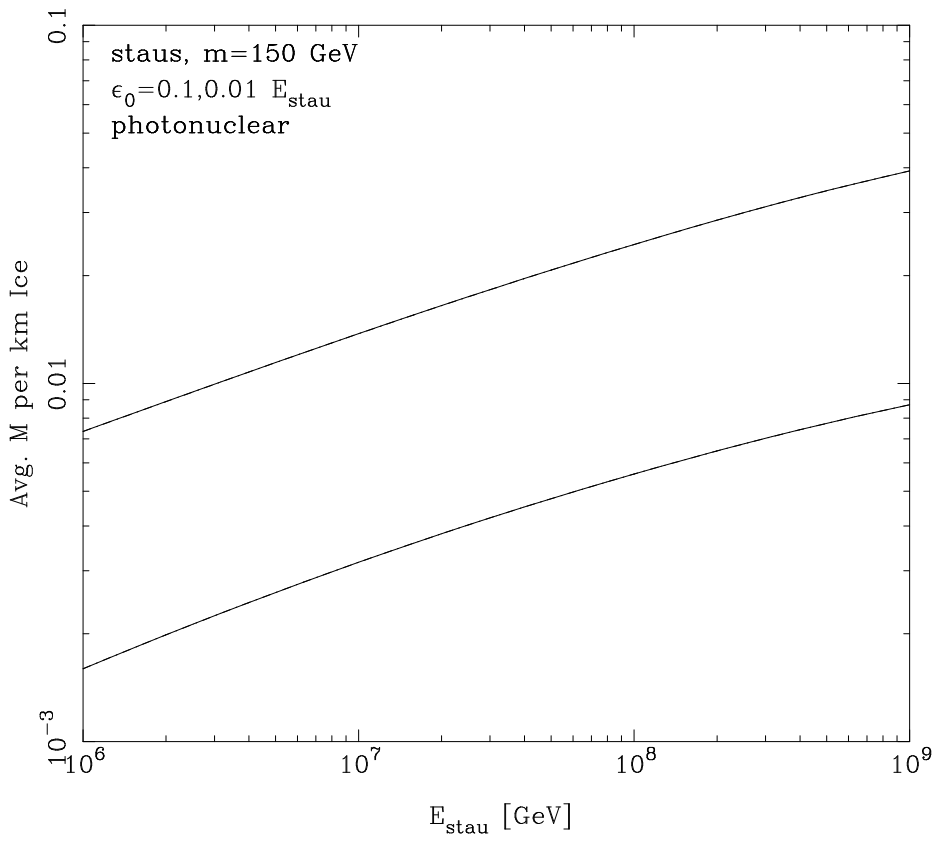


FIGURE 6.12. The average number of interactions per km of ice for staus with $m_{\tilde{\tau}} = 150$ GeV. The upper line is for $v > 0.01$, and the lower line is for $v > 0.1$.

### 6.4.2 Stau Showers in Ice

Staus reaching the detector could interact in principle via weak interactions producing showers. Weak interactions of staus reduce its range [13], but provide an additional opportunity for its detection via interactions in ice which can provide a signal for detectors such as ANITA [2,98] and ARIANNA [99]. We discuss here showers produced by staus and the background due to neutrino induced showers.

We have evaluated stau and neutrino showers for different nadir angles for energies above $10^6$ GeV. In the shower production, we assume maximal mixing for the charged-current interactions for staus. The stau showers for a given incident angle are determined by Eq. (6.9), modified to include the probability to produce showers

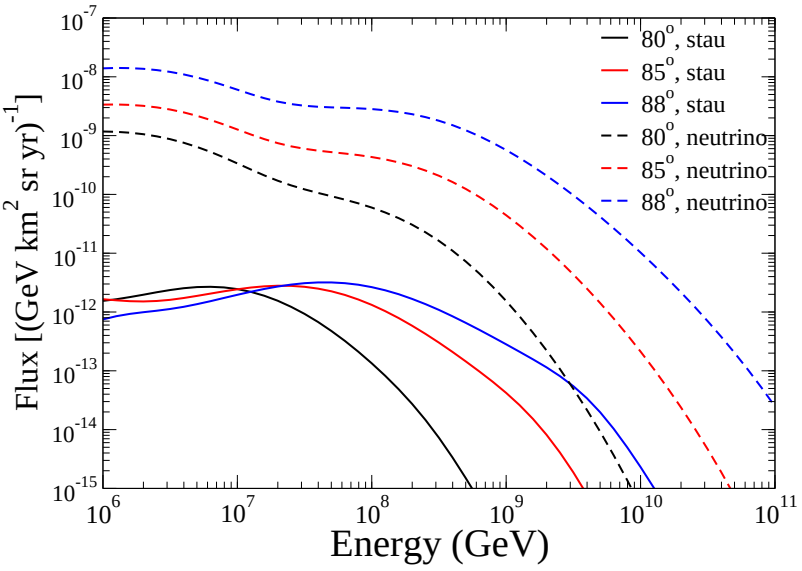


FIGURE 6.13. The shower flux for the incident angles 80° (lower curves), 85° (middle curves), and 88° (upper curves) from staus (solid lines) and neutrinos (dashed lines).

in the ice,

$$\begin{aligned} F_{\tilde{\tau},\mathrm{shr}}(E_{\mathrm{shr}},L) &= \int_0^{z_{ice}} F_{\tilde{\tau}}(E_{\mathrm{shr}},L-z')e^{-z'/\mathcal{L}^{\tilde{\tau}}_{CC}}\frac{dz'}{\mathcal{L}^{\tilde{\tau}}_{CC}} \\ &\simeq F_{\tilde{\tau}}(E_{\mathrm{shr}},L)(1-e^{-z_{ice}/\mathcal{L}^{\tilde{\tau}}_{CC}}) \ . \end{aligned}$$

The stau interaction length due to charged current interactions is $\mathcal{L}^{\tilde{\tau}}_{CC}$. We use the interaction length for maximal weak interactions shown in Fig. 6.1. The pathlength through the ice, $z_{ice}$, for $\theta < 88.56^o$ is given by

$$z_{ice} = R_E\cos\theta - \sqrt{R_E^2\cos^2\theta - 2R_E t + t^2}, \tag{6.13}$$

where $R_E$ represents the radius of the earth and $t$ the average ice thickness, taken to be 2 km. For comparison, showers due to neutrinos are found from the equation,

$$F_{\nu,\mathrm{shr}}(E_{\mathrm{shr}},L) \simeq F_{\nu}(E_{\mathrm{shr}},L)(1-e^{-z_{ice}/\mathcal{L}^{\nu}_{CC}}) \ . \tag{6.14}$$

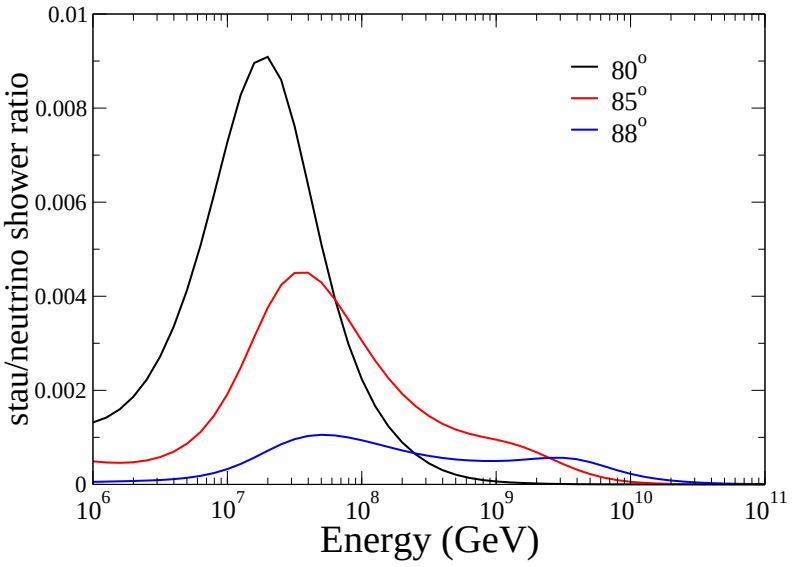


FIGURE 6.14. The ratio of stau to neutrino induced shower fluxes for the incident angles 80°, 85°, and 88°, represented by curves with the highest, intermediate and lowest peaks, respectively.

We compare the results for the showers due to staus and neutrinos for three nadir angles: 80°, 85°, and 88° in Figs. 6.13 and 6.14. All of the results in this section were obtained using the standard evolution cosmogenic flux.

In Fig. 6.13, the showers due to neutrinos are of the order $10^3 - 10^4$ larger than staus at an energy of $10^6$ GeV. The input neutrino flux for the stau signal will be at a higher energy than for the direct neutrino production of showers. The neutrino flux falls off as a function of energy so the ratio of stau to neutrino showers will be suppressed in part due to this effect. In addition, the stau flux is suppressed due to the small stau production cross section. The probability of producing showers in the detector is roughly the same for neutrinos and for staus with maximal charged-current interactions, so the inclusion of the showers is not sufficient to make up for the suppression.

The shape of the stau induced shower flux changes relative to the neutrino induced shower flux, so between $10^7 - 10^8$ GeV there is a peak in the ratio of stau to neutrino induced showers. This effect is seen in Fig. 6.14, where the peak in the ratio of stau/neutrino showers appears, but as indicated, the ratio is small. It is about 0.009 for 80°.

Fig. 6.15 shows the stau/neutrino ratio for the two fixed shower energies, $10^7$ and $10^8$ GeV, as a function of nadir angle. We can see that the ratio is the largest for $10^7$ GeV at about 78°. The integrated flux taking into account the contribution due to all incident angles is given in Fig. 6.16. The maximum stau/neutrino ratio occurs for an energy of $2.5 \times 10^7$ GeV and corresponds to a stau signal only 0.33 % of the neutrino signal.

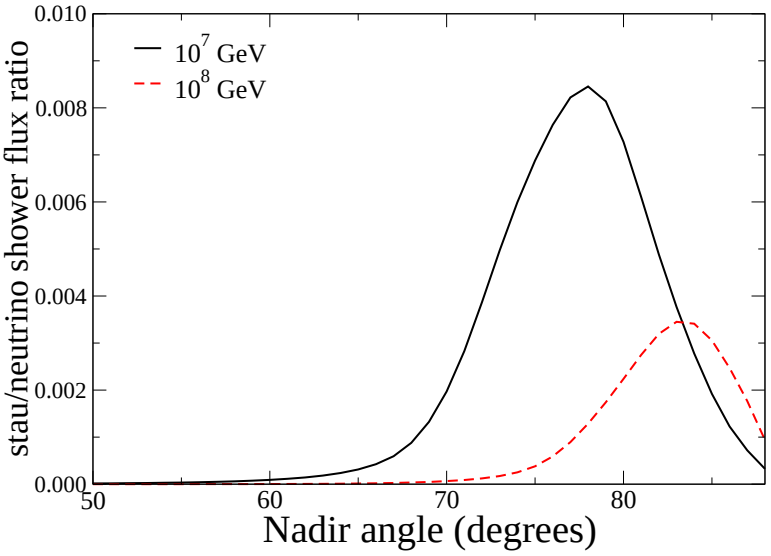


FIGURE 6.15. The ratio of the fluxes of showers due to stau and neutrino fluxes for the energies $10^7$ and $10^8$ GeV as a function of incident angle.

Whereas muon-like signals from staus can be large compared to muon signals from neutrinos because of the long lifetime of the stau, we find that the shower signal to

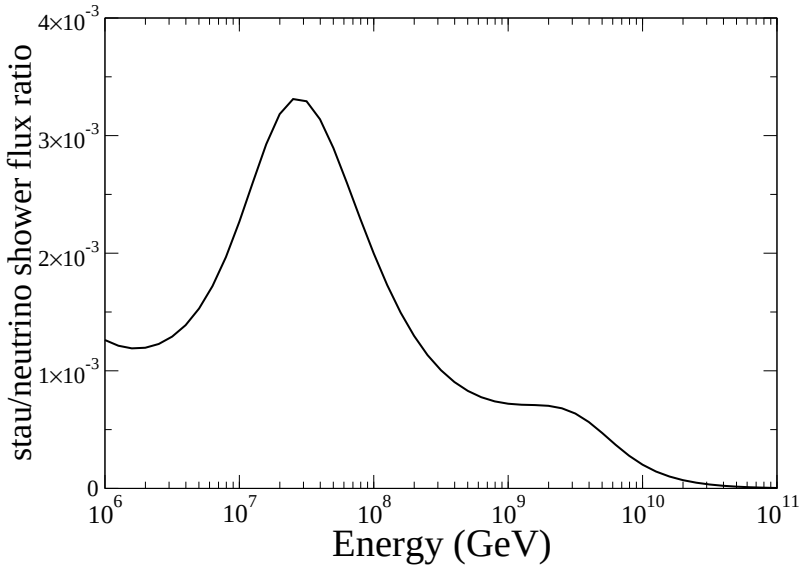


FIGURE 6.16. The ratio of stau induced to neutrino induced shower fluxes, integrated over all incident angles.

background ratio is quite small for all angles. This is due to combination of the small production cross section for stau and the energy effects due to the chain of production and the energy loss of the stau. Stau attenuation as it traverses the earth is roughly of the same size as neutrino attenuation, as are the probabilities for staus or neutrinos to produce showers.

## 6.5 Comparison with Results using WB Initial Neutrino Flux

Previous studies on the expected stau signal in neutrino telescopes such as IceCube have utilized an incident Waxman-Bahcall neutrino flux as given in Eq. (3.2) [3, 4, 9]. The present work focuses on an incident ESS flux as it describes a guaranteed flux and it has a different energy dependence than the $E^{-2}$ dependence of WB. The ESS flux is larger than WB for $E \sim 10^8 - 10^9$ GeV, or the energy regime where ANITA

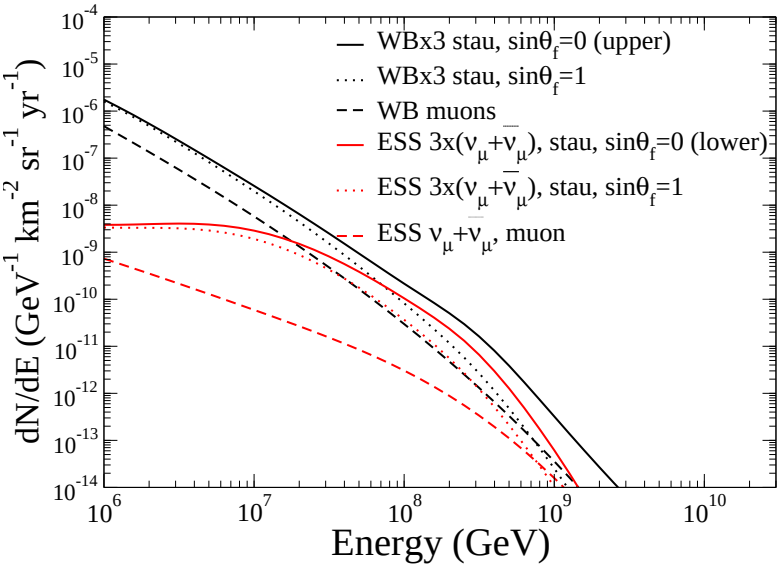


FIGURE 6.17. Stau flux at 80° for both maximal ($\sin\theta_f = 1$) and minimal ($\sin\theta_f = 0$) CC interactions and muon flux using both a WB and an ESS incident neutrino flux for comparison.

and ARIANNA have the greatest sensitivity and where CC interactions will have the greatest effect. The expected stau and muon fluxes for a nadir angle of 80° with an incident WB neutrino flux are compared to the results obtained with an incident ESS flux in Fig. 6.17. In order to compare the two results we show the results using an incident $\nu_\mu + \bar{\nu}_\mu$ neutrino flux only. We show the WB and ESS $\nu_\mu + \bar{\nu}_\mu$ fluxes multiplied by a factor of three to represent the total neutrino flux for the staus and just the $\nu_\mu + \bar{\nu}_\mu$ flux for the muons. Fig. 6.17 shows that for a nadir angle of 80° the results for an incident WB neutrino flux are consistently larger than for the ESS flux due to the different energy dependencies of the two fluxes. To determine the calculated stau flux the neutrino flux is sampled from a higher energy. In the case of WB this always corresponds to an energy region where the flux falls off as $E^{-2}$ while for ESS the energy dependence for regions of higher energy follow a power law with

a higher spectral index, accounting for the result.

Fig. 6.18 details the expected neutrino, muon, and stau fluxes integrated over solid angle for an incident WB neutrino flux for comparison.

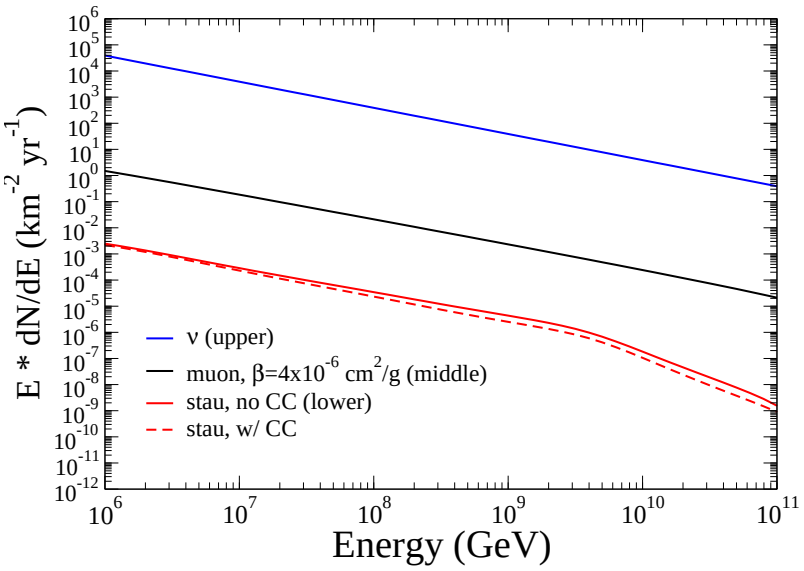


FIGURE 6.18. Total neutrino, muon, and stau fluxes (with and without CC interactions) integrated over all incident angles for an incident WB flux.

Fig. 6.18 shows the expected stau flux without proper rescaling of the stau energy as discussed in the previous section so that it can be compared to the stau flux that has been determined in the previous work. The results for the expected muon flux at these energies are about 20% larger than the flux given by Ahlers et al. in [4] between the energies of $10^5 - 10^6$ GeV. The muon flux presented is approximately an order of magnitude smaller than that in Ref. [3]. The expected flux integrated over all angles for an incident ESS neutrino flux is presented for comparison in Fig. 6.19.

It can be seen by comparing these results that the integrated neutrino flux from an incident WB flux is larger than the ESS flux for energies less than $\sim 10^9$ GeV at which point the ESS flux becomes slightly larger. Both the muon and stau fluxes

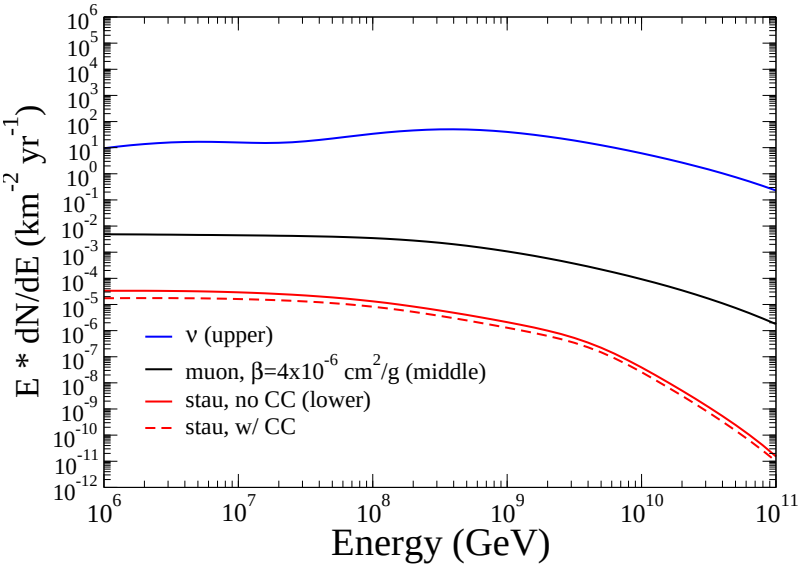


FIGURE 6.19. Total neutrino, muon, and stau fluxes (with and without CC interactions) integrated over all incident angles for an input ESS neutrino flux.

from WB neutrinos are consistently slightly larger than those from ESS neutrinos. This difference can be accounted for again by the different energy dependencies of the WB and ESS fluxes.

# Chapter 7
# Conclusion

The present work describes signals of staus produced in interactions of cosmogenic neutrinos. We have considered two types of signals, muon-like charged tracks and showers. We have focused on low scale supersymmetric models that have stau as NLSP, which decays into the lightest SUSY particle, the gravitino. For a sufficiently large scale of supersymmetry breaking, the stau has a very long lifetime and will not decay in the Earth.

Our focus has been on cosmogenic neutrino fluxes and their associated stau production in the Earth. For comparison we also include a discussion of a WB incident neutrino flux, noting the different results for the two due to their different energy dependencies. The new Auger data (as discussed in Section 3.3.3) allows for a better determination of the composition of cosmic rays as determined in Ref. [85], ultimately leading to the possibility of a substantial reduction in the corresponding neutrino flux. The reduction in the incoming neutrino flux would correspond directly to a reduction in the eventual stau flux at the detector.

Energy losses, both through electromagnetic and weak interactions, are important in evaluating stau signals. The energy loss of staus, however, is relatively small in comparison with muons. Thus, for some nadir angles, the stau flux is much larger than the muon flux produced in neutrino charged-current interactions.

The enhancement of the stau flux is larger from an input cosmogenic neutrino flux than for the Waxman-Bahcall neutrino flux [15]. This is because the cosmogenic neutrino flux is peaked at energies of about $10^8$ GeV, while the WB flux is characterized by a steep power law with index of two. The large ratio of staus to muons from cosmogenic neutrinos is encouraging for experimental detection, but in order to

see this signal one needs to be able to distinguish between staus and muons. Using the average energy loss per unit distance is not a good way to distinguish staus and muons, since the scaling of the energy loss parameter $\beta$ has the effect of making a high-energy stau look like a lower energy muon. We have proposed a way to distinguish between stau and muon tracks by measuring the energy loss of muons via their interactions in the ice, and to use this method to reduce the background.

We also considered showers produced by staus interacting in the ice via charged-current interactions. The backgrounds for this signal are showers induced directly by neutrinos that reach the detector and interact inside the detector via charged-current or neutral-current interactions. The only way that staus would produce showers in the ice is if there is a weak mixing, but this process also contributes to reducing stau range. These effects combine with the small stau production probability to give fluxes of attenuated staus that are several orders of magnitude less than attenuated neutrino fluxes. This small stau to neutrino ratio translates directly to shower rates.

In addition to weak interactions, another possibility for shower production would be stau decays in the detector. For the parameter space considered here, with long-lived staus, the signal from decays is suppressed relative to their weak interactions.

In summary, stau signals at high energies are best identified by muon-like tracks. The most important detection issue is distinguishing between staus and muons, which may be possible by looking at the incremental electromagnetic energy loss as the charged particle moves through the detection volume. With very large volumes, there is a potential for detection of staus with future large neutrino telescopes. To track and identify the different particle trajectories, an observational coverage of tens of kilometers is necessary. The future extensions to IceCube previously presented in Section 3.5 IceCube-plus and Hypercube project a factor of two increase in the detector volume over IceCube [92]. Hypercube will have twice as many strings as IceCube, which will ultimately allow for a factor of five increase for the trajectory for horizontal muons and staus. This increased distance could allow for the possibility

of distinguishing between the tracks of horizontal staus and muons. In conclusion, between existing and future experiments the techniques presented here give an interesting possibility for determining parameters of a supersymmetric model. Even with the advent of the LHC era, neutrino telescopes still offer a promising counterpart to understanding physics beyond the Standard Model.

# References


[1] M. Ackermann, (2007), arXiv:0711.3022.

[2] S. W. Barwick *et al.*, Phys. Rev. Lett. **96**, 171101 (2006).

[3] I. F. M. Albuquerque, G. Burdman, and Z. Chacko, Phys. Rev. **D75**, 035006 (2007).

[4] M. Ahlers, J. Kersten, and A. Ringwald, JCAP **0607**, 005 (2006).

[5] M. H. Reno, I. Sarcevic, and S. Su, Astropart. Phys. **24**, 107 (2005).

[6] B. Aharmim *et al.*, Phys. Rev. **C72**, 055502 (2005).

[7] Y. Ashie *et al.*, Phys. Rev. Lett. **93**, 101801 (2004).

[8] C. Bemporad, Nucl. Phys. Proc. Suppl. **77**, 159 (1999).

[9] I. Albuquerque, G. Burdman, and Z. Chacko, Phys. Rev. Lett. **92**, 221802 (2004).

[10] X.-J. Bi, J.-X. Wang, C. Zhang, and X.-m. Zhang, Phys. Rev. **D70**, 123512 (2004).

[11] T. Han and D. Hooper, New J. Phys. **6**, 150 (2004).

[12] L. Anchordoqui and F. Halzen, Annals Phys. **321**, 2660 (2006).

[13] Y. Huang, M. H. Reno, I. Sarcevic, and J. Uscinski, Phys. Rev. **D74**, 115009 (2006).

[14] M. Ahlers, J. I. Illana, M. Masip, and D. Meloni, JCAP **0708**, 008 (2007).

[15] M. H. Reno, I. Sarcevic, and J. Uscinski, Phys. Rev. **D76**, 125030 (2007).

[16] S. Ando, J. F. Beacom, S. Profumo, and D. Rainwater, JCAP **0804**, 029 (2007).

[17] J. I. Illana, M. Ahlers, M. Masip, and D. Meloni, Acta Phys. Polon. **B38**, 3357 (2007).

[18] C. Zhang and Y. Ma, Nucl. Phys. Proc. Suppl. **175-176**, 257 (2008).

[19] E. Waxman and J. N. Bahcall, Phys. Rev. **D59**, 023002 (1999).

[20] R. Engel, D. Seckel, and T. Stanev, Phys. Rev. **D64**, 093010 (2001).

[21] W. Pauli, Phys. Today **31N9**, 27 (1978).

[22] C. L. Cowan, F. Reines, F. B. Harrison, H. W. Kruse, and A. D. McGuire, Science **124**, 103 (1956).

[23] G. Danby *et al.*, Phys. Rev. Lett. **9**, 36 (1962).

[24] M. L. Perl *et al.*, Phys. Rev. Lett. **35**, 1489 (1975).

[25] K. Kodama *et al.*, Phys. Lett. **B504**, 218 (2001).

[26] C. Quigg, Front. Phys. **56**, 1 (1983).

[27] Y. Fukuda *et al.*, Phys. Rev. Lett. **81**, 1562 (1998).

[28] B. Pontecorvo, Sov. Phys. JETP **6**, 429 (1957).

[29] Z. Maki, M. Nakagawa, and S. Sakata, Prog. Theor. Phys. **28**, 870 (1962).

[30] J. N. Bahcall, P. I. Krastev, and A. Y. Smirnov, Phys. Rev. **D58**, 096016 (1998).

[31] S. P. Rosen, Los Alamos Sci. **25**, 156 (1997).

[32] R. Davis, Front. Phys. **5**, 47 (1993).

[33] G. L. Fogli, E. Lisi, A. Palazzo, and F. L. Villante, Phys. Rev. **D63**, 113016 (2001).

[34] Q. R. Ahmad *et al.*, Phys. Rev. Lett. **87**, 071301 (2001).

[35] R. Becker-Szendy *et al.*, Phys. Rev. **D46**, 3720 (1992).

[36] K. S. Hirata *et al.*, Phys. Lett. **B280**, 146 (1992).

[37] M. C. Sanchez *et al.*, Phys. Rev. **D68**, 113004 (2003).

[38] Y. Fukuda *et al.*, Phys. Lett. **B433**, 9 (1998).

[39] M. H. Ahn *et al.*, Phys. Rev. **D74**, 072003 (2006).

[40] D. G. Michael *et al.*, Phys. Rev. Lett. **97**, 191801 (2006).

[41] J. G. Learned and K. Mannheim, Ann. Rev. Nucl. Part. Sci. **50**, 679 (2000).

[42] K. Hirata *et al.*, Phys. Rev. Lett. **58**, 1490 (1987).

[43] K. S. Hirata *et al.*, Phys. Rev. **D38**, 448 (1988).

[44] R. M. Bionta *et al.*, Phys. Rev. Lett. **58**, 1494 (1987).

[45] C. B. Bratton *et al.*, Phys. Rev. **D37**, 3361 (1988).

[46] E. N. Alekseev, L. N. Alekseeva, I. V. Krivosheina, and V. I. Volchenko, Phys. Lett. **B205**, 209 (1988).

[47] M. Herant, S. A. Colgate, W. Benz, and C. Fryer, Los Alamos Sci. **25**, 164 (1997).

[48] P. Antonioli *et al.*, New J. Phys. **6**, 114 (2004).

[49] P. Bhattacharjee and G. Sigl, Phys. Rept. **327**, 109 (2000).

[50] E. Waxman, New J. Phys. **6**, 140 (2004).

[51] F. Halzen, Presented at 17th International Workshop on Weak Interactions and Neutrinos (WIN99), Cape Town, South Africa, 24-30 Jan 1999, arXiv:astro-ph/9904216.

[52] M. Punch *et al.*, Nature **358**, 477 (1992).

[53] T. K. Gaisser, F. Halzen, and T. Stanev, Phys. Rept. **258**, 173 (1995).

[54] C. E. Fichtel *et al.*, Astrophys. J. **434**, 557 (1994).

[55] J. Hinton, (2008), arXiv:0803.1609.

[56] J. Quinn *et al.*, Astrophys. J. **456**, L83 (1996).

[57] D. Horan *et al.*, Astrophys. J. **571**, 753 (2002).

[58] P. M. Chadwick *et al.*, Astrophys. J. **513**, 161 (1999).

[59] T. Yamamoto *et al.*, Prepared for 26th International Cosmic Ray Conference (ICRC 99), Salt Lake City, Utah, 17-25 Aug 1999.

[60] F. Aharonian *et al.*, Astron. Astrophys. **403**, L1 (2003).

[61] G. Superina, W. Benbow, T. Boutelier, G. Dubus, and B. Giebels, Prepared for 30th International Cosmic Ray Conference (ICRC 2007), Merida, Yucatan, Mexico, 3-11 Jul 2007, to appear in arXiv:0710.4057.

[62] F. Aharonian *et al.*, Astron. Astrophys. **436**, L17 (2005).

[63] F. Aharonian *et al.*, Nature **440**, 1018 (2006).

[64] F. Aharonian *et al.*, Astron. Astrophys. **475**, L9 (2007).

[65] F. Aharonian *et al.*, Astron. Astrophys. **475**, L25 (2007).

[66] F. Aharonian *et al.*, Astron. Astrophys. **448**, L19 (2006).

[67] J. Albert *et al.*, Astrophys. J. **648**, 105 (2006).

[68] M. Teshima *et al.*, (2007), arXiv:0709.1475.

[69] F. W. Stecker and M. H. Salamon, Space Sci. Rev. **75**, 341 (1996).

[70] K. Mannheim, Astropart. Phys. **3**, 295 (1995).

[71] R. Gandhi, C. Quigg, M. H. Reno, and I. Sarcevic, Astropart. Phys. **5**, 81 (1996).

[72] R. Gandhi, C. Quigg, M. H. Reno, and I. Sarcevic, Phys. Rev. **D58**, 093009 (1998).

[73] F. W. Stecker, Phys. Rev. **D72**, 107301 (2005).

[74] M. McConnell *et al.*, Adv. Sp. Res. **19:1**, 25 (1997).

[75] J. Abraham *et al.*, Science **318**, 938 (2007).

[76] V. Schonfelder, Prepared for Symposium on the Interface of Astrophysics with Nuclear and Particle Physics, Zuoz, Switzerland, 11-18 Apr 1992.

[77] S. E. Woosley, Astrophys. J. **405**, 273 (1993).

[78] D. Eichler, M. Livio, T. Piran, and D. N. Schramm, Nature **340**, 126 (1989).

[79] T. Piran, Phys. Rept. **314**, 575 (1999).

[80] A. A. Watson, Nucl. Phys. Proc. Suppl. **22B**, 116 (1991).

[81] D. J. Bird *et al.*, Phys. Rev. Lett. **71**, 3401 (1993).

[82] F. Halzen, R. A. Vazquez, T. Stanev, and H. P. Vankov, Astropart. Phys. **3**, 151 (1995).

[83] A. Mucke, R. Engel, J. P. Rachen, R. J. Protheroe, and T. Stanev, Comput. Phys. Commun. **124**, 290 (2000).

[84] J. Jones, I. Mocioiu, M. H. Reno, and I. Sarcevic, Phys. Rev. **D69**, 033004 (2004).

[85] L. A. Anchordoqui, H. Goldberg, D. Hooper, S. Sarkar, and A. M. Taylor, Phys. Rev. **D76**, 123008 (2007).

[86] F. Halzen and A. O'Murchadha, (2008), arXiv:0802.0887.

[87] R. P. Feynman, Phys. Rev. Lett. **23**, 1415 (1969).

[88] J. Pumplin *et al.*, JHEP **07**, 012 (2002).

[89] A. M. Dziewonski and D. L. Anderson, Phys. Earth Planet. Interiors **25**, 297 (1981).

[90] J. Ahrens *et al.*, Nucl. Instrum. Meth. **A522**, 347 (2004).

[91] M. Ackermann *et al.*, Nucl. Instrum. Meth. **A556**, 169 (2006).

[92] F. Halzen and D. Hooper, JCAP **0401**, 002 (2004).

[93] J. A. Aguilar *et al.*, Phys. Atom. Nucl. **67**, 1172 (2004).

[94] S. E. Tzamarias, Nucl. Instrum. Meth. **A502**, 150 (2003).

[95] E. Migneco *et al.*, Nucl. Phys. Proc. Suppl. **136**, 61 (2004).

[96] U. F. Katz, Nucl. Instrum. Meth. **A567**, 457 (2006), astro-ph/0606068.

[97] P. W. Gorham *et al.*, Phys. Rev. Lett. **99**, 171101 (2007).

[98] P. Miocinovic *et al.*, Proceedings of 22nd Texas Symposium on Relativistic Astrophyscis at Stanford University, Stanford, California, 13-17 Dec 2004, pp 2516, arXiv:astro-ph/0503304.

[99] S. W. Barwick, J. Phys. Conf. Ser. **60**, 276 (2007).

[100] P. Gorodetzky, Nucl. Phys. Proc. Suppl. **151**, 401 (2006).

[101] A. Ringwald, Nucl. Phys. Proc. Suppl. **136**, 111 (2004).

[102] M. Dine, W. Fischler, and M. Srednicki, Nucl. Phys. **B189**, 575 (1981).

[103] S. Dimopoulos and S. Raby, Nucl. Phys. **B192**, 353 (1981).

[104] L. Alvarez-Gaume, M. Claudson, and M. B. Wise, Nucl. Phys. **B207**, 96 (1982).

[105] M. Dine and A. E. Nelson, Phys. Rev. **D48**, 1277 (1993).

[106] M. Dine, A. E. Nelson, and Y. Shirman, Phys. Rev. **D51**, 1362 (1995).

[107] M. Dine, A. E. Nelson, Y. Nir, and Y. Shirman, Phys. Rev. **D53**, 2658 (1996).

[108] G. F. Giudice and R. Rattazzi, Phys. Rept. **322**, 419 (1999).

[109] W.-M. Yao *et al.*, J. Phys. G: Nucl. Part. Phys. **33**, 1 (2006).

[110] S. P. Martin, (1997), arXiv:hep-ph/9709356.

[111] C. F. Kolda, Nucl. Phys. Proc. Suppl. **62**, 266 (1998).

[112] A. Heister *et al.*, Eur. Phys. J. **C25**, 339 (2002).

[113] J. Abdallah *et al.*, Eur. Phys. J. **C27**, 153 (2003).

[114] P. Achard *et al.*, Phys. Lett. **B517**, 75 (2001).

[115] G. Abbiendi *et al.*, Phys. Lett. **B572**, 8 (2003).

[116] T. Gherghetta, G. F. Giudice, and A. Riotto, Phys. Lett. **B446**, 28 (1999).

[117] Particle Data Group, S. Eidelman *et al.*, Phys. Lett. **B592**, 1 (2004).

[118] R. Devenish and A. Cooper-Sarkar, Oxford, UK: Univ. Pr. (2004) 403 p.

[119] H. Abramowicz and A. Levy, (1997), arXiv:hep-ph/9712415.

[120] B. Badelek, J. Kwiecinski, and A. Stasto, Z. Phys. **C74**, 297 (1997).

[121] R. P. Kokoulin and A. A. Petrukhin, Proc. of the XII International Conference on Cosmic Rays (Hobart, Tasmania, Australia, 1971), Vol. 6.

[122] O. Nachtmann, Berlin, Germany: Springer (1990) 559 p.

[123] A. A. Petrukhin and V. V. Shestakov, Can. J. Phys. **46**, S377 (1968).

[124] H. Baer and X. Tata, Cambridge, UK: Univ. Pr. (2006) 537 p.

[125] M. H. Reno, Nucl. Phys. Proc. Suppl. **143**, 407 (2005).

[126] S. I. Dutta, M. H. Reno, I. Sarcevic, and D. Seckel, Phys. Rev. **D63**, 094020 (2001).

[127] P. Antonioli, C. Ghetti, E. V. Korolkova, V. A. Kudryavtsev, and G. Sartorelli, Astropart. Phys. **7**, 357 (1997).

[128] D. Fargion, P. G. De Sanctis Lucentini, and M. De Santis, Astrophys. J. **613**, 1285 (2004).

[129] D. Fargion, Astrophys. J. **570**, 909 (2002).

[130] S. I. Dutta, Y. Huang, and M. H. Reno, Phys. Rev. **D72**, 013005 (2005).

[131] R. P. Kokoulin and A. A. Petrukhin, Sov. J. Part. Nucl. **21**, 332 (1990).

[132] E. V. Bugaev and Y. V. Shlepin, Phys. Rev. **D67**, 034027 (2003).

[133] E. Bugaev, T. Montaruli, Y. Shlepin, and I. Sokalski, Astropart. Phys. **21**, 491 (2004).